ISSN: 1857 - 839X
DOI: 10.55302/SJCE

Volume 13
Issue 2
December 2024

SJCE
SCIENTIFIC JOURNAL OF CIVIL ENGINEERING

SS CYRIL AND METHODIUS UNIVERSITY
FACULTY OF CIVIL ENGINEERING

EDITORIAL - Preface to Volume 13 Issue 2 of the Scientific Journal of Civil Engineering (SJCE)

Vladimir Vitanov EDITOR - IN - CHIEF

Dear Readers,

The Scientific Journal of Civil Engineering (SJCE) is an internationally peer-reviewed, open-access journal that commenced publication in December 2012 and operates on a biannual release schedule. Since December 2021, the journal has transitioned to a fully digital platform encompassing submission, review, and publication processes. For more details on the digital journal edition, visit www.sjce.gf.ukim.edu.mk.

SJCE upholds a commitment to the dissemination of high-quality, innovative scientific research across the expansive domain of engineering sciences. The journal's primary objective is to advance technical knowledge and foster groundbreaking engineering solutions in areas including civil engineering, geotechnics, surveying and geospatial engineering, environmental protection, construction management, and related disciplines. By adhering to an open-access model, SJCE ensures transparent and comprehensive availability of original research papers, offering a platform for contributions that address both theoretical and practical dimensions of civil engineering and its associated fields.

As Editor-in-Chief, it is my privilege to introduce the second issue of Volume 13, which encompasses eight meticulously peer-reviewed research articles. This edition represents an open-subject collection and features contributions that have successfully fulfilled the rigorous review standards established by the journal. These articles encompass a diverse array of advanced scientific topics.

The first article systematically compares conventional steel moment-resisting frames and self-centering steel frames through seismic analyses, focusing on the latter's ability to minimize damage and residual displacements while maintaining equivalent peak story displacements. The second article investigates the use of machine learning tools, specifically the SOLDIER application and HEC ResSim software, to optimize and manage complex water systems within the Crna Reka basin in North Macedonia. The third article examines the use of sensors and automated algorithms to assess building sensitivity to traffic-induced vibrations, with potential integration into real-time smart monitoring systems. The fourth article discusses the use of PSInSAR, a satellite-based technique, to measure displacements in the Skopje region using Sentinel-1 images. The fifth article describes the application of the Least Squares Modification of the Stokes integral with Additive corrections (LSMSA) to geoid determination in western North Macedonia, noting its precision despite limited terrestrial gravity data. The sixth article examines the resistance and ductility of headed stud connectors in steel-concrete composite beams through experimental testing and elastic-plastic analysis using 3D/FM models. The seventh article presents findings that repointing masonry structures using advanced materials enhances their compressive strength, seismic resistance, and long-term stability while remaining cost-effective. The eighth article outlines a methodology for assessing the seismic vulnerability of existing masonry structures in the city of Gostivar to evaluate the risk posed by earthquakes.

Finally, I extend my thanks to all our contributors, reviewers, and readers for their involvement in this issue.

Sincerely,

Vladimir Vitanov, Editor-in-Chief

December 2024

SJCE
SCIENTIFIC JOURNAL OF CIVIL ENGINEERING

Impressum

FOUNDER AND PUBLISHER

Faculty of Civil Engineering
Partizanski odredi 24, 1000 Skopje, N. Macedonia

PRINT

This Journal is printed in Mar-saz DOOEL Skopje

EDITORIAL OFFICE

Faculty of Civil Engineering
Partizanski odredi 24, 1000 Skopje, N. Macedonia
tel. +389 2 3116 066
fax. +389 2 3118 834
prodekan.nauka@gf.ukim.edu.mk

EDITOR IN CHIEF

Prof. PhD **Vladimir Vitanov**

Ss. Cyril and Methodius University in Skopje
Faculty of Civil Engineering
Partizanski odredi 24, 1000 Skopje, N. Macedonia
v.vitanov@gf.ukim.edu.mk

EDITORIAL ADVISORY BOARD

Valentina Zhileska Panchovska, PhD

Professor, Ss. Cyril and Methodius University in Skopje, Faculty of Civil Engineering, Skopje, N. Macedonia

Denis Popovski, PhD

Professor, Ss. Cyril and Methodius University in Skopje, Faculty of Civil Engineering, Skopje, N. Macedonia

Igor Peshevski, PhD

Professor, Ss. Cyril and Methodius University in Skopje, Faculty of Civil Engineering, Skopje, N. Macedonia

ISSN: 1857-839X
DOI: https://www.doi.org/10.55302/SJCE

TECHNICAL EDITORS

MSc Natasha Malijanska Andreevska

Assistant, Ss. Cyril and Methodius University in Skopje, Faculty of Civil Engineering, Skopje, N. Macedonia

MSc **Ivona Nedevska Trajkova**

Assistant, Ss. Cyril and Methodius University in Skopje, Faculty of Civil Engineering, Skopje, N. Macedonia

MSc Frosina Panovska Georgievska

Assistant, Ss. Cyril and Methodius University in Skopje, Faculty of Civil Engineering, Skopje, N. Macedonia

EDITORIAL BOARD

Marijana Lazarevska, PhD

Ss. Cyril and Methodius University in Skopje, Faculty of Civil Engineering, Skopje, N. Macedonia

Elena Dumova Jovanoska, PhD
Ss. Cyril and Methodius University in Skopje, Faculty of Civil Engineering, Skopje, N. Macedonia

Zlatko Bogdanovski, PhD

Ss. Cyril and Methodius University in Skopje, Faculty of Civil Engineering, Skopje, N. Macedonia

Ljupco Dimitrievski, PhD

Ss. Cyril and Methodius University in Skopje, Faculty of Civil Engineering, Skopje, N. Macedonia

Zlatko Zafirovski, PhD
Ss. Cyril and Methodius University in Skopje, Faculty of Civil Engineering, Skopje, N. Macedonia

Katerina Donevska, PhD

Ss. Cyril and Methodius University in Skopje, Faculty of Civil Engineering, Skopje, N. Macedonia

Tina Dasic, PhD

University of Belgrade, Faculty of Civil Engineering, Belgrade, R. Serbia

Vlastimir Radonjanin, PhD

University of Novi Sad, Faculty of Technical Sciences, Novi Sad, R. Serbia

Nenad Ivanisevic, PhD

University of Belgrade, Faculty of Civil Engineering, Belgrade, R. Serbia

Milos Knezevic, PhD
University of Montenegro, Faculty of Civil Engineering, Podgorica, Montenegro

Marina Rakocevic, PhD
University of Montenegro, Faculty of Civil Engineering, Podgorica, Montenegro

Stjepan Lakusic, PhD
University of Zagreb, Faculty of Civil Engineering, Zagreb, Croatia

Andrej Kryzanowski, PhD
University of Ljubljana, Faculty of Civil and Geodetic Engineering, Ljubljana, Slovenia

Ales Znidaric, PhD
ZAG – Slovenian National Building and Civil Engineering Institute, Ljubljana, Slovenia

Heinz Brandl, PhD
Vienna University of Technology, Institute for Geotechnics, Vienna, Austria

Resat Ulusay, PhD
Hacettepe University, Faculty of Engineering, Ankara, Turkey

SJCE
SCIENTIFIC JOURNAL OF CIVIL ENGINEERING

Impressum

ORDERING INFO

SJCE is published bi-annually. All articles published in the journal have been reviewed.

Edition: 100 copies

SUBSCRIPTIONS

Price of a single copy:
for Macedonia (500 den);
for abroad (10 EUR + shipping cost).

BANKING DETAILS (NORTH MACEDONIA)

Narodna banka na RNM
Account number:
160010421978815,
Prihodno konto 723219,
Programa 41

BANKING ETAILS (INTERNATIONAL)

Correspond bank details:
Deutsche Bundesbank
Zentrale Address: Wilhelm Epstein Strasse 14 Frankfurt am Main, Germany SWIFT BIC: MARK DE FF
Bank details:
National Bank of the RNM
Address: Kompleks banki bb 1000 Skopje, North Macedonia
SWIFT BIC: NBRM MK 2X
IBAN: MK 07 1007 0100 0036 254
Name: Gradezen Fakultet, Skopje

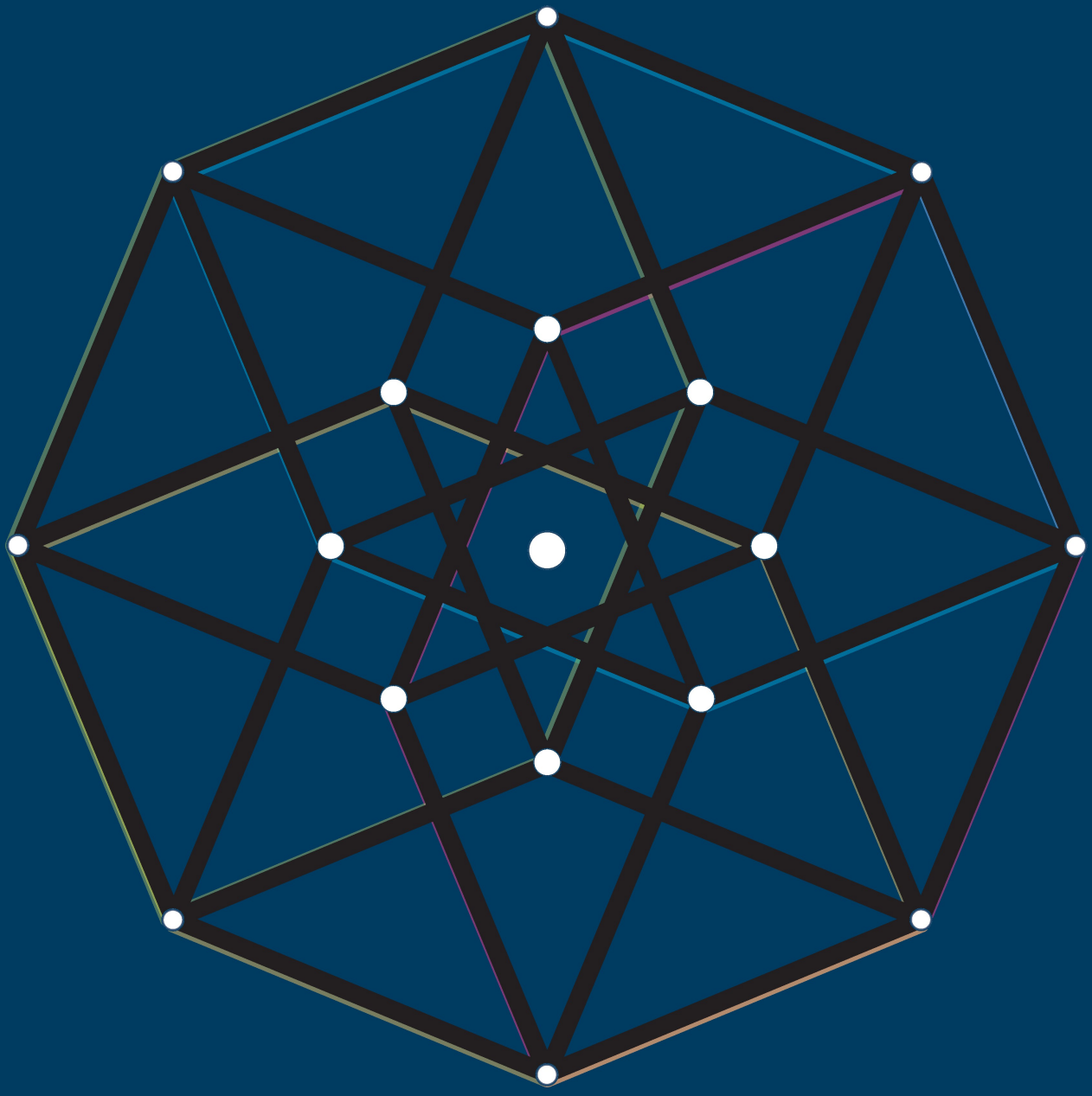

ГРАДЕЖНО КОНСТРУКТОРСТВО – БЕЗ ОГРАНИЧУВАЊА
STRUCTURAL ENGINEERING – LIMITLESS

ДГКМ
ДРУШТВО НА ГРАДЕЖНИ КОНСТРУКТОРИ НА МАКЕДОНИЈА

MASE
MACEDONIAN ASSOCIATION OF STRUCTURAL ENGINEERS

21 МЕЃУНАРОДЕН СИМПОЗИУМ
INTERNATIONAL SYMPOSIUM

ОХРИД, С. МАКЕДОНИЈА
OHRID, N. MACEDONIA
24 - 27 септември 2025
September 24th - 27th 2025

обликување мбиком + дд

SJCE
SCIENTIFIC JOURNAL OF CIVIL ENGINEERING

CONTENTS

6-ти Конгрес за брани

6th Congress on Dams

16-18.10.2025

www.macold.org.mk

ЗМКГБ MACOLD

Здружение Македонски комитет за големи брани
Macedonian Committee on Large Dams

член на
member of

Меѓународна комисија за големи брани
International Commission on Large Dams

CIGB ICOLD

Angela Poposka
MSc in Civil Engineering
Ss. Cyril and Methodius University in Skopje
Institute of Earthquake Engineering and Engineering Seismology
N. Macedonia
angela@iziis.ukim.edu.mk

Zoran Rakicevic
PhD, Professor
Ss. Cyril and Methodius University in Skopje
Institute of Earthquake Engineering and Engineering Seismology
N. Macedonia

Theodoros Karavasilis
PhD, Professor
University of Patras
Department of Civil Engineering
Greece

COMPARISON OF CONVENTIONAL AND SELF-CENTERING STEEL FRAME WITH BRACINGS

DOI: https://www.doi.org/10.55302/SJCE2421307p

This paper focuses on seismic design, assessment and comparison of conventional steel moment-resisting frame with bracings and self-centering steel frame with bracings. A prototype building was selected and designed as a conventional frame according to Eurocode 8 and as a self-centering frame. The self-centering frame is designed to utilize the same cross-section as the conventional one, while the post-tensioning connection is developed based on an iterative pushover analysis, conducted at the early phase of the design process to estimate rotations and axial forces in post-tensioned (PT) connections and to provide comparable shear strength to the conventional frame. To compare the performance of the both systems, a nonlinear dynamic analysis is conducted using a set of 30 ground motions, scaled to represent the frequently occurring earthquake (FOE), design-based earthquake (DBE), and maximum considered earthquake (MCE). Seismic analyses results show that the conventional and the self-centering frame have comparable peak story displacements and highlight the potential of the second one to eliminate or reduce damage and residual displacements.

Keywords: Conventional steel systems, self-centering systems, residual displacement.

1. INTRODUCTION

Conventional seismic-resistant systems such as steel moment resisting frames (MRFs) or concentrically braced frames (CBFs) are currently designed to develop significant inelastic deformations in the main structural members (i.e., beams and columns and/or braces) under strong earthquakes [1]. This design approach offers certain advantages, such as achieving acceptable seismic performance in terms of life safety and cost-effectiveness. Designing a structure to remain elastic during a strong earthquake would require oversized structural components, making elastic systems not justified both economically and due to increased acceleration. However, allowing inelastic deformations in main structural elements can lead to challenges in repairing damage,

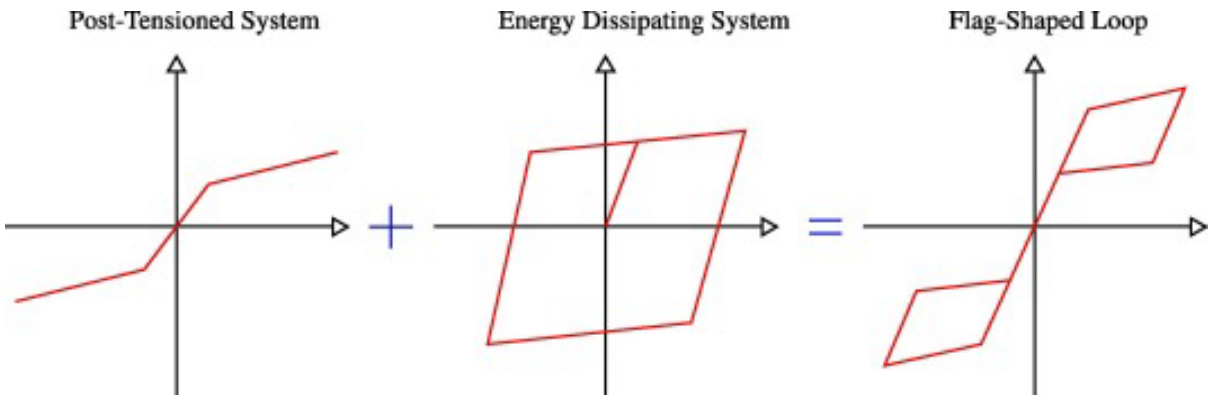

Figure 1. Formation of a flag-shaped hysteresis loop [10]

residual drifts, and consequently, higher repair costs and extended downtime while the building is out of service. A study conducted in Japan by McCormick et al. [2] which examined 12 steel-framed buildings affected by the 1995 Hyogoken-Nanbu earthquake, concluded that in cases where residual inter-story drifts exceeded 0.5% it was more cost-effective to demolish and rebuild the structures rather than repair them due to the high repair costs and the financial losses associated with keeping the building closed during repairs. These losses emphasize the importance of implementing more resilient structures that are less vulnerable and easier to repair after strong earthquakes, with the aim of minimizing or even preventing economic seismic losses. Steel self-centering frames with post-tensioned (PT) beam-column connections are a type of resilient seismic-resistant structure that prevent inelastic deformations in beams and reduce or eliminate residual drifts. These systems usually use energy dissipation devices which are activated when gaps open and can be easily replaced if damaged.

In this paper, a comparison between the conventional steel frame and self-centering steel frame where the dissipation of the energy is designed to be through the braces under tension is presented. For this purpose, a prototype steel building is designed with two different lateral load-resisting systems, i.e. conventional MRF with bracings and corresponding self-centering steel frame. To achieve a fair comparison, both seismic resistant frames are designed using the same structural member dimensions which results in two systems having very similar initial stiffness and periods of vibration.

2. SELF-CENTERING SYSTEMS

In seismic design, while life safety remains a priority, modern expectations, particularly in developed countries, demand buildings to maintain almost full functionality after an earthquake. It's been discussed that residual deformations are commonly seen as an unwanted effect of seismic loads, prompting researchers to develop methods to predict and reduce them. However, a more ambitious goal is to eliminate these residual deformations and return the structure to its original position after the end of a seismic action. This idea has led to the development of systems that return the structure to its original position, or the so-called self-centering systems. These systems are characterized with post-tensioned steel strands that remain elastic throughout seismic loading, providing an elastic restoring force and energy dissipation mechanism. Energy dissipation occurs through specialized dissipaters or elements designed to undergo inelastic behavior during rocking, while the beams and columns remain elastic. The combination of these two hysteretic behaviors creates the "flag-shaped" hysteresis loop, offering both energy dissipation and self-centering during cyclic loading, Figure 1.

Furthermore, if we compare the nonlinear response of the conventional yielding system and self-centering system, Figure 2 there are few main differences, 1) the flag-shaped hysteresis inherently has less energy dissipation per cycle, half at most; 2) the flag-shaped hysteresis has more frequent stiffness changes within one nonlinear cycle than the elastoplastic hysteresis and 3) The flag-shaped hysteresis returns to the zero-force, zero-displacement point at every cycle whereas yielding of the elastoplastic system at every cycle may lead to cumulative "crawling" of the response in one direction.

3. PROTOTYPE BUILDING AND DESIGN OF SEISMIC-RESISTANT FRAMES

The case study is a four-story building with a square plan of four bay by four bay, and a total length of 24.00 m x 24.00 m. The story height is equal to 3.0 m except for the first floor, which is 4.00 m high. The lateral force resisting system is placed at the perimeter of the plan of the buildings, consisting of two seismic frames in longitudinal direction and 2 in transverse direction. The interior frames are assumed to be gravity frames, and their lateral load resisting capacity is neglected. Consequently, the tributary area for seismic masses defers from the tributary area for the gravity loads in a way that the first one takes into account half the mass whereas the second takes into consideration the half bay mass, as described on figure 3. The perimeter frame is designed as a steel MRF with braces and as a self-centering frame with braces.

3.1 DESIGN OF A CONVENTIONAL FRAME

The design of the structure is done according to the provisions of EN 1993 and EN 1998-1 and it is carried out using commercial software. The model represents the distribution of stiffness and mass so that all significant deformation shapes and inertia forces are properly accounted for under seismic action. The models used to perform the designs are based on the centerline dimensions of the steel MRFs without accounting for the finite panel zone dimensions. The columns are considered continuous through each floor beam whereas the braces are pinned. All beam-column connections have been considered fully strength and fully rigid while all floors are assumed made of composite slabs with profiled steel sheeting that should be designed to resist the vertical loads and to behave as horizontal rigid diaphragms able to transmit the seismic actions to the seismic resistant frames. Masses were considered lumped in a selected master joint for each floor, because the floor diaphragms may be taken as rigid in their planes. The building satisfies the criteria for regularity both in plan and in elevation.

For the spectrum analysis, it is required to consider a number of vibration modes that satisfy either of the conditions of EC8. In this case, the first two mode shapes are considered (Tx1=0.6 sec and Tx2=0.17 sec). The SRSS (Square Root of the Sum of the Squares) method is used to combine the modal maxima,

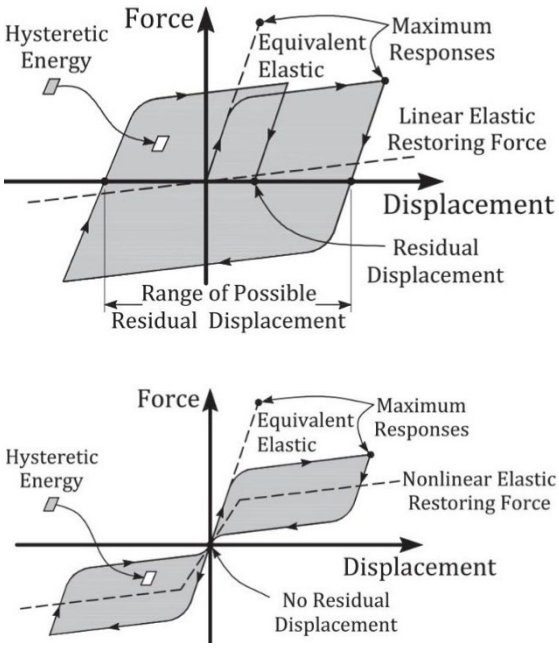

Figure 2. Idealized seismic response of yielding system (up) and self-centering system (down) [4]

since the first and the second modes of vibration in X direction are independent (T2 ≤ 0.9T1).

The steel MRF is designed as medium-ductility class according to EC8 [1]. The material for all frame elements is S275 steel with an over-strength factor γ_{ov} = 1.25. The chosen member sections are standard metric sections which are commercially available. The gravity loads are taken as approximative values for administrative/residential building, 5.50 kN/m^2 and 3.0 kN/m^2, for the dead and live load, respectively.

The DBE (10% probability of exceedance in 50 years) is expressed by the type 1 EC8 design spectrum for peak ground acceleration equal to 0.3g, ground type B, importance factor II, and behavior factor q equal to 4 (for moment resisting frames combined with concentric bracings). To meet the damage limitation requirement given ductile non-structural elements, the allowable peak story drift, θmax, under the frequently occurred earthquake (10% probability of exceedance in 10 years) is equal to 0.75% according to Eurocode [1]. The frequently occurred earthquake has an intensity of 40% the DBE, i.e. the v reduction factor is equal to 0.4 according to EC8 [1]. For all the steel MRFs, the story drift sensitivity coefficient θ that accounts for P-Δ effects is limited below 0.20. The maximum considered earthquake is assumed to have an intensity equal to 150% the DBE intensity.

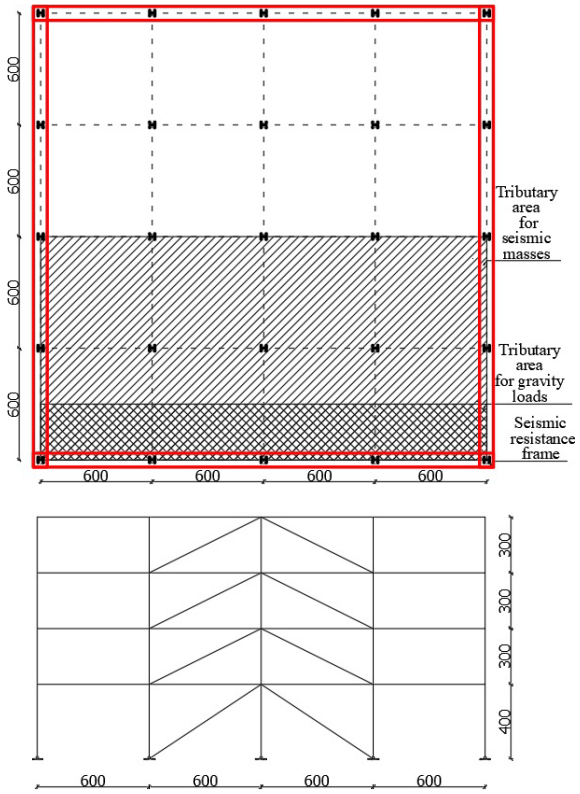

Figure 3. Plan and cross-section of the seismic resistance frame

Both flexural and shear checks are done for the verification of the beams belonging to external and internal bays according to the following equations (Eq.1 - Eq.3).

$$\frac{M_{Ed}}{M_{pl,Rd}} \leq 1 \quad (1)$$

$$\frac{V_{Ed}}{V_{pl,Rd}} \leq 0.50 \quad (2)$$

$$\frac{N_{Ed}}{N_{pl,Rd}} \leq 0.15 \quad (3)$$

The columns are also checked against axial forces, bending moments and shear forces calculated according to [1] and Eq.4 - Eq.6:

$$M_{Ed} = M_{Ed,G} + 1.1 * \gamma_{ov} * \Omega * M_{Ed,E} \quad (4)$$

$$V_{Ed} = V_{Ed,G} + 1.1 * \gamma_{ov} * \Omega * V_{Ed,E} \quad (5)$$

$$N_{Ed} = N_{Ed,G} + 1.1 * \gamma_{ov} * \Omega * N_{Ed,E} \quad (6)$$

where NEd,G, MEd,G, and VEd,G are the design values of the axial force, bending moment, and shear force due to non-seismic actions; γ_{ov} is the material overstrength factor that is equal to 1.25; and Ω is an overstrength factor which is calculated as the minimum of the ratios of the plastic moment resistance to the internal bending moment under the seismic action of all beams. Design details of the conventional frame are provided in Table 1. The braces are designed according to the rules described in Eurocodes.

Table 1. Cross-section of the steel frame elements

Story	Structural elements			P_{T0}
	Columns	Beams	Braces	[kN]
1	HE200B HE220B	IPE 300	160.160. 12.5	580
2	HE200B HE220B	IPE 300	140.140. 10	580
3	HE200B	IPE 300	140.140. 8	580
4	HE200B	IPE 270	120.120. 6	540

The weak beam-strong column capacity design rule is enforced by satisfying the following condition:

$$\frac{\sum M_{Rc}}{\sum M_{Rb}} \geq 1.3 \quad (7)$$

3.2 DESIGN OF A SELF-CENTERING FRAME

As mentioned before, the PT connection of the self-centring frame is designed using the same cross-sections for the structural elements as the conventional frame. In such a way, frame with the same or very close initial stiffness and period of vibration as the conventional one is obtained, but with different type of lateral-load resisting system and consequently with different structural performance under strong ground motions.

The main accent in the design of a self-centering frames is in the design of the post-tensioning connection between the column and the beam which is designed to "open" for a certain moment known as moment of decompresion. To achive this, the PT force in the cables that are supposed to replace the moment connection at the initial condition shoud be properly designed. According to the equations and recommendations of Garlock [5], the ratio of the decompression moment and the plastic moment of the beam should have value less than one and higher than 0.5 so that the self-centering will be posible, Eq.8.

An iterative procedure (trial and error) was made to obtain ratio of these moments and a ratio of 0.55 was defined. For this purpose, a pushover analysis was conducted at the early phase of the design process and the pushover curves of the two frames were compared, so that the self-centering frame has base share

strength comparable to that of the conventional frame. It should be mention that when calculating the decompression moment, the contribution of the two prestressed cables is taken into account.

$$0.5 \leq \frac{M_d}{M_{pl,b}} < 1 \quad (8)$$

$$M_d = P_{T0} * \frac{b_h}{2} = 0.55 * M_{pl,b} \quad (9)$$

After decompression, the gap opening results in an increase in the post-tensioning force, PT, which can be calculated from the equations derive by Christopoulos [4].

$$P_T = P_{T0} + 2K_{PT}(1 - 1/\Omega)b_h\theta \quad (10)$$

$$\Omega = 1 + \frac{K_b}{K_c + 2K_{PT}} \quad (11)$$

Where: $K_b, K_c \; and \; K_{PT}$ are the axial stiffness's of the beam, column and PT elements, respectively (AE/L).

The diameter of the cable is calculated according to the Eq.10-12, where $f_{y,PT}$ is 1770 MPa. The required cross-section of the diameter can be assumed so that the value of the initial prestressing force is half the value of the yield force of the cables ($P_{T0}/P_{Ty} \approx 0.5$) which approximately ensures that PT bars avoid yielding under large rotations in the PT connections [7]. Also, the area of the cables should be verified for the designed drift demand for the frame.

$$P_{Ty} = 0.5 * f_{y,PT} * \pi * d_{PT}^2 \quad (12)$$

4. NONLINEAR MODELS OF THE FRAME

To investigate the seismic performance, two-dimensional nonlinear analytical models of the conventional and of the self-centering frame were developed for nonlinear dynamic analyses in OpenSees [11]. The conventional frame is modelled according to the guidelines for conventional frames [11] whereas for the modeling of the self-centering frame experimental results were used [3] [10]. The SC model uses *force-based non-linear beam-column elements* to represent the braces, columns and beams. An initial camber was applied at the mid-point of the brace to simulate the effects of buckling, whereas the beam and the columns remain in elastic range. The PT connection is modeled using truss elements with applied initial PT force utilizing the *"initStrain"* material. For simulating the rocking connection ENT *("elastic no-tension"*) material is used.

5. NONLINEAR DYNAMIC ANALYSIS AND COMPARISON OF THE RESULTS

5.1 GROUND MOTIONS AND PROCEDURE FOR DYNAMIC ANALYSES

A set of 30 recorded ground motions, developed by the INNOSEIS project [9] was used for nonlinear dynamic time-history

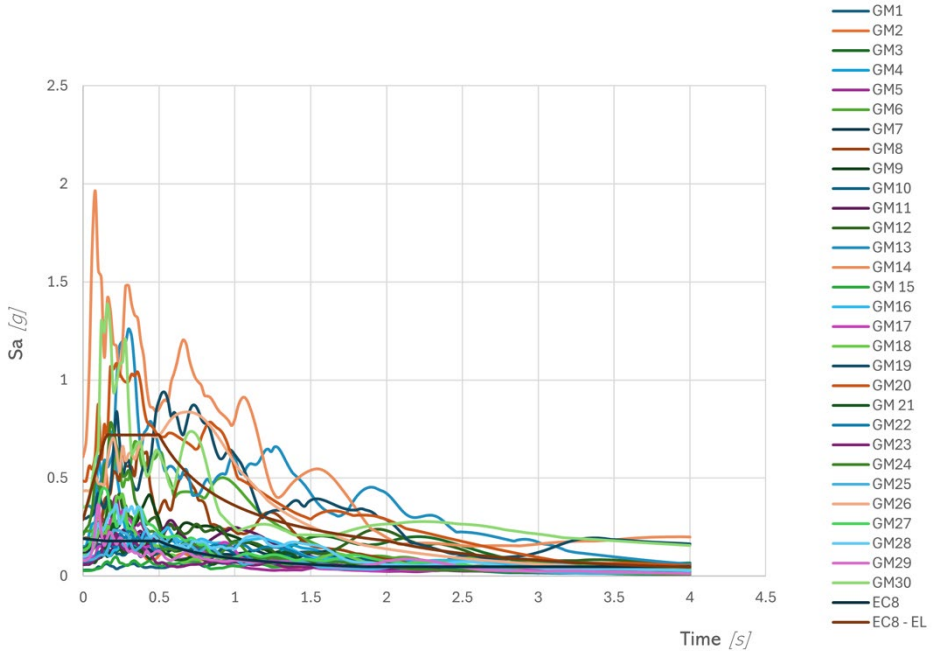

Figure 4. Acceleration response spectra of the ground motions considered in this study (unscaled)

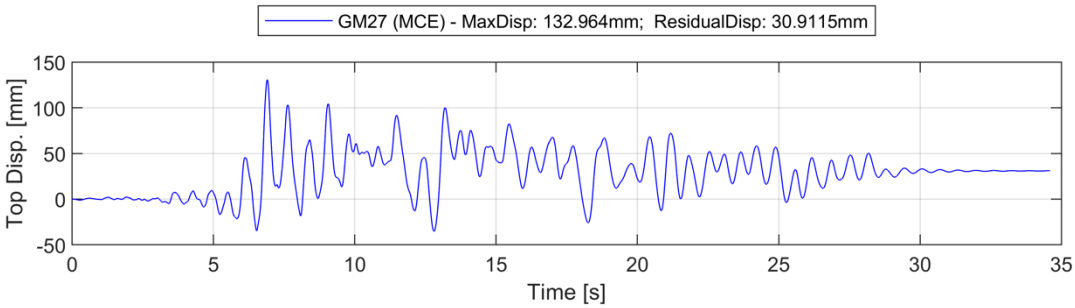

Figure 5. Time history plot of top displacement for MCE for conventional frame

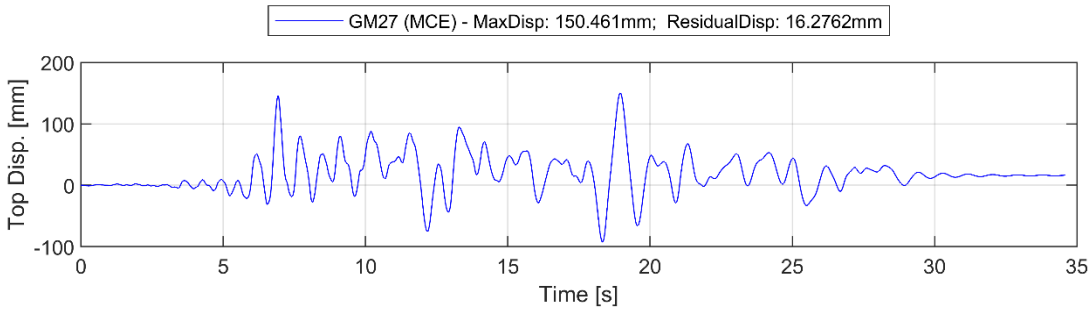

Figure 6. Time history plot of top displacement for MCE for self-cantering frame

analyses. The ground motions were scaled to FOE, DBE (Figure 4) and MCE, where the seismic intensity was represented by the 5% spectral acceleration, Sa, at T (0.6sec) of the frame models.

The Newmark method with constant acceleration is used to integrate the equations of motion. The Newton method with tangent stiffness is used to minimize the unbalanced forces within each integration time step. A Rayleigh damping matrix is used to model the inherent 3.3% critical damping at the first two modes of vibration. Each dynamic analysis was extended beyond the actual earthquake time to allow for damped free vibration decay and accurate residual drifts calculation.

5.2 SESMIC ASSESSMENT

The results of the 90 nonlinear response-history analyses for the two design cases were post-processed and the results are presented as the mean, median and standard deviation values for the maximum displacement and residual displacement, in table 2 and table 3, for the conventional and for the self-centering frame, respectively. A comparison is shown for one earthquake excitation – ground motion 27 (Figure 5 and 6), which reflects the statistical trend, which is that the self-centering system plays a role generally only during the maximum expected earthquake (MCE) and in that case it eliminates or reduces the residual deformations more than 50%.

Table 2. Mean, median and STD for the maximum and residual displacement for conventional frame

		Mean	Median	STD
FOE	Max. disp. [mm]	33.8	33.4	2.6
	Res. disp. [mm]	0.4	0.4	0.2
DBE	Max. disp. [mm]	85.6	83.3	17.0
	Res. disp. [mm]	11.1	11.6	7.0
MCE	Max. disp. [mm]	163.5	137.7	99.7
	Res. disp. [mm]	34.4	22.0	35.9

Table 3. Mean, median and STD for the maximum and residual displacement for conventional frame

		Mean	Median	STD
FOE	Max. disp. [mm]	33.1	32.6	2.4
	Res. disp. [mm]	1.1	1.1	0.9
DBE	Max. disp. [mm]	114.1	104.1	45.1
	Res. disp. [mm]	12.0	9.6	9.2
MCE	Max. disp. [mm]	204.8	180.5	123.7
	Res. disp. [mm]	12.7	9.1	16.5

6. SUMMARY AND CONCLUSIONS

In this paper, a comparison between a conventional moment resisting frame with braces and self-centering frame with braces is presented. For that purpose, the design procedure according to Eurocode 3 and 8 is given for the conventional frame. The design of the self-centering frame is carried out so that the same cross-section of the conventional frame is used, and a design for the posttensioning connection is done according to the recent research and guidelines for PT connections. In such a way, frame with the same or very close initial stiffness and period of vibration as the conventional one is obtained, but with different type of lateral-load resisting. Thus, the frames will have different structural performance under strong ground motions. To compare the different behavior, nonlinear dynamic analysis is performed for a set of 30 ground motions, scaled for FOE, DBE and MCE.

The results show that self-centering mechanism plays a significant role only for the case of maximum considered earthquake and it generally eliminates or reduce the residual displacement for at least 50% and consequently decrease the probability for non-repairability. The reason why this applies only for MCE is the conservative design of EC8, particularly the FOE design drift limits. Thus, for low to moderate earthquakes the frames behave almost elastic, and the energy dissipation and self-centering mechanisms do not make a difference.

Also, the maximum displacements for the SC frame are slightly higher. The results confirmed findings of previous studies regarding peak and residual displacements (Karavasilis and Seo 2011) indicating that for structures with a period exceeding 0.5 seconds, energy dissipation does not play a significant role [6]. Furthermore, the conventional frame experience damage in the beams for DBE and MCE, whereas the self-centering frame is damage free in the beam because of the rocking mechanism, but experience damage in the braces.

Based on aforementioned outcomes and previous work showing that self-centering and conventional systems of the same strength and period of vibration have similar seismic drifts when the self-centering system is designed with increased energy dissipation capacity and post yield stiffness [6], it can be concluded that the self-centering frame with braces may have better performance if equipped with energy dissipation devices acting as fuses for the braces.

REFERENCES

[1] Eurocode 8: Design of structures for earthquake resistance – part 1: General rules, seismic actions and rules for buildings. European Standard EN 1998-1:2004.

[2] McCormick et al., (2008), Permissible residual deformation levels for building structures considering both safety and human elements. In Proceedings of the 14th World Conference on Earthquake Engineering, Beijing, China

[3] Goggins et al., (2021), Shake Table Testing of Self-Centring Concentrically Braced Frames, https://doi.org/10.1002/cepa.1508

[4] Christopoulos, C. (2002). Self-Centering Post-Tensioned Energy Dissipating (PTED) Steel Frames for Seismic Regions. PhD Thesis. University of California, San Diego, California, USA.

[5] Garlock at al., (2004), Design and behavior of post-tensioned steel moment frames

[6] Karavasilis et al., (2011), Seismic structural and non-structural performance evaluation of highly damped self-centering and conventional systems, Engineering Structures, [VOL33, ISSUE8, DOI: 10.1016/j.engstruct.2011.04.001

[7] Rojas et al., (2004) Seismic performance of post-tensioned steel moment resisting frames with friction devices. Journal of Structural Engineering 2004; 131(4): 529-540

[8] Seo C.-Y et al., (2005) Ductility Demands on Self-centering Systems under Earthquake Loading. ACI Structural Journal 2005; 102(2):275-285

[9] INNOSEIS, (2017), Valorization of INNOvative anti-SEISmic Devices. http://innoseis.ntua.gr

[10] O'Reilly et al., (2024) Validation of a Numerical Model for Novel Self-Centring Concentrically Braced Steel Frames, Infrastructures 2024, 9(7), 112

[11] McKenna et al. (2000). Open system for earthquake engineering simulation (OpenSees).

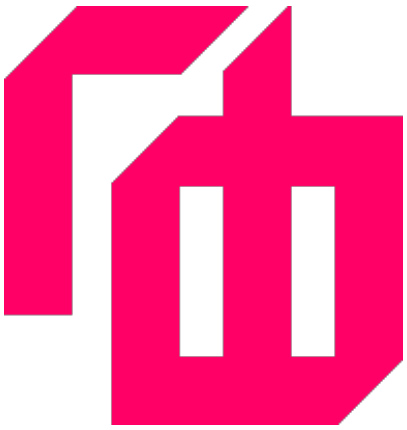

СЕКОГАШ БИДИ ИН

MANAGEMENT OF WATER RESOURCES SYSTEMS WITH USE OF SIMULATION MODELS AND MODELS BASED ON MACHINE LEARNING

Frosina Panovska Georgievska
Teaching assistant
MSc in Civil Engineering
Ss. Cyril and Methodius University in Skopje
Faculty of Civil Engineering
N. Macedonia
fpanovska@gf.ukim.edu.mk

Stevcho Mitovski
PhD, Associate professor
Ss. Cyril and Methodius University in Skopje
Faculty of Civil Engineering
N. Macedonia

Ljupcho Petkovski
PhD, Professor
Ss. Cyril and Methodius University in Skopje
Faculty of Civil Engineering
N. Macedonia

DOI: https://www.doi.org/10.55302/SJCE2421315pg

Throughout the history of humankind, in parallel with the progress of civilizations, the techniques and methods for analyzing structures in construction have undoubtedly progressed. As a tool of the latest date that finds application in undoubtedly every sector of construction, is the use of tools from machine learning - a branch of artificial intelligence. The tool offers opportunities for use in construction for optimization of structures, safety analysis, cost analysis and construction cost optimization, as well as help in their real time daily management. Undoubtedly, these machine-learning tools can be applied to dam and reservoir engineering as well as water management. As complex systems with deterministic output and stochastic input, machine-learning tools can help in all phases – from planning, construction, and operation to management of water systems. In this paper, the application of machine learning tools with analyses in the SOLDIER application in decision-making in the management of a complex water management system is described. A case study has been prepared for a part of the Crna Reka basin in RN Macedonia. In addition to the SOLDIER application, the HEC ResSim software was used to generate input and output data in the management of the systems – data used to train the model in SOLDIER.

Keywords: water management systems, reservoirs, hydropower, simulation model, machine learning, SOLDIER, HEC ResSim.

1. INTRODUCTION

Throughout the history of humankind, in parallel with the progress of civilizations, the techniques and methods for analysis of civil engineering structures have undoubtedly progressed. From the Stone Age, to the construction of the pyramids in Egypt, the construction of the Tower of Babylon, the sewers and water supply in Rome, the Great Wall of China, the Acropolis in Athens, to the construction of the Three

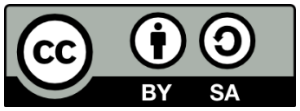

Gorges Dam in China with an incredible height of 181m and a crown length of 2335m , we have come at a moment in civil engineering history where structures reached incredible sizes, with new materials of carbon fiber, steel and concrete, maintaining their stability, defying the weather, gravity and natural stochastic incident occurrences (earthquake and flood).

From an engineering point of view, machine learning represents a process of forming a mathematical correlation between certain variables that are of interest in the analysis of the structures.

Undoubtedly, these machine-learning tools can be applied to dam engineering as well as water resources management. Water resources systems are complex systems with stochastic input and deterministic output and machine-learning tools can be applied in all stages – from planning, designing, construction and management of such systems.

In this paper, the application of machine learning tools with carried out analyses in the application SOLDIER in decision-making in the management of a complex water management system is described. A case study has been prepared for a part of the Crna Reka basin in RN Macedonia. In addition to the SOLDIER application, the HEC ResSim software was used to generate input and output data in the water management of the system – data used to train the model in SOLDIER.

SOLDIER application is developed by CIMNE – International center for numerical methods in engineering [2] based in Barcelona, Spain. The main goal of the CIMNE application is to analyze the relationship between different variables using machine learning. The main application of this software is focused in the field of technical monitoring of dams and appurtenant structures [3]. In the case study, it is applied to the analysis of operational rules for management of a complex hydropower multi storage system, by observing the correlation of the power production and the variables of the mathematical model, obtained with HEC ResSim.

HEC ResSim [4] software is open source, developed by the USACE Army Corps of Engineers. It is used for mathematical modeling of complex water management systems for determining operational management rules and for determining the physical parameters of the system.

2. CASE STUDY – CRNA REKA BASIN

As a case study, mathematical modeling was performed to determine operational parameters for the management of a complex hydropower system in the Crna Reka basin, specifically the gorge of the Crna Reka, where, according to the Water master plan from 1973, Chebren and Galishte reservoirs are planned for construction in addition to the existing Tikvesh reservoir.

Crna Reka is a right tributary of the Vardar River and it is one of the largest rivers in the Vardar River Basin with nearly ¼ of the total basin area, which is 5,890 km^2. The river flows through the Pelagonia and Tikvesh valleyes - both areas burdened with serious water management problems.

The course of the Crna Reka, from the spring to the confluence in the Vardar River passes through a mountainous, lowland and gorge part with a total length of 229 km. Along its course, Crna Reka receives several tributaries, the largest of which are: Shemnica river, on which hydro system Strezhevo is also built, Dragor river, Konjarka, Bela, Buturkica, Blešica, Raec and others. The average height above sea level of the Crna Reka basin is 863 masl. According to the Water Master plan of 1973, the course of Crna Reka can be divided into three parts:

- Spring, which is characterized by large falls and mountainous character of the basin;
- The middle course, which is characterized by small falls and is mostly flat - the part in which the Pelagonia valley is located;
- The gorge in the lower course of Crna Reka, which is characterized by large falls, distinctly mountainous terrain - very favorable for energy use of the water.

In the spring part of Crna Reka, as well as in the middle course, there are no favorable conditions for energy utilization of the water. Only the gorge in the lower course of the river provides solid opportunities for energy production. The gorge part of the course stretches from the town of Skochivir (108 km from the mouth of the Vardar River) to Tikvesh valley, near the village of Vozarci (26.3 km from the mouth of the Vardar River). In this part, with a total length of 81.7 km, the difference in terrain elevation is 400 m. On this stretch, the Tikvesh dam was built, with operational level of 265masl, with Tikvesh HPP, in which 4 Francis

hydro turbines were installed with a total installed power of 113MW and installed turbine flow of 144 m^3/s. After the construction of the Tikvesh dam, there are still about 300m of potential energy height and a length of 52.5km from Crna Reka, which have very favorable possibilities for hydropower utilization. According to the Water Master plan from 1973, the most favorable scheme for energy production is construction of two dams upstream of Tikvesh dam, both with hydropower plants - HPP Galište at 53,6km with operational level of 392masl and HPP Chebren at 81km with operational level of 565masl (Figure 1).

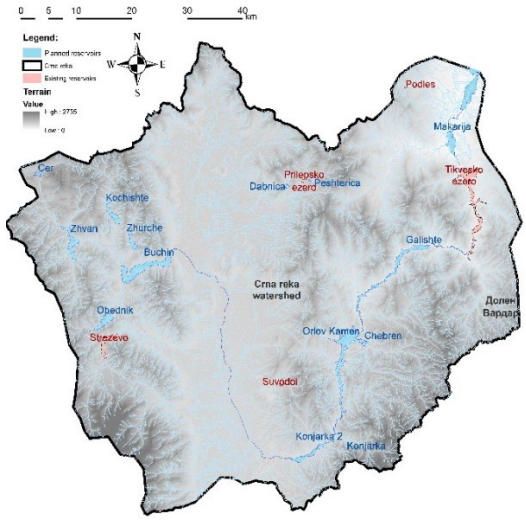

Figure 1. Planned and constructed reservoirs in the Crna Reka river basin, map created with Copernicus data [1]

The scheme for hydropower utilization of Crna reka in the gorge stretch consists of: 1) Chebren reservoir as the upstream reservoir and pumped-storage hydropower plant, 2) Orlov Kamen reservoir which will serve as a lower reservoir in pumping regime for HPP Chebren, 3) Galishte reservoir in the middle, and 3) Tikvesh reservoir as the downstream reservoir (Figure 2). HPP Galishte is planned as conventional hydropower plant.

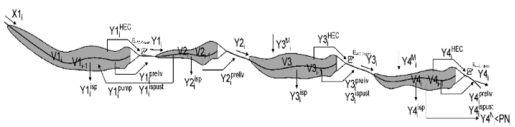

Figure 2. Schematic view of the analyzed scheme [2]

The dam profile for Chebren reservoir i the narrowest part of the Crna Reka course, with very favorable geotechnical and geological characteristics for the construction of a high dam. The dam site is located near the village of Manastir. The operational level in the reservoir is limited by the topography - up to 565masl - due to the danger of flooding of the Pelagonia valley. The volume of the formed reservoir up to the elevation of 565masl is $915\times10^6 m^3$, of which $555\times10^6 m^3$ are active volume. The reservoir is planned exclusively for the power production through HPP Chebren, and the size of the reservoir is sufficient for an annual leveling of the natural flows of Crna Reka. HPP Chebren will be located downstream of Chebren dam. If built with conventional units, the annual production of this plant with Francis hydro turbines is 352×10^6 kWh/year [3]. As a pumped-storage unit, the production is expected to be doubled – approximately 600×10^6 kWh/year [4].

Downstream of Chebren reservoir, Orlov Kamen reservoir is planned, as the lower basin for the pump regime of work of HPP Chebren. The operational level in this reservoir is 400masl.

The Galishte reservoir starts downstream from Orlov Kamen dam, all the way to the dam profile, which is located 56.3 km from the confluence of Crna Reka in the Vardar river. With the construction of the Galishte dam, a reservoir will form with operational level at 392 masl and a total capacity of 344×10^6 m^3 and active volume of 256×10^6 m^3. This hydropower plant is expected to deliver over of 224×10^6 kWh/year [5].

The next in line down the cascade of the river is the existing Tikvesh reservoir with HPP Tikvesh located downstream of Tikvesh dam. This plant delivers over 137×10^6 kWh/year [6]. The reservoir is also used for irrigation of Tikvesh valley - the primary water user in this scheme.

In the case study for which the water management planning was developed, the results of which are elaborated in this paper, the Chebren reservoirs with the Orlov Kamen and Galishte reservoirs were taken into account - as newly planned reservoirs, and the Tikvesh reservoir, as an existing reservoir.

3. APPLIED CODES

3.1. SOLDIER APP

The SOLDIER app is created by the CIMNE Institute in Barcelona, Spain, is a tool developed for machine learning application for dams and hydropower. The application works

by applying regression sequences, ie. creation of mathematical correlation between multiple variables based on previously known data [7].

The application has so far been used for the development of models for the analysis of the structural behavior of several dams in Europe, it is actively used within the framework of the DOLMEN project, which is focused on the application of methodologies for defining dynamic warning thresholds in the operation of dams with reservoirs for different purposes [8]. The application also won the Verbund prize in a competition for innovative challenges in 2017 [8].

3.2. HEC RESSIM SOFTWARE

HEC-ResSim is a software used to model complex water management systems in order to comply with the demands of one or more water users. With the help of the software, it is possible to model water resources systems by creating simulation models, that include multi-dimensional and multipurpose aspects (flood protection, meeting of water supply and irrigation demands, determining the capacity of reservoirs for hydropower production, as well as combinations of operational policies and prioritizing more water users according to the demands).

HEC-ResSim consists of: (1) user interface (GUI-Graphical User Interface), (2) a mathematical background program that simulates reservoir management, (3) files for saving data from the simulations, and (4) tools for processing the output results. HEC-ResSim uses a data storage system HEC-DSS (Data Storage System), through which data is provided for the system as time series (inflow in the reservoir, water level, water quantities for different needs, etc.) [9].

HEC-ResSim offers three modules through which the simulation model is defined:

- Module for defining the elements present in the simulation model and their interrelationship – setting up a watershed area Watershed Setup (defining rivers, tributaries, reservoirs, embankments, canals) ;
- Module for defining the physical parameters of the elements – Reservoir Network;
- Module for simulating the defined system – Simulation.

For the needs of the research work, with the help of HEC ResSim, a large number of input and output data were created, which are used as data that feeds the model in SOLDIER , which will create a dependency between the various variables - inflow into the reservoir, water level, water needs, discharge from reservoir, energy production, etc.

4. INPUT DATA FOR THE MACHINE LEARNING MODELS

The main goal of this research is the determination of correlation between the parameters that impact the water management of the abovementioned reservoirs. As main variables, they include:

- Hydrological series of inflows in reservoirs, defined as hydrographs of inflows for the period 2020 - 2050
- Outflow from reservoirs, defined as runoff hydrographs for the period 2020 – 2050
- Delivered irrigation water, defined as an irrigation hydrograph for the period from 2020 to 2050, for the Tikvesh reservoir
- Hydropower production for the period from 2020 to 2050,
- Operation in pumping mode at the Chebren reservoir for the period from 2020 to 2050,
- Variations of the water level in the reservoirs for the period from 2020 to 2050.

The specified hydrographs were obtained by simulation model created in HEC ResSim software, with a time step in the models of 1 day.

To create the simulation model, it is necessary to define: (1) inflow hydrograph in each reservoir, (2) physical characteristics of the reservoir, (3) water needs, and (4) operational rules for managing the system. In addition to the listed steps, the models also need to define the location of the reservoirs and their mathematical connection in order to perform rational and effective water management. Namely, the outflow from the upstream reservoir is inflow into the downstream reservoir. This connection is defined according to Figure 2, and it can be seen how it is set up with the HEC ResSim application in Figure 3.

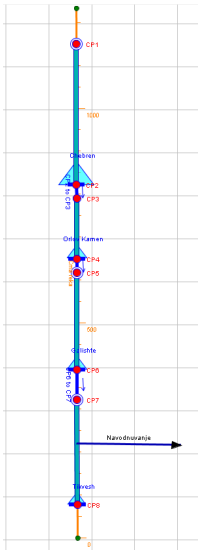

Figure 3. Schematic representation of the reservoirs in the study case apropos created model in HEC ResSim.

The hydrological input to the Chebren reservoir is taken from a historical series of measured mean monthly flows for the hydrological station Rasimbegov Most (Figure 4), for the Galishte reservoir - data from the hydrological station Galishte (Figure 6) and for the Tikvesh reservoir - data from the hydrological station Tikvesh (Figure 7). The time period of analysis is 30 years – from 2020 to 2050. The hydrological series of inflows correspond to the measured data from the period 1946 to 1976.

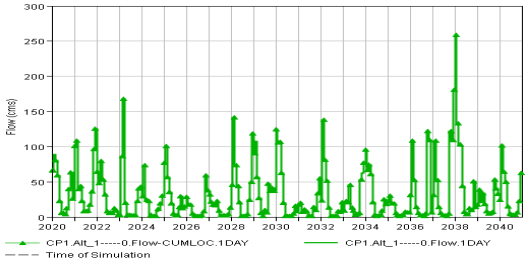

Figure 4. Inflow hydrograph for Chebren reservoir

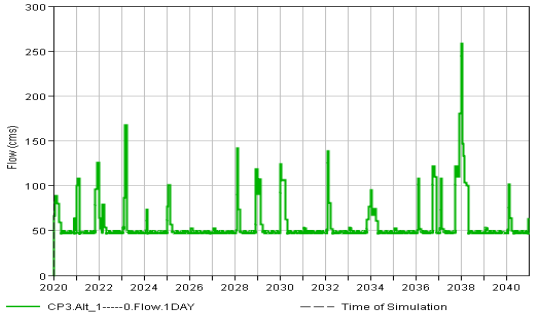

Figure 5. Inflow hydrograph for Orlov Kamen reservoir

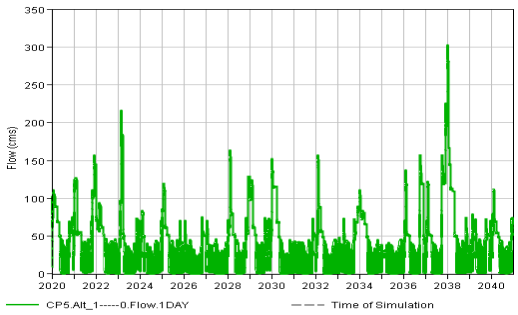

Figure 6. Inflow hydrograph for Galishte reservoir

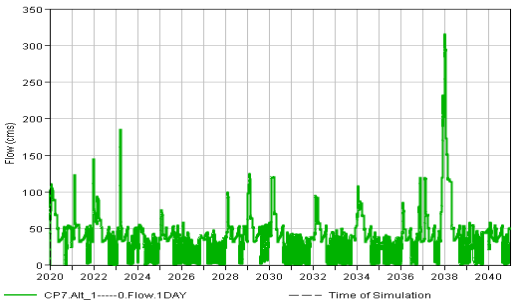

Figure 7. Inflow hydrograph for Tikvesh reservoir

As follows, the technical data for each reservoir is given in Tab. 1. It is a configuration consisting of a cascade system with four reservoirs on Crna Reka.

Table 1. Physical parameters of the reservoirs

Reservoir	Physical parameters		
Tikvesh	Normal operating level	265	masl
	Minimum operating level	233	masl
	Active volume	310 x 10^6	m^3
	Dam crest elevation	269	masl
	Installed power	115.32	MW
	Installed turbine flow	144	m^3/s
Galishte	Normal operating level	392	masl
	Minimum operating level	342	masl
	Active volume	256 x 10^6	m^3
	Dam crest elevation	398	masl
	Installed power	190.83	MW
	Installed turbine flow	180	m^3/s
Chebren	Normal operating level	565	masl
	Minimum operating level	515	masl
	Active volume	555 x 10^6	m^3
	Dam crest elevation	567.5	masl
	Installed power	458	MW
	Installed turbine flow	333	m^3/s
	Installed pump flow	150	m^3/s
Orlov Kamen	Normal operating level	400	masl
	Minimum operating level	393	masl
	Active volume	14.9 x 10 6	m^3
	Dam crest elevation	408	masl

The variation of water level in each reservoir is also used as a variable for making of correlation for management of the system, as well as the discharge from the reservoir. These data are shown for each reservoir in Figure 8, 9, 10 and Figure 11.

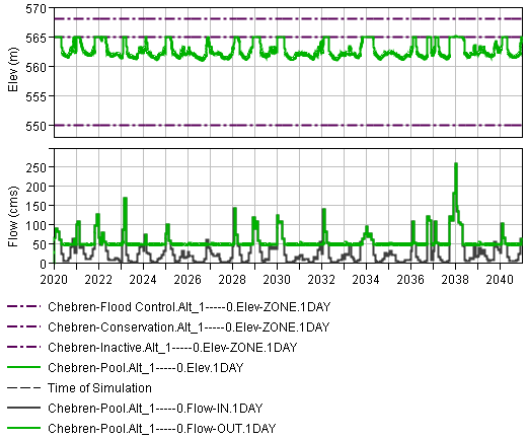

Figure 8. Variation of the water level in Chebren reservoir (upper graph), with a hydrograph of inflows and outflows (lower graph).

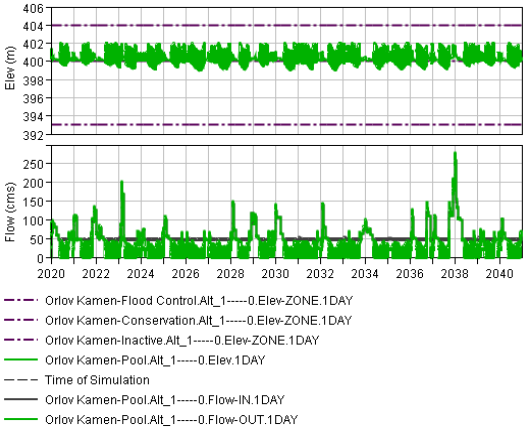

Figure 9. Variation of the water level in Orlov Kamen (top graph), with a hydrograph of inflows and outflows (bottom graph).

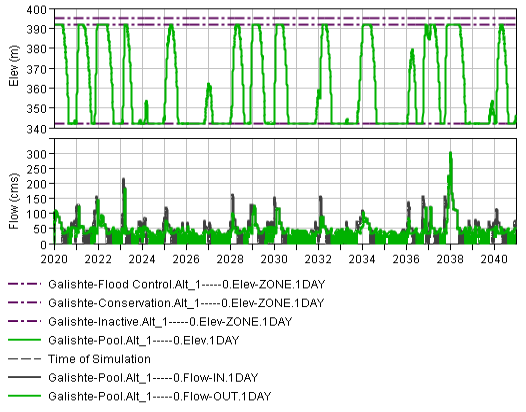

Figure 10. Variation of the water level in Galishte (top graph), with a hydrograph of inflows and outflows (bottom graph).

At the Tikvesh reservoir, in addition to power production, it is necessary to take in to account the quantities of delivered water for irrigation demands, for the analyzed period.

This is a seasonal variation of the flows, for a period of 30 years (Figure 12).

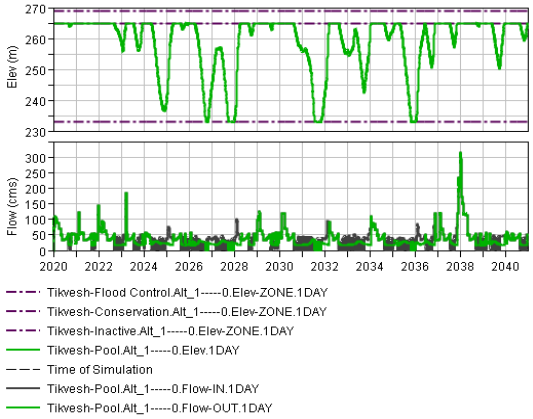

Figure 11. Variation of the water level in Tikvesh (top graph), with a hydrograph of inflows and outflows (bottom graph).

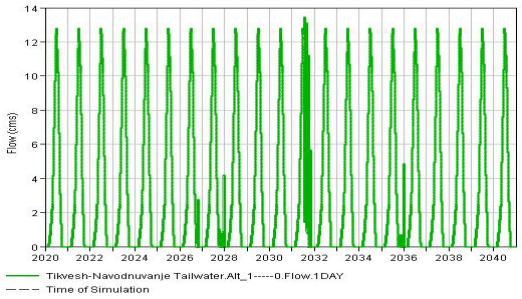

Figure 12. Hydrograph of supplied irrigation water from Tikvesh reservoir.

The primary purpose of each reservoir in the analysis is power production. Below are the output results of the power production in each hydropower plant, as a series of data for the analyzed period (Figure 13, 14 and 15).

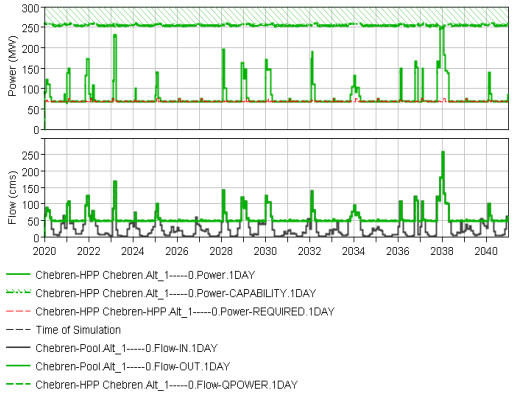

Figure 13. Time series of power production from HPP Chebren

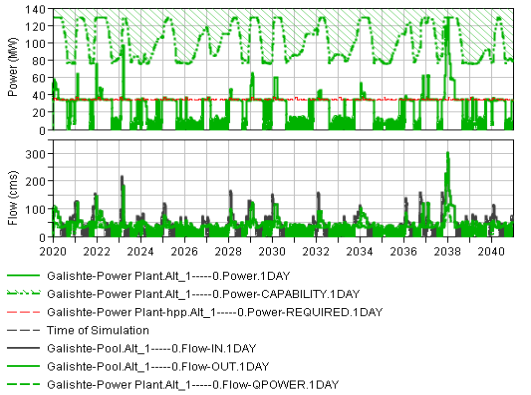

Figure 14. Time series of power production from HPP Galishte

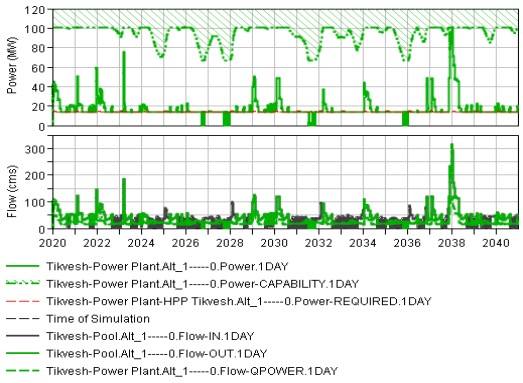

Figure 15. Time series of power production from HPP Tikvesh

5. OUTPUT RESULTS FROM THE MACHINE LEARNING MODELS

As follows, the output results from the models with machine learning are given. The model is fed with data obtained with the simulation models, for time series data for 30 years, in 1 day time step.

With the ML models, we will be able to observe the following correlations:

1. The hydropower production in correlation with the hydrological series of inflow into the reservoirs and the variations of the water level in the reservoir,

2. The overflow and downstream discharge for environmental flow in correlation with the hydropower production,

In the models, the principle of using 75% of the data for model training and 25% for testing the obtained results was applied.

To evaluate the suitability of the models, the mean absolute error (MAE) was calculated:

$$MAE = \frac{\sum_{i=1}^{N}|y_i - F(x_i)|}{N} \quad (1)$$

where N represents the number of data in the training zone or the validation zone, y_i are the observed outputs and $F(x_i)$ are the predicted values. This coefficient is measured in the same measurement units as the hypothesized variable, and it represents an intuitive measure of the model's accuracy [10].

In addition to the mean absolute error, the coefficient R^2 - coefficient of determination which is defined for a set of n - elements with $y_1 \ldots y_n$ results and their assumed values $y_1' \ldots y_n'$:

$$R^2(y, y') = 1 - \left(\frac{\sum_{i=1}^{N}(y_i - y_i')^2}{\sum_{i=1}^{N}(y_i - y')^2}\right), y' = \frac{1}{n}\sum_{i=1}^{N} y_i \quad (2)$$

The target value for the coefficient R^2 is 1, i.e. a score close to 1 indicates that the model made a solid mathematical correlation between the variables, and a score of 0 indicates that the model cannot establish any correlation between the variables [11].

5.1. CORRELATION BETWEEN POWER PRODUCTION, INFLOWS AND DISCHARGE FROM THE CHEBREN RESERVOIR

In order to understand the relationship between the hydropower production at Chebren HPP, a model has been prepared in the SOLDIER application in which the connection of the variables is analyzed: water level in the Chebren reservoir, inflows in the Chebren reservoir, hydropower production, overflow through the spillway, the released water through the bottom outlet and pump operation for return of water from the Orlov Kamen reservoir to the Chebren reservoir.

The target parameter in the analysis is hydropower production.

According to the output results, the MAE for the subject model is 9.68 for the learning period of the model, while it is 31.68 for the testing period. The coefficient R^2 is 1 for the model learning period, and 0.99 for the model testing period. The coefficients indicate a well-formed correlation between the variables and the target variable, and this can be seen in the graphic display of the adjustment of the target variable in Figure 16.

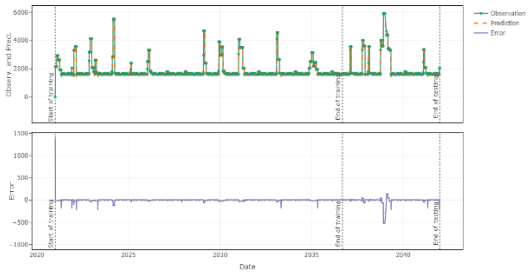

Figure 16. Adjustment of the variable – power production, in the learning zone of the model, and in the testing zone of the model at the Chebren reservoir.

The largest influence of the entered variables on the target variable is the HPP flow (Figure 17). The remaining variables have an insignificant influence on the formation of the mathematical relationship between the input variables and the target variable.

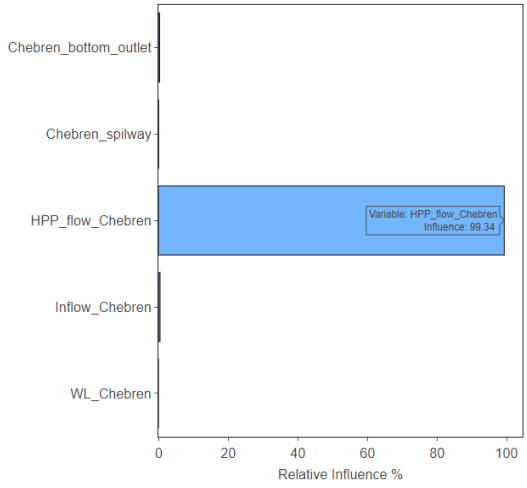

Figure 17. Relative influence of each variable in the target variable at Chebren reservoir

From Figures 18-21 it can be concluded that a higher inflow into the reservoir and a higher level of water in the reservoir generated higher hydropower production. Also, greater flow through the hydro plant and a higher level of water in the reservoir, generates increased hydropower production. These are logical and expected outcomes, by which it can be judged that the model provides realistic data and information regarding the correlation of the variables.

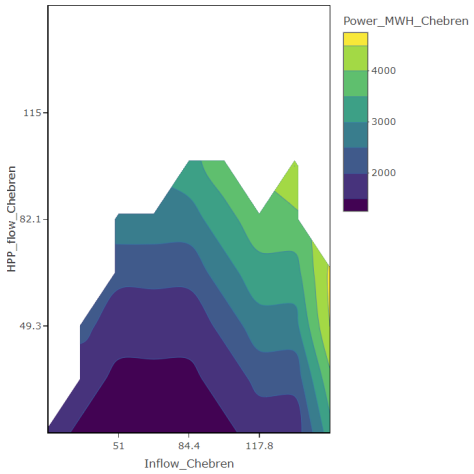

Figure 18. Partial dependence between the HPP flow, reservoir inflow and produced hydropower.

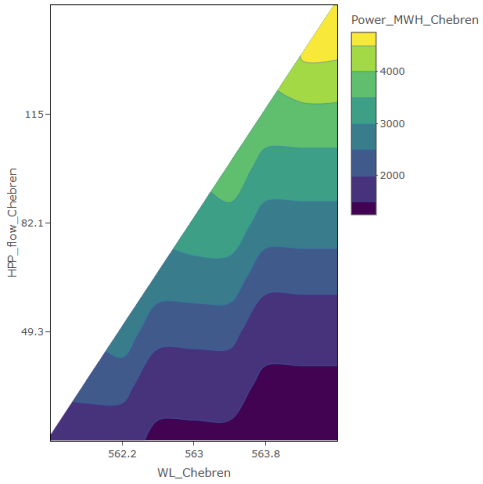

Figure 19. Partial dependence between the HPP flow, reservoir elevations and produced hydropower.

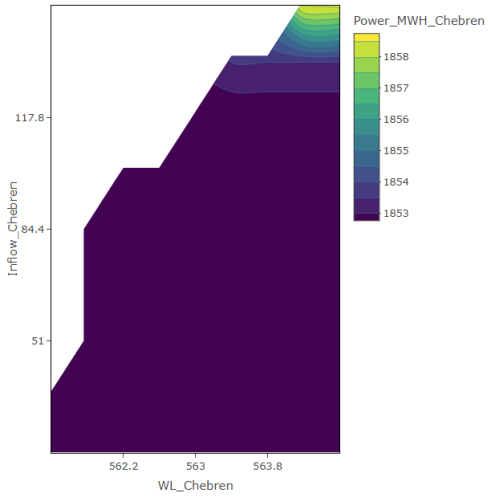

Figure 20. Partial dependence between inflows in the reservoir, reservoir level and hydropower production.

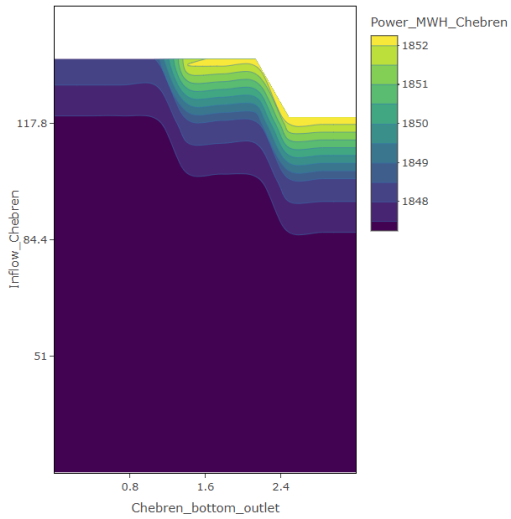

Figure 21. Partial dependence between inflow in the reservoir, bottom outlet flow produced hydropower.

5.2. CORRELATION BETWEEN PUMPED FLOW AND WATER LEVEL IN CHEBREN RESERVOIR

It is also of interest to see the correlation of the operation of HPP Chebren in pumping mode, ie. the operation of the pumps for filling the upper pool, for which a model has been prepared where the target variable is the operation of the pumps.

In this model, as variables that form the dependency for the target variable, the following are entered: water level in the Chebren reservoir and in Orlov Kamen, the produced hydropower, inflow into the Chebren reservoir and HPP flow.

According to the results, the MAE for the subject model is 0.19 for the learning period of the model, while it is 0.21 for the testing period. The coefficient R^2 is 1 for the model learning period, and 1 for the model testing period. The coefficients indicate a well-formed correlation between the variables and the target variable, and this can be seen in the graphic display of the adjustment of the target variable in Figure 22.

From the obtained results it can be concluded that the lower the water level in the Chebren reservoir, the more water is pumped into the upper pool, and the more the difference between the level in the upper and lower pool increases, the smaller the quantity of water that needs to be pumped (Figure 23 and 24). These are expected and logical results, which indicate a well-formed relationship between the variables in the model.

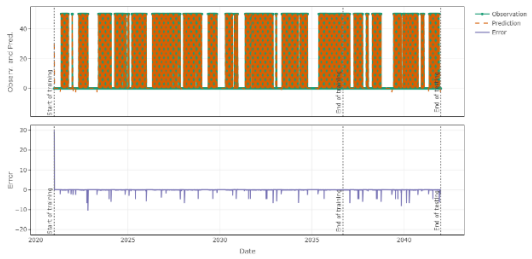

Figure 22. Adjusting the variable – the amount of water to be pumped into the upper basin in the learning zone of the model, and in the testing zone of the model.

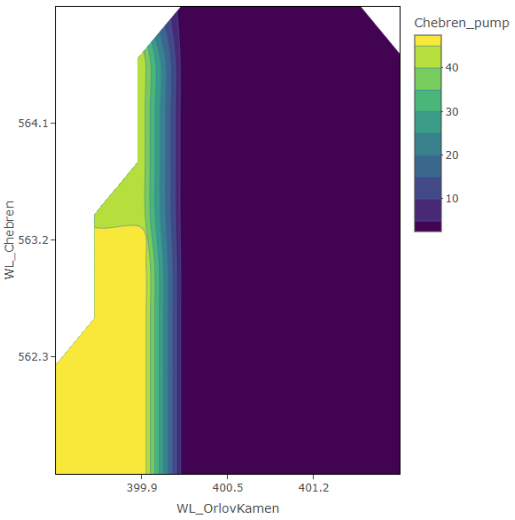

Figure 23. Partial dependence of the elevations in the Chebren and Orlov Kamen reservoirs on the amount of water pumped from the lower to the upper pool

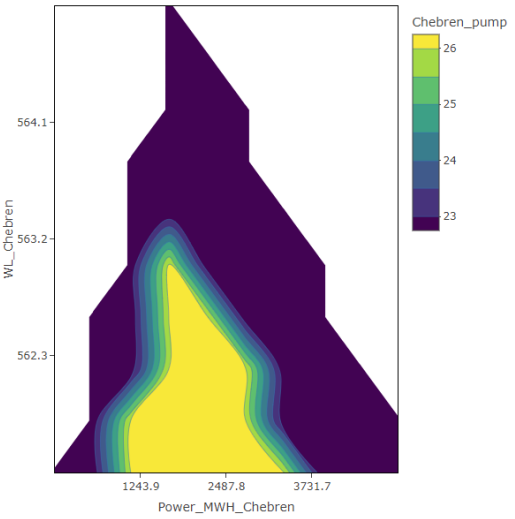

Figure 24. Partial dependence of the elevations in the Chebren reservoir with the produced hydropower and the required flow to be pumped into the upper pool.

5.3. CORRELATION BETWEEN HYDROPOWER PRODUCTION, INFLOW AND DISCHARGE FROM GALISHTE RESERVOIR

In order to understand the effect of hydropower production from HPP Galishte, a model has been prepared in the SOLDIER application in which the correlation of the variables is analyzed: water level in the Galishte reservoir, inflow in Galishte reservoir, hydropower production, spillway overflow and the flow through the bottom outlet.

The target variable in the analysis is hydropower production.

According to the results, the MAE for the subject model is 13.97 for the learning period of the model, while it is 19.94 for the testing period. The coefficient R^2 is 1 for the model learning period, and 0.99 for the model testing period . The coefficients indicate a well-formed correlation between the variables and the target variable, and this can be seen in the graphic display of the adjustment of the target variable in Figure 25.

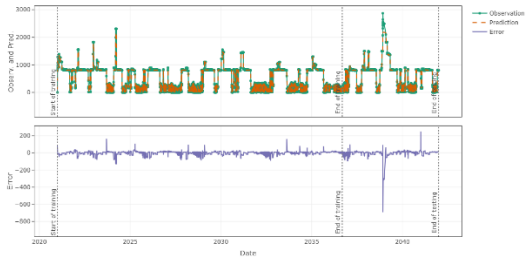

Figure 25. Adjustment of the variable – power production, in the learning zone of the model, and in the testing zone of the model at the Galishte reservoir.

Of the entered variables, the flow through HPP Galishte has the greatest relative influence on the target variable, with over 85% impact (Figure 26). Furthermore, it can be seen in Figure 26 that the spillway overflow also has a certain influence on the formation of the relationship between the variables and the target variable, as well as the water level in the Galishte reservoir. Inflow in the reservoir has an insignificant influence on the formation of the mathematical correlation.

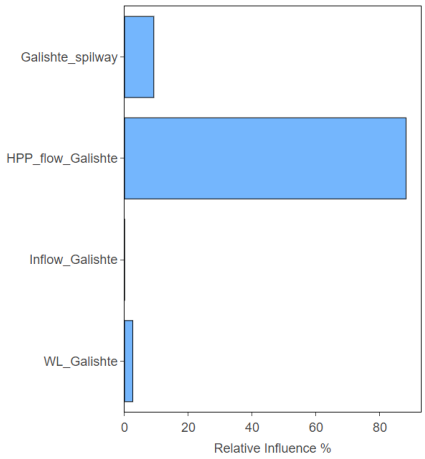

Figure 26. Relative influence of each variable in the target variable at Galishte reservoir.

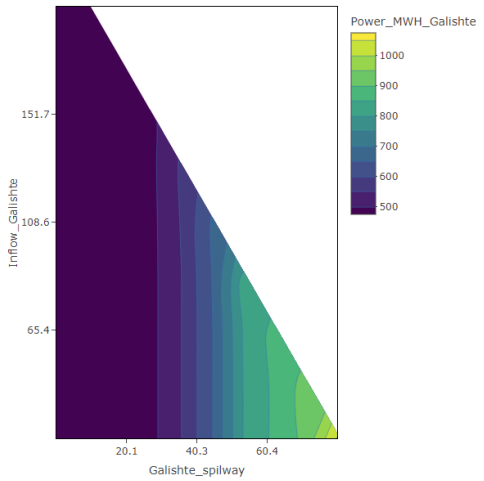

Figure 27. Partial dependence between inflow, spillway overflow and hydropower production at HPP Galishte.

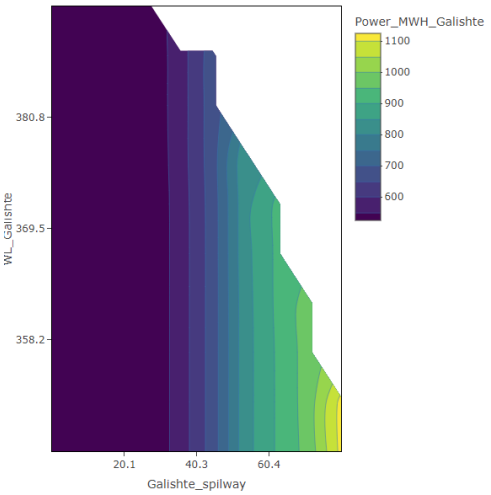

Figure 28. Partial dependence between the elevations in the Galishte reservoir, spillway overflow and hydropower production.

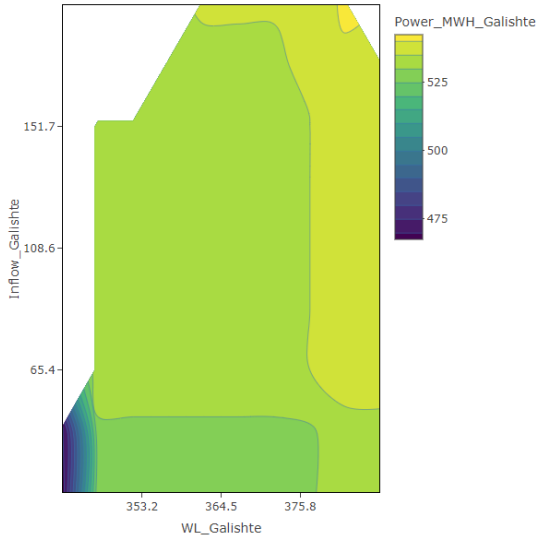

Figure 29. Partial dependence between the inflow, elevations in the reservoir and hydropower production at HPP Galishte.

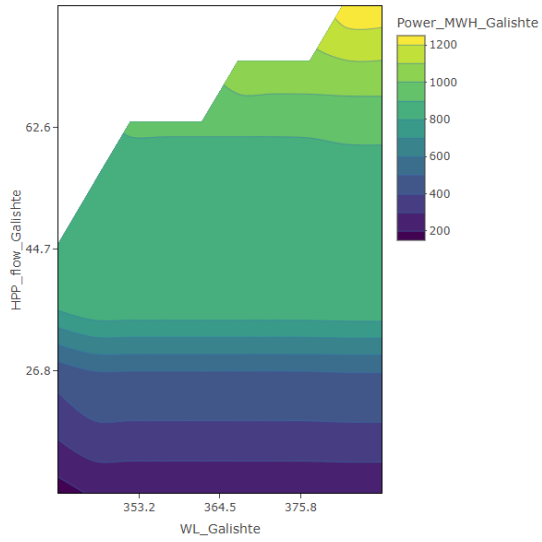

Figure 30. Partial dependence between the elevations in the Galishte reservoir, the HPP flow and hydropower production.

5.4. CORRELATION BETWEEN HYDROPOWER PRODUCTION, INFLOW AND DISCHARGE FROM TIKVESH RESERVOIR

In order to study the relationship between the hydropower production at HPP Tikvesh, a model has been prepared in the SOLDIER application in which the connection of the following variables is analyzed: water level in the Tikvesh reservoir, inflow in Tikvesh reservoir, hydropower production, spillway overflow, outflow in the bottom outlet and provided water for irrigation.

The target variable in the analysis is hydropower production.

According to the results, the MAE for the subject model is 7.36 for the learning period of the model, while it is 12.7 for the testing period. The coefficient R^2 is 1 for the model learning period, and 0.94 for the model testing period. The coefficients indicate a well-formed correlation between the inputs and the target variable, and this can be seen in the graphic display of the adjustment of the target variable in Fig. 31.

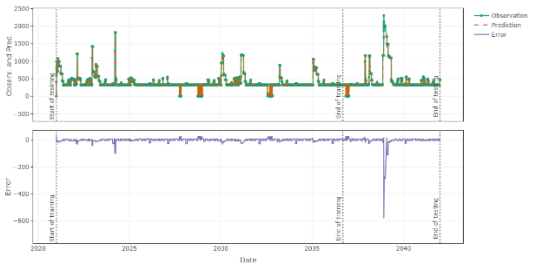

Figure 31. Adjustment of the variable – hydropower production at the HPP Tikvesh.

Of the entered variables, the spillway overflow has the greatest impact on the formation of the mathematical correlation, second is flow through the HPP and the reservoir inflow (Fig. 32).

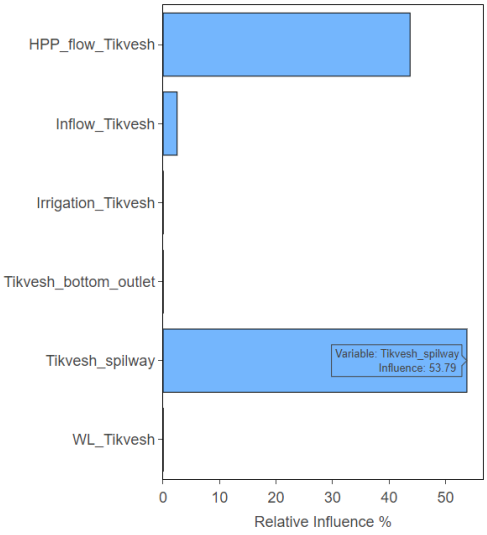

Figure 32. Relative influence of each variable in the target variable at Tikvesh reservoir.

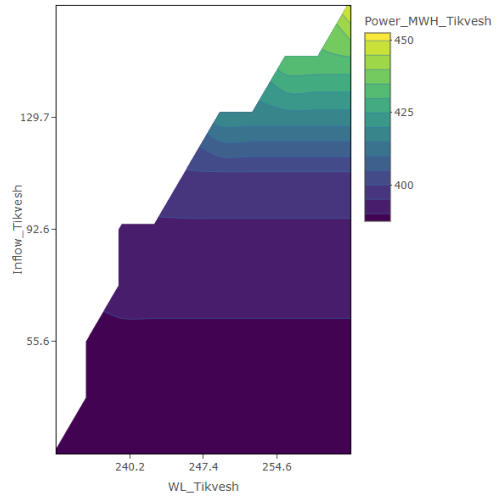

Figure 33. Partial dependence between the elevations in the Tikvesh reservoir, the reservoir inflow and hydropower production

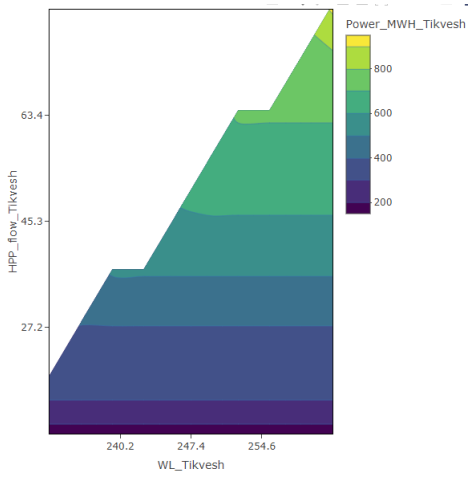

Figure 34. Partial dependence between the reservoir elevations, HPP flow and hydropower production at HPP Tikvesh.

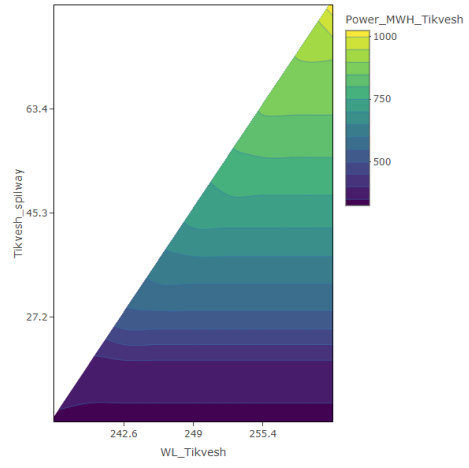

Figure 35. Partial dependence between the spillway overflow, reservoir elevations and hydropower production.

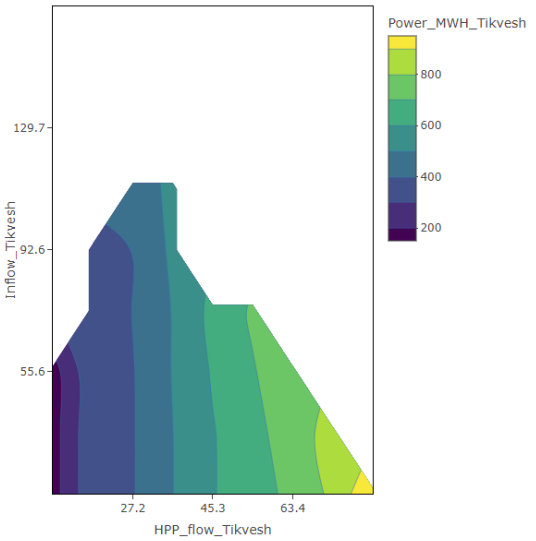

Figure 36. Partial dependence between reservoir inflow, HPP flow and hydropower production at HPP Tikvesh.

From the output results, it can be concluded that the higher the level in the reservoir, and the higher the inflow, the power production also increases. Also, the correlation between the flow through a hydropower plant and the elevations in the reservoir is similar – as they increase, the production of power also increases (Figure 33 and 34). In Figure 35 and 36 the correlation between the HPP flow and the inflow into the reservoir can be seen, in relation to the hydropower production. It is a non-linear connection, where for higher values of the flow through the hydropower plant; the highest values for power production are obtained.

CONCLUSION

Within the scope of the paper, the procedures for creating a simulation model and models with machine learning are described, with the aim of understanding the correlation of the target parameters on the variables in the management process of a complex hydropower system, with a "case study" of the Crna Reka basin, for the planned pump storage HPP Chebren and HPP Galishte.

To understand the impact on the target parameters of the management variables with the individual reservoirs, machine learning models were built using the SOLDIER application, developed by the CIMNE Institute in Barcelona, Spain.

To form a sequence of data to train the model with machine learning, a simulation model was

prepared in HEC ResSim for the complex hydropower system Chebren-Galishte. From the model, the hydrographs of inflow into the reservoirs, reservoir outflow, delivered water for irrigation and time series of hydropower production were calculated, in order to form dependencies for the water management of the reservoirs with the help of the SOLDIER application.

Four reservoirs are included in the models: Chebren, Orlov Kamen, Galishte and Tikvesh. Of the specified reservoirs, the Tikvesh reservoir is existing, while the rest are planned reservoirs with hydropower plants. HPP Chebren is planned as a pumped-storage plant, and as such it is included in the study case.

For each reservoir, a separate model was created in SOLDIER, through which the impact of the individual variables on the target parameter – hydropower production is perceived.

From the conducted analyses, it can be concluded that in all models a solid relationship was established between the variables and the target parameter, and as an indicator of the relationship is the R^2 coefficient, which in all models is approximately 1, i.e. it ranges from 0.94 - 1 in the different models.

According to the carried out analytical procedure, at the PSHPP Chebren for the hydropower production, it can be concluded that there is a dominant correlation with the parameter hydropower plant flow. Also, logical results can be seen from the obtained dependencies – with an increase in the water level in the Chebren reservoir and with an increase in the inflow into the reservoir, the power production increases, while the overflow decreases. The water that is required to be pumped from the lower pool (Orlov Kamen reservoir) to the upper pool (Chebren reservoir) increases with the lowering of the water level in the Chebren reservoir.

At the Galishte reservoir, the dependencies are similar – the higher the water levels in the reservoir, the higher the power production, and the overflow decreases with the increase in power production.

The situation is identical with the Tikvesh reservoir - with an increase in the water level in the reservoir, a greater amount of power is generated.

In this initial phase of the research, the sensitivity of the target parameters from the simulation models by changing the variables is investigated, and it can be concluded that solid correlative dependencies have been established, which contribute to an improved study and understanding of the variables dependence in a complex hydropower system.

REFERENCES

[1] "Copernicus Land Monitoring Service," European Environment Agency, [Online]. Available: www.land.copernicus.eu.

[2] F. Panovska, "Simulation model for analyses of multi reservoir hydropower scheme" master thesis, Faculty of Civil Engineering, Ss. Cyril and Methodius University in Skopje, 2019.

[3] Водостопанска основа на Р. Македонија, Скопје, 1973.

[4] EXERGIA, "Main report on Optimization of the river Crna Reka, system for power production and preparation for tender documents for concession," 2003.

[5] USACE, "HEC RESSIM User's Manual, ver 3.3," 2021.

[6] АД Електрани на Р.С. Македонија, "Годишен извештај за работата на АД ЕСМ за 2021 година," АД ЕСМ, Скопје, 2021.

[7] F. Salazar, J. Irazabal and A. Conde, SOLDIER: SOLution for Dam behaviour Interpretation and safety evaluation with boosted regression trees, User Manual, 2023.

[8] F. Salazar, J. Irazabal and A. Conde, "SOLDIER: SOLution for Dam behavior Interpretation and safety Evaluation with boosted Regression trees," SoftwareX, vol. 25, 2024.

[9] US Army Corps of Engineers, "HEC ResSim application," [Online]. Available: https://www.hec.usace.army.mil/software/hec-ressim/.

[10] F. Salazar, M. A. Toledo, E. Onate and B. Suarez, "Interpretation of dam deformation and leakage with," Engineering Structures, 2015.

[11] M. A. Hariri-Ardebili and F. Pourkamali-Anaraki, "An Automated Machine Learning Engine with Inverse Analysis," Water, vol. 14, no. 3898, 2022.

[12] "CIMNE" [Online]. Available: https://www.cimne.com/.

[13] A.-M. Ali Najah Ahmed, O. A Karim, A. El-Shafie and A. El-Shafie, "Application of artificial neural networks for water quality prediction," Neural computing and applications, 2012.

[14] H. Robert Maier and G. Clyde Dandy, "Neural networks for the prediction and forecasting of water resources variables: A review of modelling issues and applications," Environmental Modelling & Software, pp. 101-124, 2000.

[15] F. Schulze, H. Wolf, H. Jansen and P. Van der Veer, "Applications of artificial neural networks

in integrated," Water Science & Technology, vol. 52, no. 9, pp. 21-31, 2005.

[16] A. A. Ahmed, S. Sayed, A. Abdoulhalik, S. Moutari and L. Oyedele, "Applications of machine learning to water resources management: A review of present status and future opportunities," Journal of Cleaner Production, vol. 441, 2024.

Marija Galevska
MSc, Civil Engineer
N. Macedonia
marijagalevska99@gmail.com

Simona Bogoevska
PhD, Assistant Professor
Ss. Cyril and Methodius University in Skopje
Faculty of Civil Engineering
N. Macedonia

Kristina Milkova
PhD, Assistant Professor
Ss. Cyril and Methodius University in Skopje
Faculty of Civil Engineering
N. Macedonia

Sergey Churilov
PhD, Professor
Ss. Cyril and Methodius University in Skopje
Faculty of Civil Engineering
N. Macedonia

Elena Dumova Jovanoska
PhD, Professor
Ss. Cyril and Methodius University in Skopje
Faculty of Civil Engineering
N. Macedonia

Scientific Journal of Civil Engineering (SJCE)

HUMAN COMFORT IN BUILDINGS: AUTOMATION OF THE VIBRATION DOSE VALUE METHOD

DOI: https://www.doi.org/10.55302/SJCE2421329g

Smart buildings, as dynamic ecosystems, integrate cross-dependent sensors to enhance structural serviceability, optimize efficiency, and improve safety. This research employs a custom-designed sensor prototype to explore the feasibility of developing an automated system for evaluating building sensitivity to traffic-induced vibrations. The methodology involves collecting acceleration data from a full-scale structure subjected to traffic vibrations, processing it through an automated algorithm, and categorizing buildings qualitatively based on vibration levels and human perception, as defined by the Vibration Dose Value (VDV) method in the BS 6472-1 standard. Comparative analyses reveal the method's sensitivity to signal duration and amplitude variations, highlighting its potential for integration into real-time smart monitoring systems.

Keywords: traffic-induced vibrations, vibration dose value, vibration measurement, human comfort, acceleration amplitude, smart monitoring systems.

1. INTRODUCTION

In modern urban environments, vibrations caused by traffic — both from road and railway systems — are a common issue that can significantly impact building structures and occupant comfort. Vibrations in buildings often lead to negative effects, including cracks, plaster detachment, and in extreme cases, structural damage. In addition, the simultaneous presence of noise and vibrations can further disrupt occupant comfort, affecting both acoustic and visual well-being. According to studies such as [16], human perception of vibrations is influenced by factors like resonance frequencies, which are critical for understanding how building occupants experience these disturbances.

Numerous studies have analyzed traffic-induced vibrations, focusing on their measurement and impact in high-traffic urban areas [1], [2], [10], [11]. These investigations emphasize the importance of minimizing dynamic loading to meet the threshold levels

set by various standards, such as the British Standard BS 6472-1 and ISO standards [8], [9]. Measures proposed to mitigate vibration effects include retrofitting buildings with appropriate insulation [13], [15], and using in-situ measurements to assess ground-level vibrations, which are then incorporated into structural design models [12], [7], [14]. These approaches ensure that structures meet serviceability requirements and safeguard occupant comfort.

Various standards, including the ISO and British standards, focus on evaluating the sensitivity of buildings to vibrations and their impact on occupant comfort. These guidelines are primarily based on the calculation of a weighted acceleration value derived from measured time records. Other standards, such as the NBC 2005, provide specific recommendations for maximum acceleration limits based on the type of building [4]. The European Standard EN 1990, which addresses the dynamic effects of vibrations, suggests that the natural frequency of a structure be limited to prevent exceeding the serviceability limit state, with further detailed assessments available through ISO standards [5], [6].

This paper investigates the vibration levels in a building exposed to traffic-induced vibrations, analyzing the effects on occupants based on recorded acceleration signals. Specifically, it examines the British Standard BS 6472-1 [3] and the robustness of the Vibration Dose Value (VDV) method for vibration assessment. Two key factors are studied: (1) the impact of signal duration and (2) the influence of peak amplitude on vibration perception. The findings offer valuable insights into the potential for automating the analysis within real-time smart monitoring systems.

The prototype sensor used in this study could be further developed into a "smart" sensor, capable of monitoring a range of environmental factors such as temperature, humidity, and vibrations. This advancement would enhance the role of such sensors in "smart" buildings, ultimately improving structural serviceability, efficiency, and occupant safety.

2. OVERVIEW OF THE BRITISH STANDARD BS 6472-1 METHODOLOGY

The British Standard BS 6472-1 [3] offers a systematic approach for predicting and assessing human responses to vibrations within the frequency range of 0.5 Hz to 80 Hz. By categorizing vibration time histories, the standard accommodates diverse scenarios:

- Continuous vibrations – sustained vibrations over extended periods, such as those caused by consistent traffic flow.
- Periodic vibrations – vibrations occurring at regular intervals, often associated with industrial machinery.
- Occasional vibrations – irregular or infrequent vibrations, such as those caused by sporadic construction activities.

Traffic-induced vibrations are typically classified as continuous, characterized by fluctuating amplitudes throughout the measurement period.

To account for human perceptual sensitivity, the standard [3] incorporates frequency-dependent weighting factors. These factors adjust recorded acceleration signals to reflect the human body's differential sensitivity to vibrations. For vertical movements, the Wb factor is applied, emphasizing the range of 4 to 12.5 Hz. For horizontal movements, the Wd factor is used, capturing sensitivity within 1 to 2 Hz. These adjustments, presented in one-third octave bands, align with the physiological perception thresholds of vibration. Their linear values are graphically represented in Figure 1.

The primary parameter for assessing the effects of vibrations on occupants is the Vibration Dose Value (VDV). This parameter considers the cumulative effect of vibration amplitude over time and is particularly sensitive to peak amplitudes due to its reliance on a fourth-power calculation. The VDV is defined as:

$$\mathrm{VDV}_{\mathrm{b/d,day/night}} = \left(\int_0^{\mathrm{T}} \mathrm{a}^4(\mathrm{t})\mathrm{dt}\right)^{0.25} \quad (1)$$

Here, $\mathrm{VDV}_{\mathrm{b/d,day/night}}$ represents the vibration dose value for the specified weighting and time period (day or night), expressed in $m/s^{1.75}$ for translational vibrations or $rad/s^{1.75}$ for rotational vibrations; $\mathrm{a}(\mathrm{t})$ represents the weighted acceleration as a function of time, expressed in m/s^2 for translational vibrations or rad/s^2 for rotational vibrations; T represents the duration of a measurement period during which vibration can occur, expressed in s.

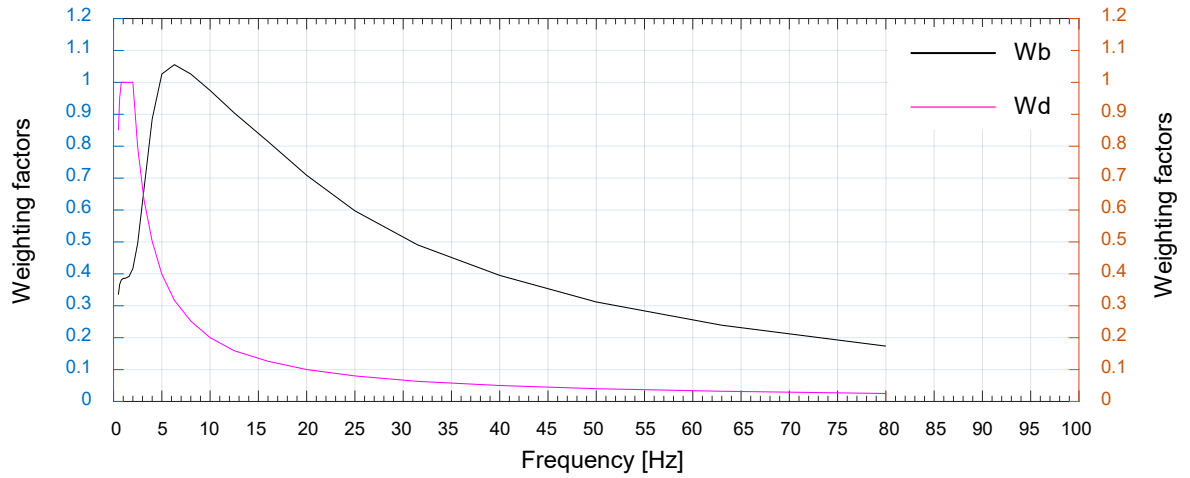

Figure 1. Weighting factors according to BS 6472-1

If the vibration signal consists of multiple intervals with varying durations (e.g., traffic-induced vibrations), the total VDV is calculated as:

$$\mathrm{VDV}_{\mathrm{b/d,day/night}} = \left(\sum_{n=1}^{N} \mathrm{VDV}_{t_n}^4\right)^{0.25} \quad (2)$$

where N represents the total number of time intervals; VDV_{t_n} represents the vibration dose value for the time interval t_n, expressed in $m/s^{1.75}$ for translational vibrations or $rad/s^{1.75}$ for rotational vibrations; t_n represents the duration of n_{th} time interval, expressed in s.

The process of calculating the VDV is outlined in the accompanying block diagram (Figure 2).

Once the VDV is calculated, the standard [3] provides threshold values to interpret its significance. These thresholds categorize the likelihood of adverse comments from building occupants. Lower VDV values indicate minimal risk of negative feedback, while higher values suggest a higher probability of dissatisfaction. The variability in human sensitivity and expectations accounts for the broad ranges specified in the standard, which inherently limits the precision of the assessment.

By integrating these guidelines, the British Standard BS 6472-1 provides a robust framework for quantifying and mitigating vibration effects on building occupants. This study leverages its methodology to assess the sensitivity of an exposed structure, with implications for advancing automated monitoring systems.

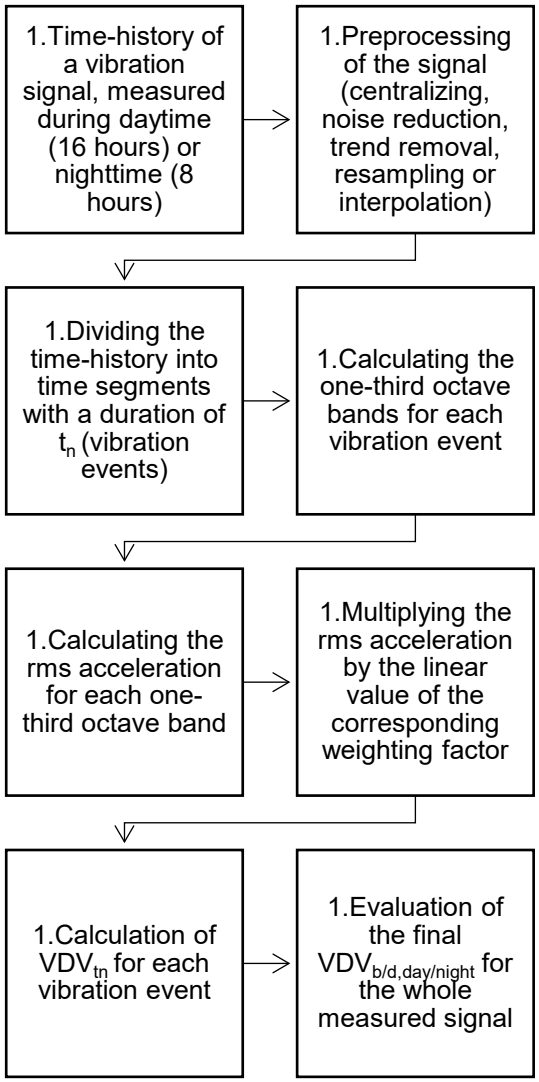

Figure 2. Step by step methodology

3. EXPERIMENTAL CASE STUDY ON BUILDING VIBRATION RESPONSE TO TRAFFIC STIMULI

3.1. CONCEPT DEVELOPMENT

This concept, which forms part of the SmartBuild research project supported by the University of Ss. Cyril and Methodius in Skopje, explores the development of methodologies for utilizing sensor technology in the smart monitoring of various environmental parameters, including temperature, humidity, and vibration levels in buildings. Such a methodology aims to enhance insights into building performance and facilitate data-driven decision-making through real-time monitoring and analysis.

The vibration-based monitoring system proposed in this study focuses on creating a methodology for an automatic system that is triggered when vibration amplitudes surpass predefined acceleration threshold values. Upon activation, the system would record the corresponding vibration events, storing the acceleration histories. These recorded signals would be automatically processed through an algorithm that estimates the Vibration Dose Value (VDV) and provides the user with a qualitative assessment of the vibration levels. The procedure is outlined schematically in Figure 3, and can be divided into four primary phases: (1) measuring of vibrations and time-history acquisition; (2) preprocessing of the signal and preparing the raw data for more detailed analysis; (3) processing of the signal in time domain and frequency domain; (4) obtaining of final results and evaluation. This algorithm could be fully automated via a programming platform, allowing users to adjust input parameters such as the duration of time intervals (t_n) or the acceleration amplitude cut-off threshold. Additionally, constants could be used for values such as one-third octave bands' frequencies, linear weighting factors, and the limit values for qualitative evaluation.

3.2. DESCRIPTION OF THE EXPERIMENTAL SETUP

The experimental setup in this study involved the use of a custom-designed prototype by Digitex Systems [17], representing a smart structural monitoring system composed of two main components.

The first component is the measuring instrument – a prototype three-axis accelerometer called Pulse (Figure 4). This device features three channels, two for horizontal axes and one for the vertical axis. The accelerometer has a sensitivity of 900 mV/g and is equipped with an analog low-pass anti-aliasing filter to reduce band noise and limit the bandwidth. This filter provides a fixed 3 dB bandwidth of approximately 1 kHz (selectable). The Pulse device requires electrical power, which is supplied via a USB connection.

The second component of the system is Voyager, a cloud-based software platform for data collection and processing (Figure 4). Voyager facilitates real-time data collection, management, and analysis from all sensor units connected in the monitoring system. Data communication between Pulse and Voyager is established via Wi-Fi, ensuring continuous data transfer and remote monitoring.

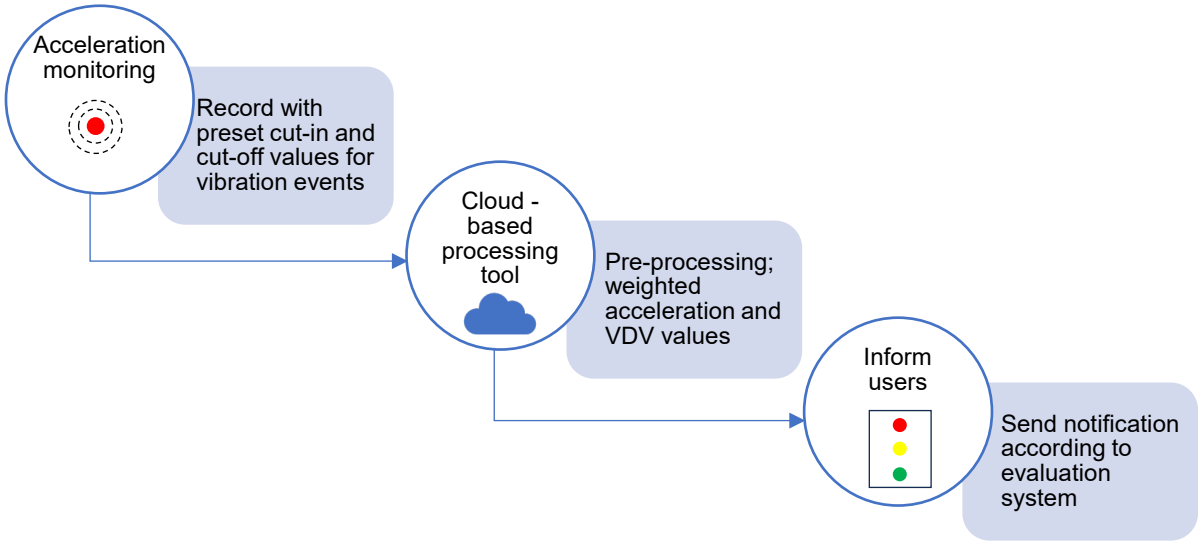

Figure 3. Concept for the automated algorithm for calculating the VDV parameter

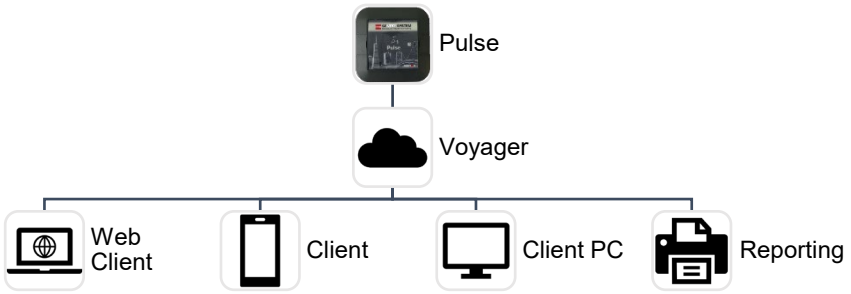

Figure 4. Pulse - Voyager system (adopted from [17])

Following the guidelines outlined in the British Standard [3], the accelerometer was positioned at floor level within a room of the building exposed to traffic-induced vibrations (Figure 5). The building is located along a boulevard with high traffic frequency. The sensor was placed directly on the floor (without being fixed) and connected to the cloud-based software via Wi-Fi for real-time data transmission. During the monitoring period, the building was unoccupied and not in use.

Figure 5. Placement of measuring instrument

To assess the sensitivity of the applied methods and tools regarding measurement duration and exposure time, a 16-hour daytime period was selected based on the recommendations from the standard [3]. In total, 96 acceleration time histories, each lasting 10 minutes, were collected. The recording frequency was set to 200 samples per second, allowing for the extraction of frequencies below 100 Hz. The recorded data was subsequently processed using a custom algorithm developed in the MATLAB programming environment.

3.3. IMPACT OF TIME DURATION AND SIGNAL AMPLITUDE ON VIBRATION ANALYSIS

Determining how the length and amplitude of the measured acceleration signal affect the estimated VDV parameter is crucial for an effective autonomous algorithm, especially in defining the threshold values for cut-in and cut-out amplitude levels that determine vibration events (step 3 of the proposed methodology in Figure 2).

Regarding the time length of the vibration events t_n, three different analyses were conducted for each direction, using signals that include the identified peak acceleration amplitude. The durations analyzed were: 600 seconds (the duration of the entire 10-minute signal), 100 seconds, and 20 seconds. For clarity, only the results from the X and Z directions will be presented here. In the results shown in Figure 6, the three vibration events correspond to the periods during which the maximum acceleration amplitude (from the entire 16-hour signal) occurs.

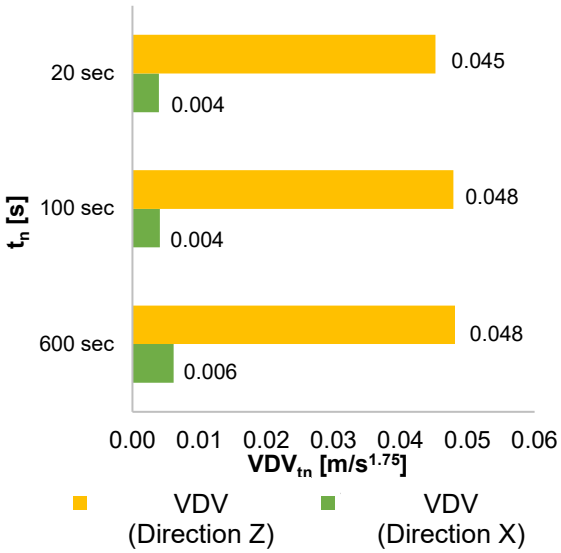

Figure 6. Results for parameter VDV_{tn} depending on direction and time of integration

The linear values of the applied weighting factors (compared to those proposed in the ISO standards), along with the frequency domain representation of the signal, are shown in Figure 7 for direction X and Figure 8 for direction Z.

A possible simplification is to automatically preset the algorithm to assess time slots with identified absolute maximum accelerations within a 16-hour monitoring period. To examine how the magnitude of the amplitude affects the VDV_{tn} parameter in relation to the length of vibration events, all 10-minute records from the 16-hour measurement period were assessed using the three time-lengths: 600 seconds, 100 seconds, and 20 seconds, each of which included the maximum peak occurring in the corresponding record. The graphical representations of these results are shown in Figures 9 and 10, where the maximum VDV_{tn} values are also marked.

The linear trendlines show that, generally, the VDV_{tn} values increase as the maximum acceleration in the vibration event increases. However, it is noteworthy that in some pairs of adjacent amplitudes on the graphs, the VDV_{tn} value is lower when analyzing the time record with the larger amplitude (as observed in the X direction, the maximum VDV_{tn} value is calculated for a vibration event in which the maximum acceleration is lower than the greatest peak in entire signal). This occurs because other significant peaks are present in the time segment of the analyzed record, in addition to the one with the greatest value. These additional peaks have considerably high acceleration values, which contribute significantly to the final integration of values when determining the VDV_{tn} value.

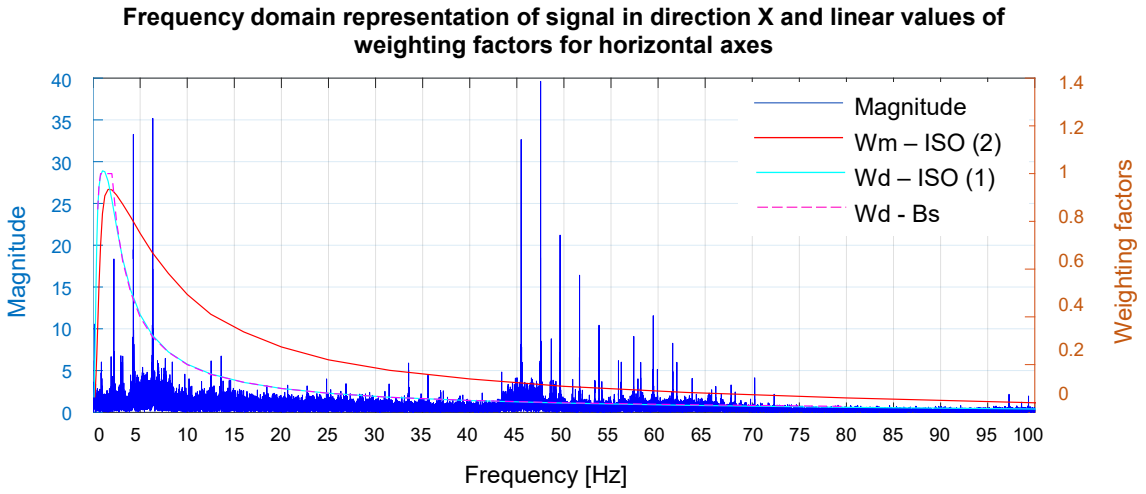

Figure 7. Linear values of weighting factors for horizontal axes and frequency domain representation of signal in direction X

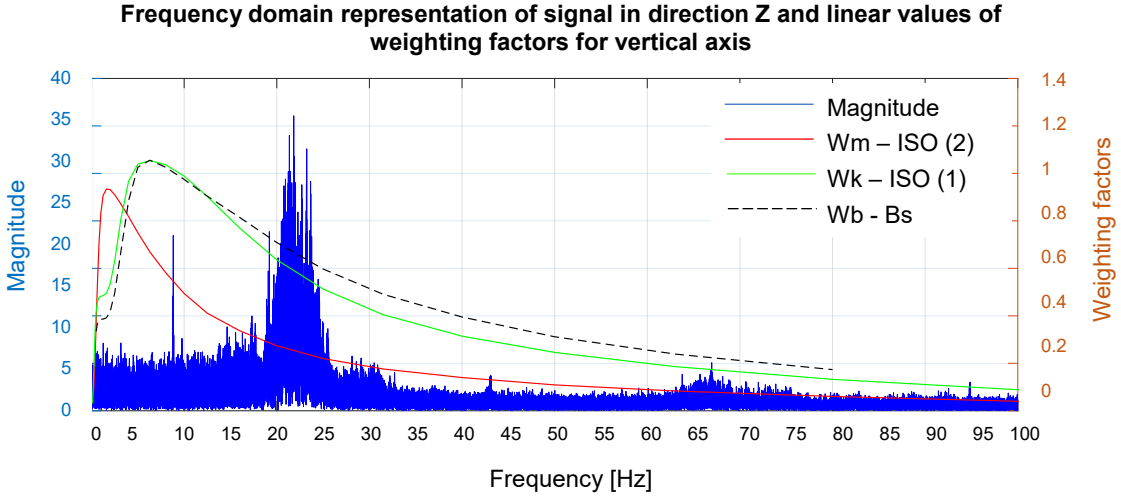

Figure 8. Linear values of weighting factors for vertical axis and frequency domain representation of signal in direction Z

Thus, although the records may contain accelerations that are slightly lower than the maximum, the final result shows a higher VDV_{tn} value compared to cases where only one amplitude is considered, accompanied by much lower accelerations.

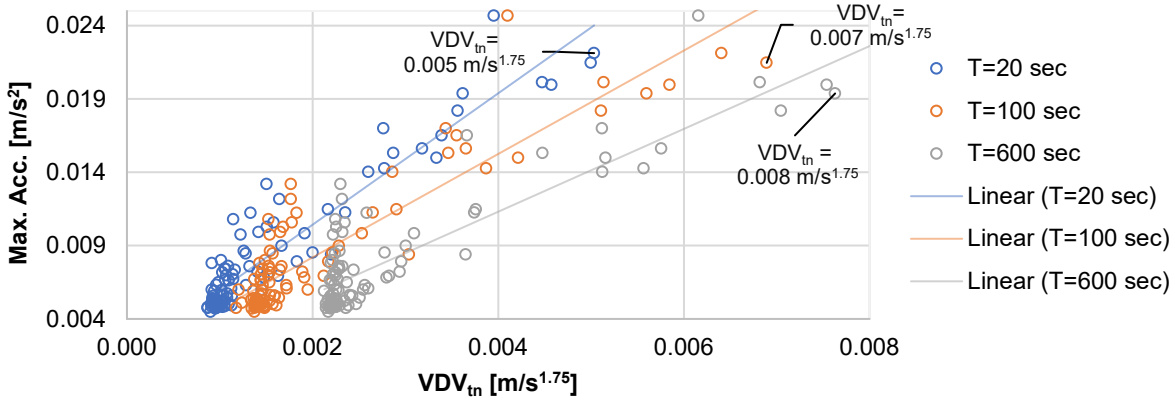

Figure 9. Impact of the length and the amplitude of the time signal on the VDV_{tn} value, direction X

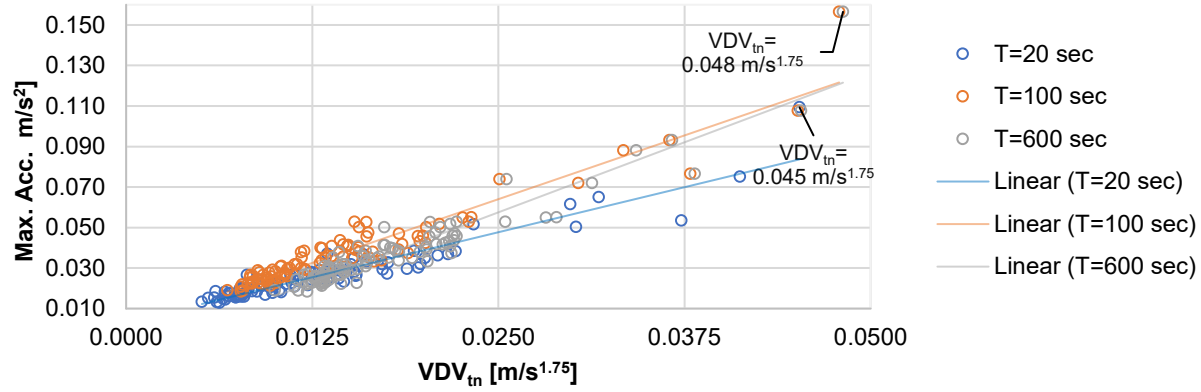

Figure 10. Impact of the length and the amplitude of the time signal on the VDV_{tn} value, direction Z

3.4. IMPACT ASSESSMENT BASED ON PROBABILITY OF ADVERSE HUMAN RESPONSE

Based on the calculated VDV_{tn} values for t_n=600 s (which produced the highest values compared to the shorter time slots), and applying equation (2), a final evaluation of the results for the 16-hour daytime exposure period is provided in Table 1.

This shows that according to the standard [3], no negative effects occur from the examined stimulus.

Table 1. Evaluation according to BS 6472-1

Direction	X	Z
Place and period of measurement	Residential buildings, 16 hours-daytime	Residential buildings, 16 hours-daytime
Calculated VDV	0.013 $m/s^{1.75}$	0.071 $m/s^{1.75}$
Lowest limit value	0.2 $m/s^{1.75}$	0.2 $m/s^{1.75}$
Effect	No adverse comments expected	No adverse comments expected

4. CONCLUSIONS

This study investigates the application of the British Standard BS 6472-1 for assessing the impact of traffic-induced vibrations on buildings, with a focus on developing an autonomous monitoring methodology. Using a prototype triaxial accelerometer, a 16-hour monitoring period was conducted on a building floor exposed to vibrations from nearby traffic. The measured time histories were analyzed to calculate the Vibration Dose Value (VDV) for various vibration events of different durations.

The results demonstrated that the VDV values were not significantly influenced by the various duration of the vibration events, suggesting that the methodology robust across different time intervals. The final assessment indicated no adverse effects from the vibrations, with all values falling below the prescribed limits in the standard. This supports the potential of the proposed methodology for assessing human response to building vibrations in real-time.

Future work will expand on this concept by incorporating multiple accelerometers for more comprehensive data collection, long-term monitoring to build a larger dataset, and controlled traffic exposure to better simulate real-world conditions. Additionally, the development of a refined algorithm with pre-set thresholds for automatic detection of vibration events will further enhance the efficiency and accuracy of the system.

Acknowledgements

The authors are grateful for the invaluable support received from Digitex Systems in providing prototype sensing equipment and technical support throughout the conducted research. This research was conducted within the framework of the SmartBuild research project, University of Ss. Cyril and Methodius University in Skopje.

REFERENCES

[1] Beben D. et al. (2022), "Influence of Traffic-Induced Vibrations on Humans and Residential Buildings – A Case Study", International Journal of Environmental Research and Public Health.

[2] Bongiovanni G. et al. (2011), "Traffic-induced vibrations in historical buildings", 8th International Conference on Structural Dynamics, EURODYN, pp. 812-819.

[3] British Standards Institution (2008), "Guide to evaluation of human exposure to vibration in buildings – Part 1: Vibration sources other than blasting".

[4] Buerau of Indian Standards (2005), "National building code of India".

[5] European Committee for Standardization (2005), „Eurocode – Basis of structural design".

[6] Feldmann M. et al. (2009), "Design of floor structures for human induced vibrations", Office for Official Publications of the European Communities, 64 p..

[7] He L., Tao Z. (2024), „Building Vibration Measurement and Prediction during Train Operations", Buildings Journal.

[8] International Organization for Standardization (1997), "Mechanical vibration and shock – Evaluation of human exposure to whole-body vibration – Part 1: General requirements".

[9] International Organization for Standardization (2003), "Mechanical vibration and shock – Evaluation of human exposure to whole-body vibration – Part 2: Vibration in buildings (1 Hz to 80 Hz)".

[10] Jakubczyk-Galczynska A., Jankowski R. (2014), "Traffic-induced vibrations. The impact on buildings and people", The 9th International Conference "Environmental Engineering".

[11] Kowalska-Koczwara A., Stypula K. (2017), "A comparative analysis of two methods for determining the influence of vibrations on people in buildings", Technical Transactions 1/2017, pp. 53-64.

[12] Koziol K. (2019), "Designing of Buildings in the aspect of prediction of people from traffic included vibrations", IOP Conference Series: Materials Science and Engineering, 7 p..

[13] Koziol K., Stypula K., Tatara T. (2017), "Prediction and Experimental Analysis of the Effectiveness of Vibration-Isolating Tramway", International Conference on Structural Dynamics, EURODYN, pp. 1810-1815.

[14] Liu Y. Lu Z., Yan X., Liu Z., Tang L. (2021), "Measurement and modelling of the vibration induced by working equipment of an offshore platform", Ocean Engineering, Volume 219.

[15] Rosao V., Carreira A. (2014), "Use of vibration measurements to determine the most suitable locations to improve sound insulation in buildings", The 21st International Congress on Sound and Vibration.

[16] Trolle A., Marquis-Favre C., Parizet E. (2015), "Perception and Annoyance Due to Vibrations in Dwellings Generated from Ground Transportation: A Review", Journal of low frequency noise, vibration and active control, Vol.34 No.4, pp. 413-458.

[17] www.digitexsystems.com

PSINSAR-BASED DEFORMATION ANALYSIS IN THE SKOPJE AREA

Tome Gegovski
MSc in Geodesy
Teaching Assistant
Ss. Cyril and Methodius University in Skopje
Faculty of Civil Engineering
N. Macedonia
gegovski@gf.ukim.edu.mk

Zlatko Bogdanovski
PhD, Associate professor
Ss. Cyril and Methodius University in Skopje
Faculty of Civil Engineering
N. Macedonia

DOI: https://www.doi.org/10.55302/SJCE2421337g

PSInSAR is a multi-interferogram InSAR technique used to determine small displacements in urban environments, utilizing satellite SAR images.

This paper presents the fundamental characteristics of the PSInSAR technique and its application for determining displacements in the Skopje region using 101 Sentinel-1 images.

Keywords: PSInSAR, Skopje area, Sentinel-1, deformation, geodynamics.

1. INTRODUCTION

The monitoring of Earth's crust deformations, resulting from constant seismic processes impacting its surface, is a crucial and increasingly popular field within geodesy, known as geodynamics. Geodynamics has emerged as a distinct discipline focusing on the dynamic changes in the Earth's crust and mantle. The application of traditional geodetic methods for this purpose is often limited, as these methods are not always suited for detailed and frequent monitoring over large areas.

Advances in satellite technology have opened up new possibilities for overcoming previous limitations in monitoring Earth's crust deformations. One well-known geodetic approach for this is GNSS. However, in recent years, SAR (Synthetic Aperture Radar) has gained prominence as a modern technology in remote sensing. SAR captures images that can be used to assess deformations through SAR Interferometry (InSAR), a radar-based technique. InSAR techniques rely on identifying phase differences, or the interferometric phase, in pixels from two SAR images taken at different times to measure surface deformation.

The interferometric phase consists of multiple components, among which the deformation and topographic components are the most important for modeling. However, these are often masked by phase influences caused by atmospheric effects and various signal noises. The topographic component can be modeled using a Digital Elevation Model (DEM), a technique known as Differential InSAR (DInSAR). However, to monitor subtle 'silent displacements' of seismic origin, other

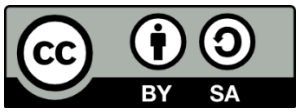

components must also be considered, complicating the process further.

One of the most well-known InSAR techniques, which addresses the additional components of the interferometric phase and offers the highest accuracy in measuring Earth's crust deformations, is PSInSAR (Permanent Scatterer InSAR). This paper presents the fundamental characteristics of the PSInSAR approach, supported by a real analysis of the Skopje basin using 101 Sentinel-1 SAR images from 2016 to 2024.

2. ADVANCED MULTI-INTERFEROGRAM TECHNIQUE PSINSAR

2.1. FUNDAMENTAL INSAR CONCEPT

The interferometric phase consists of several components, as expressed in relation (1):

$$\Delta\varphi = \Delta\varphi_{flat} + \Delta\varphi_{elev.} + \Delta\varphi_{disp.} + \Delta\varphi_{atm.} + \Delta\varphi_{n.} \quad (1)$$

The first component, $\Delta\varphi_{flat}$, is not a significant issue for modern SAR satellites, as it can be relatively easily modeled and removed from the interferometric phase. The elevation component, $\Delta\varphi_{elev.}$, is generally corrected using a DEM, however, errors in the DEM or the limited sensitivity of SAR images to this component can still affect the interferometric phase, leading to potential inaccuracies.[2] [10]

The deformation component, $\Delta\varphi_{disp.}$, is the primary focus of this research. However, various atmospheric conditions during the acquisition of SAR images ($\Delta\varphi_{atm.}$), as well as noise ($\Delta\varphi_{n.}$) in the images leading to decorrelation, have a significant impact on the interferometric phase [10].

2.2. THE NEED FOR MULTI-INTERFEROGRAM TECHNIQUE

In [4], we presented the fundamental characteristics of SAR interferometry, which is a relatively new acquisition method. Due to its unique features, it stands out as the only method capable of accurately determining deformations over large areas.

SAR interferometry is a very promising technology, however, it is affected by a series of important problems. Firstly, interferograms are prone to decorrelation, either temporal or geometrical. Secondly, the interferometric phase is wrapped, making it difficult to unwrap accurately using a single interferogram. Additionally, if the topography of the area of interest is not known with sufficient precision, distinguishing between residual topography and actual terrain displacement becomes a challenging task. Finally, even when these issues are addressed, atmospheric artifacts can severely bias the detected signals, undermining the overall analysis. [7]

These challenges highlight the need for advanced approaches, such as multi-Interferogram InSAR techniques like PSInSAR, which provide a robust framework to overcome these limitations and enhance the accuracy of deformation measurements.

2.2. PERMANENT SCATTERER INSAR

The Permanent Scatterer InSAR technique is based on the assumption that atmospheric effects on phase values are spatially correlated in each acquisition, while the deformation component is temporally correlated. This allows for the estimation and removal of the Atmospheric Phase Screen (APS) from each SAR acquisition, thanks to the network of PS points. [9]

The technique consists of the following steps:

1. Creation of differential interferograms;
2. Selection of PS candidates;
3. Spatial-temporal modeling;
4. Phase demodulation and network adjustment of PS points.

2.2.1 Creation of differential interferograms

Since this is a multi-interferogram technique, the first step is to create N interferograms from N+1 SAR acquisitions.

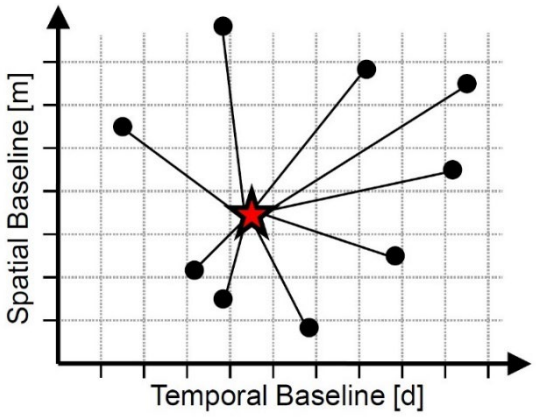

Figure 1. Schematic representation of interferogram generation in PSInSAR. [1]

All interferograms are generated using the same reference image. The choice of the reference image is determined by the need to create interferograms with the smallest

possible spatial and temporal baselines (Figure 1).

The spatial baselines refer to the normal baseline distance between the satellite positions during the two acquisitions. The temporal baseline refers to the time interval between the two acquisitions. In each interferogram, the topographic component is modeled and removed using a digital elevation model (DEM). This type of interferogram is called a **differential interferogram**, and the technique is known as **DInSAR**.

2.2.2 Selection of PS candidates

A Permanent Scatterer (PS) point refers to a scatterer within the resolution cell whose scattering vector has the highest intensity. This results in the resolution cell having a high Signal-to-Noise Ratio (SNR) and a stable phase value over time. As shown in Figure 2, one of the scatterers exhibits a high amplitude value, which is attributed to a high level of reflection.

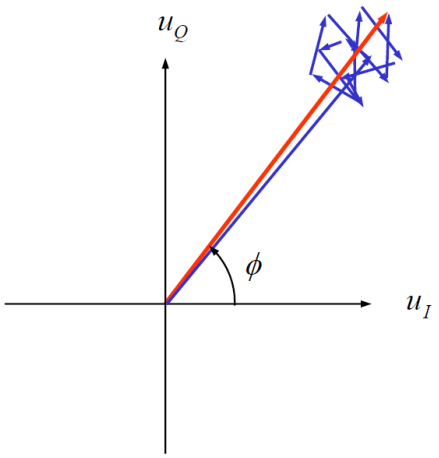

Figure 2. Representation of a Permanent Scatterer within the resolution cell [5]

High amplitude values are observed in scatterers within the resolution cell where dihedral scattering occurs. In this case, almost all the energy reaching that resolution cell is reflected back toward the sensor (Figure3A).

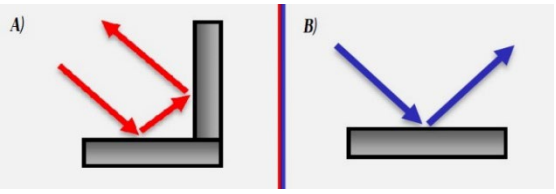

Figure 3. A) Dihedral Scattering B) Specular Scattering

Dihedral scattering most commonly occurs in urban areas, as this type of scattering is characteristic of objects such as buildings. Therefore, PS points are predominantly found in urban environments. However, it can also occasionally occur in rocky terrains.

A very important characteristic of PS points is that they have a stable phase over time, which is not the case with other pixels, such as **DS (Distributed Scatterers).** (Figure 4)

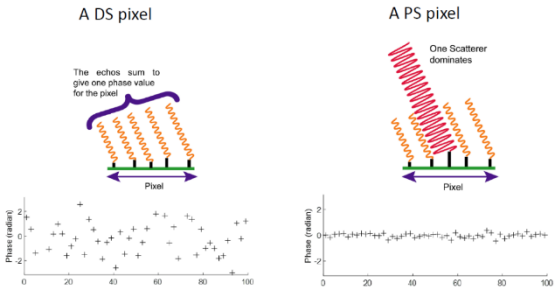

Figure 4. Representation of phase variation in PS and DS pixels. [5]

In the PSInSAR algorithm, a simple solution is proposed for detecting PS points in all N interferograms, based on the determination of the **Amplitude Dispersion Index (DAI)**, which is calculated according to relation (2).

$$D_A = 1 - \frac{\sigma_A}{\mu_A} \qquad (2)$$

Where:

σ_A – The standard deviation of the amplitude of pixel P across all N interferograms. μ_A– The mean amplitude of pixel P across all N interferograms.

The Amplitude Dispersion Index is calculated for each pixel across all N interferograms. In this process, all SAR images, specifically the layer of the image containing all amplitude values, must be radiometrically calibrated. The selection of PS candidates refers to those pixels with an Amplitude Dispersion Index greater than 0.4 (when using the STaMPS algorithm). To obtain reliable values, at least 30 SAR images are required.

2.2.3 Spatial-temporal modeling

The selection of PS points refers to the process of choosing pixels where the interferometric phase in all created differential interferograms is significantly freed from the systematic influence of phase decorrelation (n), which is reduced to random error ($\Delta\varphi_{n.}$).

On the other hand, the topographic component ($\Delta\varphi_{elev.}$) has already been modeled and largely removed in the creation of differential interferograms. However, errors in elevation must still be considered, and this component will be further treated as a systematic influence, which will depend on the size of the

interferogram's baseline. As for the deformation component it is important to note that its determination is only possible if it is assumed that the displacement is **linear over time**. This assumption limits the application of this technique to areas where deformations follow a linear trend over time. In general, the total deformation is decomposed into two components: linear and nonlinear deformation, where the assumption is that the nonlinear deformation has minimal impact on the overall interferometric phase.

According to the above, the interferometric phase in the i-th interferogram for each PS point is determined according to relation (3):

$$\varphi_i = W\left\{\underbrace{\frac{4\pi}{\lambda}\cdot v\cdot \Delta t}_{\varphi_{def}} + \underbrace{\frac{4\pi}{\lambda}\cdot\frac{B_n}{R\cdot\sin(\theta)}h_{err}}_{\varphi_{topo}} + d_{NL} + \alpha + n_{res}\right\} \quad (3)$$

Where:

W – Modulated interferometric phase with a 2π modulus (Wrapping operator).

$\frac{4\pi}{\lambda}$ – Wavelength conversion factor (λ) into a 2π modulus, multiplied by 2 due to the round-trip signal path from the sensor to the Earth's surface and back.

v – Speed of displacement of the deformation vector (usually expressed in mm/year).

Δt– Temporal baseline of the i-th interferogram.

B_n–Normal baseline distance between the satellite positions in the two acquisitions. For modern satellites, it is calculated with very high accuracy. (Figure 1)

h_{err}–Mean elevation error of the PS (taken from the DEM).

R – Distance from the sensor to the Earth's surface.

θ – Acquisition angle.

d_{NL}–Component related to nonlinear deformation.

α–Component related to non-identical atmospheric effects in the two acquisitions.

n_{res}–Component related to residual phase decorrelation. It is typically a small, insignificant value after selecting the PS points.

According to one of the assumptions of the PSInSAR technique, which involves the spatial correlation of atmospheric influences, this means that the atmospheric components of the interferometric phases at two neighboring PS points will have identical or very similar values. Their difference will be largely free from atmospheric effects. Moreover, this difference will reflect the relative speed of the linear deformation component and the relative elevation errors at the two points. Therefore, the difference in the interferometric phases between neighboring PS points A and B in the i-th interferogram is expressed according to relation (4):

$$\Delta\varphi_{i_A}^{B} = W\left\{\left[\underbrace{\frac{4\pi}{\lambda}\cdot\Delta t\cdot\Delta\boldsymbol{v_A^B}}_{\varphi_{def}} + \underbrace{C\cdot B_n\cdot\Delta\boldsymbol{h_{err_A}^{\ B}}}_{\varphi_{topo}}\right] + \underbrace{\Delta d_{NL}+\Delta\alpha+\Delta n_{res}}_{phase\ residual\ (\Delta w)}\right\} \quad (4)$$

Where:

Δv_A^B – Relative displacement speed between the two PS points.

C – A constant value for each interferogram, which refers to the product $\frac{4\pi}{\lambda\cdot R\cdot\sin(\theta)}$.

$\Delta h_{err}{}_A^B$ – Relative mean elevation error between the PS pair.

Δd_{NL} – Value of the nonlinear deformation component.

$\Delta\alpha$ – Difference in atmospheric components between two neighboring PS. If the distance between the PS points is <1 km, it is estimated that $\Delta\alpha$ < 0.1 RAD.

The determination of the spatially dependent component of atmospheric influence is determined by at least 3 to 4 PS points within 1 km². Failure to meet this condition is an additional limiting factor for applying the PSInSAR technique in non-urban areas, where vegetated surfaces predominate. In urban environments, typically, the number of PS points exceeds 50 within 1 km². [3]

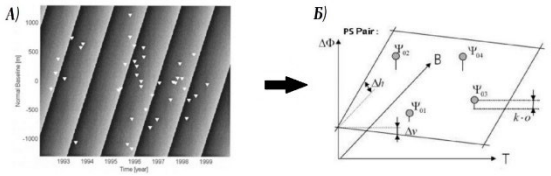

Figure 5. A) Periodogram showing the spatial-temporal dependence; B) Best-fitting 2D plane, whose slopes represent the linear values of the PS pair. [3]

It should be emphasized that the difference in interferometric phase between two points ($\Delta\varphi_{i_A}^{B}$) still has a modulated phase value within 2π. According to relation (4), the problem is reduced to an equation with two dependent unknowns between the two neighboring PS points, namely:

- Relative speed of the linear deformation component (Δv_A^B), which depends on the temporal baseline Δt;

- Relative elevation error ($\Delta h_{err}{}_A^B$), which depends on the normal baseline distance (Bn).

Assuming that the values for Δv_A^B and $\Delta h_{err}{}_A^B$ are known, the phase residual (Δw) in relation (4) must satisfy the condition (Δw < 0.6).

After determining the values for Δv_A^B and $\Delta h_{err}{}_A^B$, these values are substituted into relation (4), and the phase residual (Δw) is obtained. Based on this, the **temporal coherence (γ)** is calculated, which must be higher than the minimum allowed value (γ_0 = 0.9), satisfying the condition ($\gamma > \gamma_0$). The multi-interferogram coherence ranges from 0 to 1 and is calculated according to relation (5):

$$\gamma = \left| \frac{\sum_{i=1}^{N} e^{j\Delta w}}{N} \right| \quad (5)$$

All PS pairs that, after determining the relative deformation velocities and relative elevation errors, do not satisfy the condition ($\gamma > \gamma_0$) will not proceed to the next step. However, those pairs that meet the condition will participate in the next integration step with a γ-weight.

2.2.4 Phase demodulation and network adjustment of PS points

After determining the values of Δv and Δh_{err} for each pair in the PS point network, these values need to be phase unwrapped according to one of the phase unwrapping algorithms. The most commonly used phase unwrapping algorithm is the SNAPHU algorithm.

Once the unwrapped values of Δv and Δh_{err} for each PS pair are determined, they need to be integrated to obtain absolute values. The process of obtaining the absolute values of the deformation velocity and elevation error for each PS point is done using one of the geodetic network adjustment methods with a datum at a single point (the reference PS point). The most commonly used method is the indirect adjustment using the least squares method.

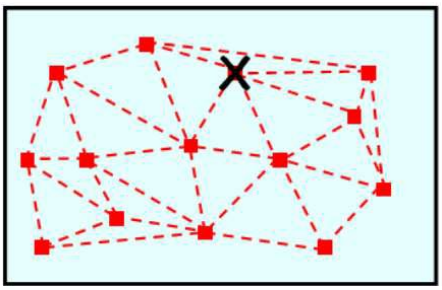

Figure 6. PS network integration [6]

Two separate adjustments are made: one to determine the deformation velocity of the PS points and another to determine the mean elevation errors of the PS points. In the indirect adjustment, the number of measurements equals the number of PS pairs, which represent relative deformation velocity or relative elevation error measurements.

3. PSINSAR FOR THE SKOPJE AREA

3.1. ACQUISITION OF SAR IMAGES

The first step in conducting a PSInSAR analysis is obtaining SAR images. Sentinel-1 images, which are part of the Copernicus program of the European Space Agency (ESA), provide global coverage and are freely available, making them ideal for large-area analysis and long-term deformation monitoring. Users can easily access these data through platforms such as ASF DAAC Vertex or Copernicus Open Access Hub, where the images can be downloaded in various formats.

Given the circumstances, the choice was limited to using exclusively Sentinel-1 SAR images. For this purpose, a total of 101 images were downloaded from the ASF DAAC Vertex platform for the territory of Skopje, from a descending orbit, covering the period from November 11, 2015, to March 16, 2024.

Additionally, the following parameters were used when selecting the images.

Table 1. Parameters used for obtaining SAR images

Orbit type	*Descending*
SAR image type	*L1 SLC*
Beam mode	*IW*
Polarization	*VV*
Orbital path number	80
Frame number	453

4.2. SELECTION OF THE REFERENCE IMAGE AND CREATION OF DIFFERENTIAL INTERFEROGRAMS

In the PSInSAR analysis process, the selection of the reference image plays a crucial role in the accuracy of the final results. For the purposes of this analysis, the image from October 27, 2019, was selected based on several criteria, such as the stability of atmospheric conditions and the quality of the image. Additionally, when selecting the reference image, careful consideration was given to the effects of the

temporal and normal baseline vectors between the reference and secondary images. (Figure 7)

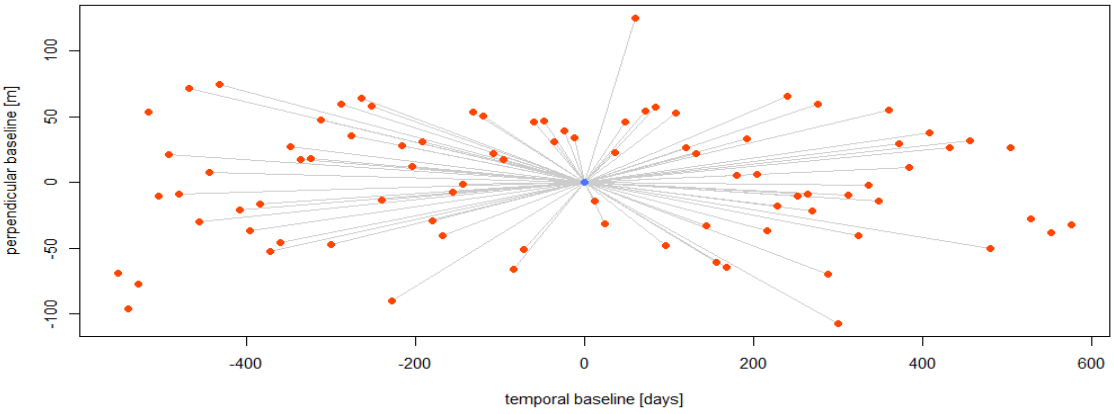

Figure 7. PSInSAR graph of the connection between the reference and secondary images.

It is primarily important to note that for the PSInSAR analysis, the **STaMPS** (Stanford Method for Persistent Scatterers) algorithm, developed by Stanford University, was used. This algorithm is specialized for identifying and analyzing PS points. However, for the creation of differential interferograms, the SNAP (Sentinel Application Platform) software was used, which allows for SAR image processing and data preparation for further analysis with STaMPS.

The process of creating differential interferograms begins with loading the reference and secondary SAR images into the SNAP software, from which a total of 100 differential interferograms will be generated. The first step in the processing is preprocessing, which involves selecting one of the three sub-swaths of the Sentinel-1 images, as well as selecting a precise orbit for the acquisition of the images. The choice of sub-swath is significant as it facilitates processing, since the processing will not be performed on the entire image.

The next step is geocoding each image, where the images are transformed from pixel coordinates to geographic coordinates, enabling their accurate spatial alignment. Radiometric corrections are then applied to improve the spectral characteristics of the images, which is important for further analysis and for reducing noise and some atmospheric effects.

After geocoding and enhancing the spectral characteristics, differential interferograms are generated by comparing each secondary image with the reference image. This enables the calculation of phase differences, which are used to detect deformations. Additionally, reflectivity maps are created for the amplitude values of each secondary image. These maps are utilized to calculate the amplitude dispersion index, which aids in selecting stable ground points (Persistent Scatterers - PS) for analysis.

Since Sentinel-1 images are captured across multiple sub-swaths and bursts, a debursting process is required to synthesize all the strips from each sub-swath into a single continuous image. Furthermore, it is possible to select specific strips to further simplify processing.

The aforementioned process is computationally and time-intensive, as it needs to be performed for all 100 differential interferograms. To streamline and automate the workflow, Python scripts from the *snap2stamps* package were employed. This enabled the automatic generation and processing of differential interferograms. As a result, the entire process was consolidated into two graphs, significantly simplifying the generation of differential interferograms.

It is important to emphasize that the differential interferograms were not created for the entire area of the SAR images, but rather for the region defined by the following WGS 84 ellipsoidal coordinates, listed in Table 2.

Table 2. WGS84 Coordinates of the Area of Interest Subject to PSInSAR Analysis

Longitude minimum	*21° 19’ 15”*
Latitude minimum	*41° 56’ 05”*
Longitude maximum	*21° 39’ 10”*
Latitude maximum	*42° 03’ 35”*

4.3. PSINSAR USING THE STAMPS ALGORITHM

We have already defined that the PSInSAR technique consists of four steps. Through the previous activities in the SNAP software, we generated the differential interferograms, where the interferometric phase includes the components from relation (3).

The PS approach begins by utilizing only those pixels with a high coefficient of the Amplitude Dispersion Index (ADI), defined by relation (2). Since this ADI ranges from 0 to 1, high coefficients are considered to be values above 0.7, indicating a high likelihood of stable phase values. However, this approach may exclude many other pixels with stable phase values but lower ADI coefficients. Therefore, when using the STaMPS algorithm, it is recommended that PS candidates have an ADI of at least 0.4.

The STaMPS algorithm begins precisely with this activity: defining PS candidates, where the $\Delta\varphi_{noise}$ component is either eliminated or has an insignificant influence in relation (3). This is achieved using the *mt_prep_snap* command in a Linux environment. With this command, the algorithm calculates the ADI coefficient for each pixel in the defined area and retains only those pixels with a value above 0.4, referred to as PS candidates.

The STaMPS algorithm is MATLAB-oriented and consists of eight steps:

1. Loading PS candidates: Initial processing of identified PS candidates.
2. Temporal coherence calculation: Calculating the temporal coherence for each PS candidate.
3. PS point selection: Final selection of PS points based on coherence and stability.
4. PS point filtering (PS weeding): Removing redundant or low-quality PS points.
5. Phase correction: Addressing potential phase inconsistencies.
6. Phase unwrapping: Resolving phase ambiguities for the selected PS points.
7. Determination of spatially correlated error components: Correcting errors related to the acquisition angle.
8. Atmospheric filtering of secondary images: Mitigating atmospheric effects across the processed images. [8]

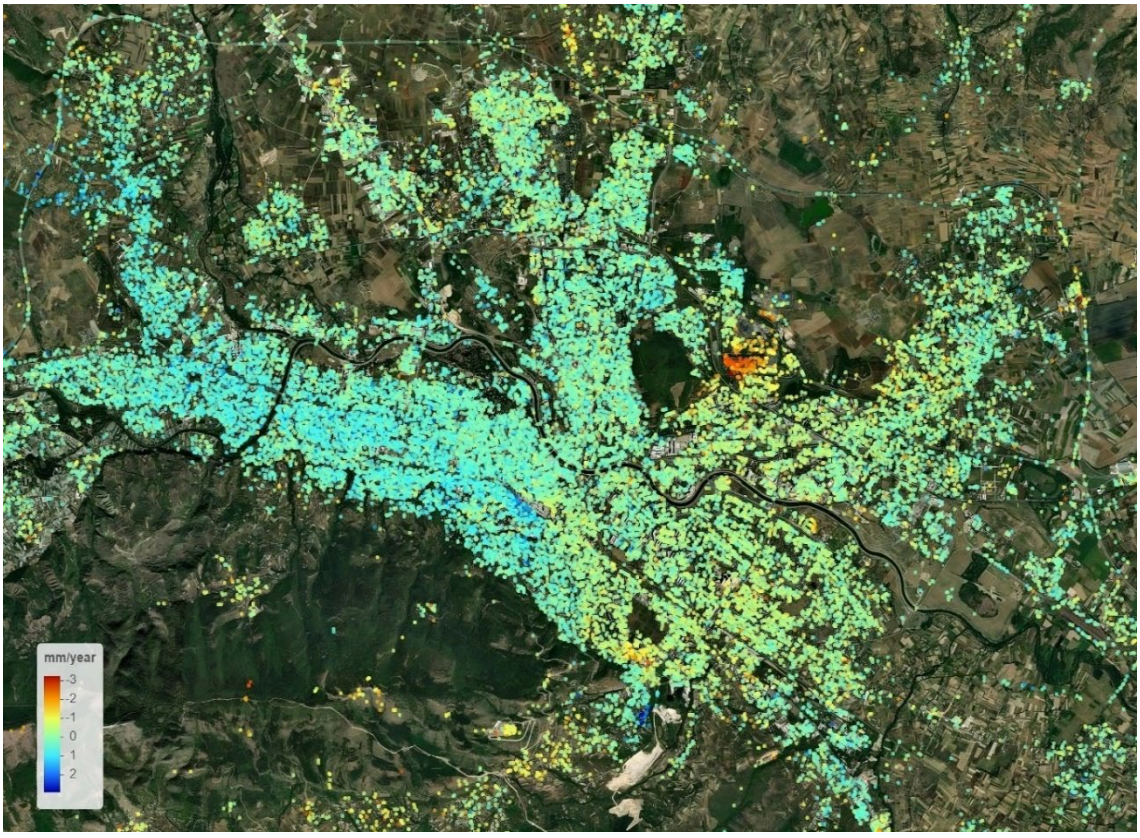

Figure 8. Deformation Results from the Conducted PSInSAR Analysis for the Skopje Basin Displayed in the STaMPS Visualizer Software

After processing all the aforementioned stepsthe $\Delta\varphi_{disp}$ was isolated from the other components in the interferometric phase across all **26 384 PS points**. It is important to note that only linear displacements over time are determined, modeled by the following equation:

$$\Delta\varphi_{disp} = \frac{4\pi}{\lambda}\Delta v B_T \quad (6)$$

From equation (6), it can be observed that the linear deformations are determined as the displacement velocity (Δv) in millimeters per year in the acquisition direction.

From Figure 8, the displacements in the Line of Sight (LOS) direction are clearly shown, which in essence slightly differ from the vertical displacements. The results of the PSInSAR analysis indicate that the PS points are mainly positioned in the urban area of the city, as the objects exhibit the characteristics of permanent scatterers (PS). According to Figure 8, in the western part of the Skopje basin, PS points with light blue color dominate, indicating an uplift of 1mm/year, while in the eastern part of the Skopje basin, PS points with a yellowish color prevail, indicating a subsidence of 1mm/year.

4. CONCLUSION

This paper briefly presents the fundamental characteristics of InSAR, with an emphasis on PSInSAR, as the most accurate InSAR technique for determining surface deformations. All of this is supported by a PSInSAR analysis for the territory of Skopje. The results of the PSInSAR analysis clearly show that there is a slight relative displacement between the western and eastern parts of the city, in opposite directions. The western part is moving towards the satellite, indicating a slow uplift of the surface with an average velocity of approximately 1mm/year for the PS points, while the eastern part is moving in the opposite direction, indicating slow subsidence of the surface with an average velocity of around 1mm/year for the PS points. These results provide additional motivation to continue research in the field of InSAR, using additional SAR images, applying different PSInSAR algorithms, and certainly adopting a multidisciplinary approach to interpret the causes of such displacements.

Additionally, further investigation into the long-term trends and potential correlations with other geophysical data could lead to a more comprehensive understanding of the underlying factors contributing to these surface deformations, such as geological activity, urban expansion, or human-induced changes.

REFERENCES

[1] ASF. (2023). Radar Community ASF. Retrieved from GEOS 657 Microwave Remote Sensing: https://radar.community.uaf.edu/

[2] EO59. (2024). Advance InSAR training course supported by SARPROZ PSInSAR algorithm.

[3] Ferretti, A., & Rocca, F. (2000). Analysis of Permanent Scatterers in SAR interferometry. IEEE Transactions on Geoscience and Remote Sensing.

[4] Gegovski, T., Bogdanovski, Z., & Kasapovski, F. (2022). A REVIEW OF INSAR TECHNOLOGY FOR DETERMINATION OF SURFACE DEFORMATION. SJCE, 13-19.

[5] Hooper, A. J. (2006). PERSISTENT SCATTERER RADAR INTERFEROMETRY FOR CRUSTAL DEFORMATION STUDIES AND MODELING OF VOLCANIC DEFORMATION.

[6] Minh, D. H. (2021). InSAR course supported by IGARSS.

[7] Perissin, D. (2014). Interferometric SAR MultiTemporal processing (techniques and applications).

[8] RUS Copernicus. (2022). StaMPS: Persistent Scatterer Interferometry Processing. ESA.

[9] UAF University of Alaska Fairbanks. (2024). GEOS F639 901 202401 (CRN 35703) InSAR and Its Applications. Retrieved from https://canvas.alaska.edu/courses/18500

[10] Woodhouse, I. H. (2006). Introduction to Microwave Remote Sensing. CRC Press.

LOCAL GEOID DETERMINATION IN WESTERN MACEDONIA BY LSMSA METHOD

Filip Petrovski
MSc in Geodesy
Teaching Assistant
Ss. Cyril and Methodius University in Skopje
Faculty of Civil Engineering
N. Macedonia
petrovski@gf.ukim.edu.mk

Zlatko Bogdanovski
PhD, Associate Professor
Ss. Cyril and Methodius University in Skopje
Faculty of Civil Engineering
N. Macedonia

Ramazan Alpay Abbak
PhD, Professor
Konya Technical University
Faculty of Engineering and Natural Sciences–
Department of Geomatics Engineering – Konya
Republic of Turkye

DOI: https://www.doi.org/10.55302/SJCE2421345p

This paper presents the fundamental components of the Least Squares Modification of the Stokes integral with Additive corrections (LSMSA) to geoid determination. This method also known as the KTH method is theoretically described, then it is applied to the western part of North Macedonia. In this regard, input data is firstly explained, and then various geoid models are created in the test area. Finally, all geoid models are evaluated against the ground truth to get a final geoid model. Numerical results indicate that despite of limited terrestrial gravity data, a precise geoid model by LSMSA method is computed in the test area.

Keywords: additive corrections, digital elevation model, geopotential model, gravity anomalies, KTH method

1. INTRODUCTION

Along with Earth's topographic surface and ellipsoid, the geoid is one of the three main surfaces in geodesy. The geoid is the reference surface for physical heights. It can be described with many definitions and one of them is: "The geoid is the equipotential surface of the Earth's gravity field that most closely coincides with the undisturbed mean sea level (and its continuation through the continents). Disturbances are caused by ocean tides, streams, winds, variations in salinity and temperature, of the order of ± 2 m" [1].

The geoid is a physical surface, and its best approximation is the mean sea level. The geoid model plays an essential role in many engineering and scientific applications, such as:

- Reference surface for leveling,
- Vertical datum for orthometric heights,
- Transformation of ellipsoidal (geometrical) to orthometric heights (physical),
- Studies of the Earth's interior and ocean,
- Research for deposits of oil and gas etc.

One of the main uses of geoid model is for transformation of ellipsoidal heights obtained by *GNSS (Global Navigation Satellite System)* to physically meaningful orthometric heights by,

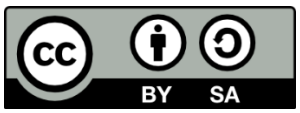

$$H = h - N \quad (1)$$

The geoid undulations N are defining the geoid model and they can be interpreted as the differences between the orthometric height (measured along the plumb line from the geoid) and ellipsoidal height (measured along the ellipsoidal normal line from reference ellipsoid). The type of measurement method for obtaining height differences which consists of measuring ellipsoidal heights h using GNSS and geoid undulations N from geoid model is called GNSS levelling. This method is intended as a replacement to the classical levelling using a pair of rods and it could save time and cost (Fig. 1).

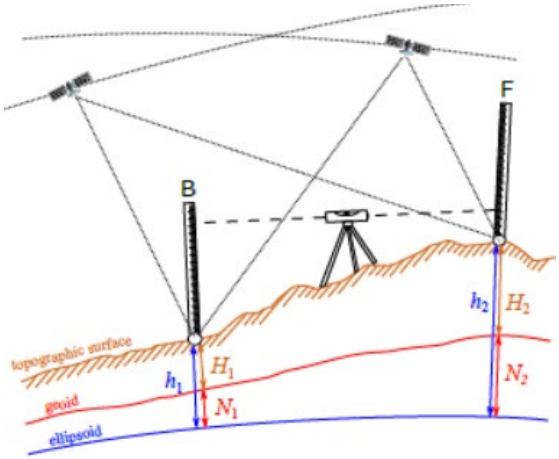

Figure 1. Determination of height differences using classical levelling and GNSS levelling

The main aim of this paper is to obtain a local gravimetric geoid model as accurate as possible. To the best of our knowledge, there has not been any precise gravimetric geoid model in our test area.

The methodology and input data for determining a geoid model will be explained in the next sections. Then, numerical applications will be realized in the western part of Makedonia. Lastly, comparison results will be discussed in the final section.

2. BASIC CHARACTERISTICS OF THE LSMSA METHOD

Least Squares Modification of Stokes formula with Additive corrections (LSMSA) is developed at the Royal Institute of Technology in Sweden by L. E. Sjöberg [9]. It is one of frequently used methods for determination of a geoid model [1,6,7,13]. In this approach, terrestrial free-air anomalies and global geopotential models are combined for calculation of the approximate geoid undulations. Then, the additive corrections are computed separately and added to the previously computed approximate undulations to get the final geoid model.

Let's start with the fundamental equation in the physical geodesy, which is the Stokes formula for determining geoid undulations:

$$N = \frac{R}{4\pi\gamma}\iint_{\sigma} S(\psi)\Delta g d\sigma \quad (2)$$

This is the Stokes kernel to determine the undulation on a sphere as a body that approximates the Earth, but the Earth is not a sphere. Thus, Sjöberg [8,12] did some modifications and the eq. (2) is rewritten as:

$$\tilde{N} = \frac{R}{4\pi\gamma}\iint_{\sigma 0} S_L(\psi)\Delta g d\sigma + \frac{R}{2\gamma}\sum_{n=2}^{M} b_n \Delta g_n \quad (3)$$

where Δg is the free-air anomaly, $\sigma 0$ is the cap with a spherical radius ψ_o, S_L is modified Stokes kernel, Δg_n is the free-air anomaly from GGM (Global Geopotential Models).

Since the integration should be done to the whole sphere according to Stokes formula, we need the gravity anomalies for whole Earth. Eventually, we only have the gravity measurements for specific target area, while the other gravity anomalies are gathered from the GGMs. Therefore, the modification of the original Stokes kernel was needed.

Considering assumptions above, the final geoid model is given as follows:

$$N = \tilde{N} + \delta N_{top}^{comb} + \delta N_{DWC} + \delta N_{atm} + \delta N_{ell} \quad (4)$$

where $\tilde{N}$ represents the approximate geoid undulations (eq. 3), $\delta N_{\mathrm{top}}^{\mathrm{comb}}$ represents the combined topographic correction, δN_{DWC} represents the downward continuation correction, δN_{atm} is the atmospheric correction and δN_{ell} is the ellipsoidal correction.

The combined topographic correction [11] is carried out by the orthometric height of the point,

$$\delta N_{comb}^{Top} = -\frac{2\pi G\rho H^2}{\gamma}\left(1 + \frac{2H}{3R}\right) \quad (2)$$

This correction has the largest impact of all four corrections and its value can be in the range of decimeters. Moreover, interested reader can exploit actual topographic density instead of the standard density (2670 kg/m^3) to gain more precise results [e.g. 1].

The downward continuation correction [10] of the gravity anomalies can be expressed as,

$$\delta N_{dwc}^{(1)} = \frac{\Delta g_P}{\gamma} H_P + 3\frac{\tilde{N}}{r_p} H_P - \frac{1}{2\gamma}\frac{\partial \Delta g}{\partial r}\Big|_P H_P^2 \quad (3)$$

$$\delta N_{dwc}^{L1,Far} = \frac{R}{2\gamma}\Sigma_{n=2}^{M} b_n \left[\left(\frac{R}{r_P}\right)^{n+2} - 1\right] \Delta g_n \quad (4)$$

$$\delta N_{dwc}^{L2} = \frac{R}{4\pi\gamma}\iint_{\sigma_o} S^L(\psi)\left[\frac{\partial \Delta g}{\partial r}\Big|_Q (H_P - H_Q)\right] d\sigma_o \quad (5)$$

The value of this correction is in the range of several centimeters.

The atmospheric correction is computed by [8]:

$$\delta N_{comb}^{Atm} = -\frac{GR\rho^a}{\gamma}\iint_{\sigma 0} S^L(\psi) H_P d\sigma_o \quad (6)$$

The ellipsoidal correction [3] due to the Earth's approximation with a sphere, can be simply calculated by,

$$\delta N_{ell} \approx \left[(0.0036 - 0.0109 sin^2\varphi)\Delta g + 0.0050\tilde{N} cos^2\varphi\right] Q_0^L \quad (7)$$

The atmospheric and ellipsoidal corrections are in the range of a few millimeters.

We can conclude several aspects about the calculations:

- The approximate geoid undulations are dependent of the terrestrial gravity anomalies and GGM,
- Topographic correction depends on the digital elevation model (DEM),
- Downward correction depends on DEM GGM, terrestrial gravity anomalies,
- Atmospheric correction depends on DEM,
- Ellipsoidal correction is dependable on the approximate geoid undulations and free-air anomalies.

3. STUDY AREA FOR LOCAL GEOID

The study area for determination of geoid model is located in the western part of the Republic of North Macedonia. The target area is bounded by the points in Tab. 1.

The study area is characterized with a dynamic topography. The minimum, maximum, and average heights are 594, 2102, and 1264 m, respectively.

Table 1: Target area boundaries

Point	ϕ	λ
Southwest	41°18′18″	20°39′18″
Northwest	41°38′42″	20°39′18″
Southeast	41°18′18″	20°59′42″
Northeast	41°38′42″	20°59′42″

For the determination of a local geoid model, three datasets are needed (terrestrial gravity anomalies, GGM, DEM). Some of the data are accessed with the permission from state authorities, namely the National Agency for Cadastre which provides the gravity surveys, GNSS and high precision levelling data. GGM and DEM are publicly available via the webpages ICGEM [4] and Earth Explorer [14], respectively.

The total number of gravity points over the target area is 165, which derivates the terrestrial free-air gravity anomalies (Fig. 2).

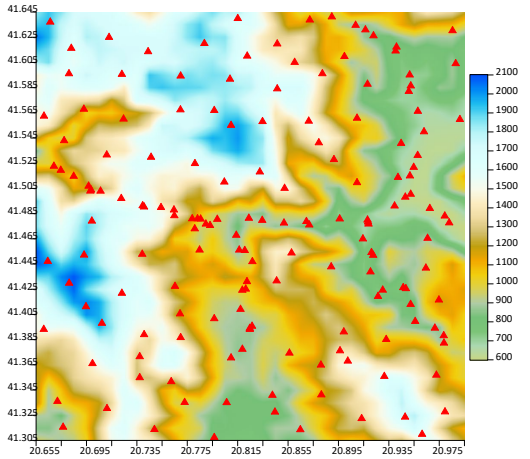

Figure 2: Distribution of terrestrial gravity points in the target area

According to the boundaries, the length of the area is the same as the width of the area, which is 20'24'' (total area equals to 1000 km^2). The density of the gravity data is 1 point per 6 km^2, which is better than a couple of studies showing that good density is approximately 1 point per 10 km^2. From Fig. 2, the gravity data is regularly distributed around the target area.

On the other hand, we have 46 GNSS-levelling benchmarks which can help us derive geometrical geoid undulations using the eq. (1). GNSS-levelling data will be used for fitting the gravimetric geoid model to local vertical datum. In the following sub-sections, GGMs and DEMs which are employed in this study will be treated.

3.1 GLOBAL GEOPOTENTIAL MODELS

Global geopotential models represent the long wavelength information of the Earth's gravity field. The models are represented by a series of spherical harmonics with different degree (n) and order (m). While the maximum harmonic expansion was around 30-40 degrees in the past, today the most detailed models are produced by degree expansion up to 5500 [4]. They are created by the different satellite missions (GRACE, GOCE, CHAMP), terrestrial gravity data as well as topography.

When a geoid model is calculated, the question of which GGM to use always arise. In this situation, there are no restraints on which model to use, but in order to get more accurate model, the GGM that is intended for use should be evaluated by the ground truth in form of gravity anomalies or geometrical geoid undulations. The LSMSA method mostly uses satellite-only GGM. Thus, in our case, the evaluation is carried out on eight satellite-only GGMs (Tab. 2). The choice of these eight models is done by the most recent releases and derivation from two missions such as GRACE, GOCE or GRACE+GOCE models.

Table 2: GGMs used in this study

Name	Year	Max. degree of expansion
Tongji-Grace02k	2018	180
HUST-Grace2016s	2016	160
GOSG02S	2023	300
GO_CONS_GCF_2_TIM_R6	2019	300
GOSG01S	2018	220
WHU-SWPU-GOGR2022S	2023	300
Tongji-GMMG2021S	2022	300
ITU_GGC16	2016	280

From Tab. 2, the maximal expansion for the GGMs is ranging from 160 to 300 degrees. For the validation of the GGMs, we need the gravimetric geoid undulations from the ICGEM calculation center [4] using full expansion for each GGM and the geometrical geoid undulations derived from GNSS-levelling data. The comparison results are listed in Tab. 3.

Table 3: Validation of GGMs on GNSS-levelling points

Name	Absolute validation [cm]		
	Min.	Max.	RMS
Tongji-Grace02k	-105.48	2.92	30.06
HUST-Grace2016s	-174.38	-82.78	25.22
GOSG02S	-39.88	39.61	21.20
GO_CONS_GCF_2_TIM_R6	-41.38	41.02	22.08
GOSG01S	-62.48	15.88	21.60
WHU-SWPU-GOGR2022S	-40.68	38.71	21.21
Tongji-GMMG2021S	-48.18	32.01	21.30
ITU_GGC16	-59.48	23.82	22.21

From Tab. 3, we can conclude which GGM is the best suitable for use in the computation of the geoid model based on the RMS (root mean square error) of the differences between gravimetric (GGM) and geometric (GNSS derived) geoid undulations. Based on the table, we can see that the values are similar to each other. The model that gives smallest RMS is GOSG02S. The worst one is Tongji-Grace02k with RMS of 30.06 cm. In order to eliminate possibly systematic bias in the comparison, we employ corrector surfaces [5, 7]. In this case, 4 parameter is used in this study and results are given in Tab. 4.

Table 4: Fitting of GGMs to GNSS points (4 par. fit)

Name	4 parameter fit [cm]		
	Min.	Max.	RMS
Tongji-Grace02k	-17.15	20.39	6.44
HUST-Grace2016s	-17.10	20.69	6.49
GOSG02S	-17.20	20.37	6.45
GO_CONS_GCF_2_TIM_R6	-17.20	20.26	6.41
GOSG01S	-17.20	20.29	6.39
WHU-SWPU-GOGR2022S	-17.18	20.40	6.44
Tongji-GMMG2021S	-17.21	20.70	6.51
ITU_GGC16	-17.18	20.26	6.41

From Tab. 4, we can see that all GGMs give precise results comparing them with GNSS-levelling points. The GGM that derives smallest RMS is GOSG01S.

3.2 DIGITAL ELEVATION MODELS

Digital elevation model (DEM) is the representation of the Earth's topography as well as the short wavelength variations in the Earth's gravity field. In our case, two mostly used DEMs are employed: SRTM (Shuttle Radar Topography Mission) and ASTER (Advanced Space-borne Thermal Emission and Reflection Radiometer). The technical specifications of the DEMs are available in Tab. 5

Table 5: SRTM and ASTER data [14,15]

Type of info	SRTM	ASTER
Institution	NASA	NASA, METI
Resolution	1''	1''
Horizontal datum	WGS84	WGS84
Vertical datum	EGM96	EGM96

Before using any DEM, it should be evaluated with the ground truth, which means comparison with the 46 levelling points in our case. We need to check the differences between the orthometric heights derived from the DEMs and those measured with classical levelling. The results are shown in the Tab. 6 using the 4-parameter fit because of the different vertical datum between the DEMs (EGM96) and the levelling points (mean sea level).

Table 6: Comparison results of DEMs

Model	Absolute validation – 4 par. fit [cm]		
	Min.	Max.	RMS
SRTM	-131.02	134.7	61.21
ASTER	-131.53	134.31	61.22

The numerical results present same agreement after 4-parameter fitting between both DEMs and levelling points.

4. PRACTICAL COMPUTATION OF LOCAL GEOID MODEL

The input data is gathered in form of terrestrial free-air anomalies, global geopotential models and digital terrain models. In geoid modelling studies, we need the data for the target area and surrounding area. The data area will be within these boundaries in Tab. 7. The data area is 1 degree wider on each side from the boundaries of the target area.

Table 7: Boundaries of data area

Point	ϕ	λ
Southwest	40°18′18″	19°39′18″
Northwest	42°38′42″	19°39′18″
Southeast	40°18′18″	21°59′42″
Northeast	42°38′42″	21°59′42″

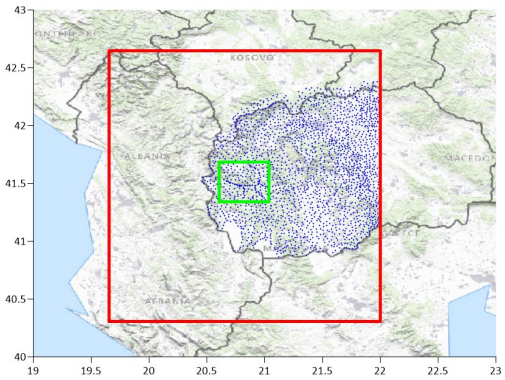

Figure 3: Data and target area

Fig. 3 shows the data area marked with red line, target area with green line, and terrestrial free-air anomalies marked with blue color. Whereas the data coverage is well on the eastern side of the target area, the other parts will be fulfilled with anomalies derived from EGM2008, because it is difficult to obtain the gravity data from the neighboring countries.

For the practical computation of geoid model, LSMSSOFT will be used in this study [1]. The LSMSSOFT starts with three files:

- First one is the GGM file in GFC format that is obtained from ICGEM web page. This file contains the spherical harmonic coefficients up the maximum expansion degree for the selected GGM;
- Second one is the free-air gravity anomaly file. For this one, we have to interpolate gravity anomalies on grid centers using the Bjerhammer rule and nearest neighbor technique. The grid resolution plays an important role since higher resolution is better approximation. Therefore, the resolution of 36 arc-second which equals to 0.01 arc-degrees was chosen in our case.
- Third one is the elevation file consisting of the orthometric heights from DEM. Averaged heights on the grid centers were created for both DEMs. Both the resolution and coverage of elevation data must match the gravity anomaly data.

The LSMSSOFT coded with C++ programming language can be executed on Linux platform

[2]. Several parameters can be chosen arbitrarily to create a geoid model:

- Firstly, we need to determine the maximum degree of expansion for the GGM (e. g. 100, 150, 200, 250, 300)-GOSG02S;
- Secondly, we need to choose the spherical integration cap size (i. e. 0.5 or 1 degree);
- Finally, variance of terrestrial gravity anomalies (e. g. 1, 2, … 30).

Considering these parameters, a wide range of geoid models can be created, and one must be chosen among them. The geoid model giving the smallest RMS is chosen as final geoid model, comparing with the geometric geoid derived from GNSS-leveling points. In our case, the final parameters of maximum expansion degree, cap size and variance of terrestrial gravity anomalies are 300, 1 degree, and 30 mgal^2, respectively.

Table 6: Comparison of gravimetric and geometric geoid models

	Absolute comparison [cm]		
	Min.	Max.	RMS
No fit	56.11	104.26	10.92
4 par. fit	-25.66	11.11	6.16

After comparing the gravimetric and geometric geoid models, we can conclude that the improvement of geoid model using fitting surface is significant from 21.20 cm (Tab. 3) to 10.92 cm (Tab. 7).

Furthermore, after using 4 parameter fitting surface, we can see a remarkable improvement from 10.92 to 6.16 cm. Finally, the hybrid geoid model (gravimetric geoid is fitted to the geometric geoid) is portrayed in Fig. 4.

5. CONCLUSIONS

Based on the presented analysis in the previous sections, the following conclusions can be drawn:

- The more gravity data used in the calculation gives the better results. The aspiration should be to have at least 1 point per 4 km^2.
- The recent satellite GGMs yields the precise results.
- Better and improved DEMs should be included.
- Dozens of geoid models are calculated changing the input parameters.

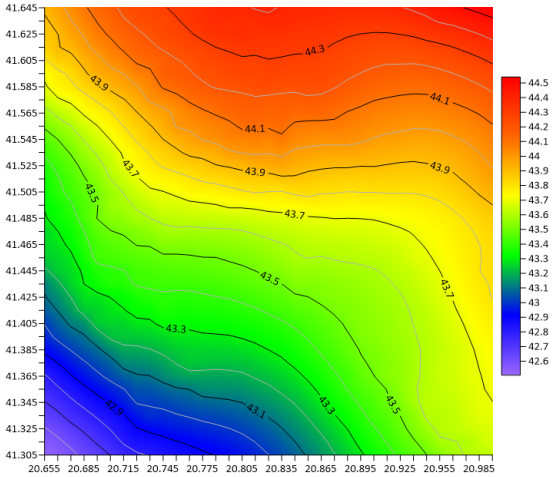

Figure 4: Hybrid geoid model by LSMSA

- The gravimetric geoid model is checked with geometric geoid for the final solution.
- Hybrid geoid model created by parametric surface gives systematic error free model which is usable directly in the test region.

REFERENCES

[1] Abbak, R. A. (2020). Effect of a high-resolution global crustal model on gravimetric geoid determination: a case study in a mountainous region. Studia geophysica et geodaetica, *64*, 436-451.

[2] Abbak R. A. and Üstün A. (2015). A software package for computing a regional gravimetric geoid model by the KTH method. Earth Science Informatics 2015 Vol. 8 Pages 255-265. DOI: 10.1007/s12145-014-0149-3

[3] Ellmann A. and Sjöberg L. (2004). Ellipsoidal correction for the modified Stokes formula. Boll Geod Sci Aff 2004 Vol. 63.

[4] ICGEM (2024). International Centre for Global Earth Models https://icgem.gfz-potsdam.de/home, accessed date: November 21st, 2024

[5] Kotsakis, C. and Sideris M. G. (1999). On the adjustment of combined GPS/levelling/geoid networks. Journal of Geodesy 73(8), 412–421. DOI: 10.1007/s001900050261

[6] Pa'suya, M. F., Din, A. H. M., Yusoff, M. Y. M., Abbak, R. A., & Hamden, M. H. (2021). Refinement of gravimetric geoid model by incorporating terrestrial, marine, and airborne gravity using KTH method. Arabian journal of geosciences, 14, 1-19.

[7] Pa'suya, M. F., Md Din, A. H., Abbak, R. A., Hamden, M. H., Yazid, N. M., Aziz, M. A. C., & Samad, M. A. A. (2022). Hybrid geoid model over peninsular Malaysia (PMHG2020) using two approaches. Studia Geophysica & Geodaetica, 66(2022), 98—123,

[8] Sjöberg L. E. (1999). The IAG approach to the atmospheric geoid correction in Stokes' formula and a new strategy. Journal of Geodesy 1999

Vol. 73 Issue 7 Pages 362-366. DOI: 10.1007/s001900050254

[9] Sjöberg L. E. (2003). A general model for modifying Stokes' formula and its least-squares solution. Journal of Geodesy 2003 Vol. 77 Issue 7 Pages 459-464. DOI: 10.1007/s00190-003-0346-1

[10] Sjöberg L. E. (2003). A solution to the downward continuation effect on the geoid determined by Stokes' formula. Journal of Geodesy 2003 Vol. 77 Issue 1 Pages 94-100. DOI: 10.1007/s00190-002-0306-1

[11] Sjöberg, L. E. (2007). The topographic bias by analytical continuation in physical geodesy. *Journal of Geodesy*, *81*(5), 345-350.

[12] Sjöberg L. E. and Bagherbandi M. (2017). Gravity Inversion and Integration, Theory and Applications in Geodesy and Geophysics. Springer. DOI: 10.1007/978-3-319-50298-4

[13] Krdžalić, D., & Abbak, R. A. (2023). A precise geoid model of Bosnia and Herzegovina by the KTH method and its validation. Survey Review, 55(393), 513-523.

[14] USGS (2024). United States Geological Survey, https://earthexplorer.usgs.gov, accessed date: November 21st, 2024

[15] Üstün, A., Abbak, R. A., & Zeray Öztürk, E. (2018). Height biases of SRTM DEM related to EGM96: from a global perspective to regional practice. *Survey Review*, *50*(358), 26-35.

SELECT A PROFESSION

CREATIVE	SOPHISTICATED	RECOGNIZED	RESPONSIBLE
ENDURING	UP-TO-DATE	WORLWIDE	IMPORTANT

WWW.GF.UKIM.EDU.MK

OUR FACULTY CAN GIVE YOU

IMPULSE !	SCHOLARSHIPS FOR THE BEST	ASSURANCE !	COORPERATION WITH INDUSTRY AND INTERNATIONAL UNIVERSITIES
SIMPLE ENROLLMENT	MOTIVATION !	100% EMPLOYMENT AND INTERNATIONALLY RECOGNIZED DIPLOMA	SUPPORT !

WWW.GF.UKIM.EDU.MK

Ali Muriqi
MSc,Teaching Assistant
University 'Hasim Prishtina', Prishtina
Republic of Kosovo
alishmuriqi@uni-pr.edu

Petar Cvetanovski
PhD, Professor
Ss. Cyril and Methodius University in Skopje
Facuty of Civil Engineering
N. Macedonia

EXPERIMENTAL AND ANALITICAL STUDY OF COMPOSITE BEAMS WITH PROFILED STEEL SHEETING

DOI: https://www.doi.org/10.55302/SJCE2421353m

The paper presents the results of experimental and analytical research on steel-concrete composite beams of floor structures with the application of steel profiled sheet. The parallel and transversal position of the ribs of the profiled sheet in relation to the axis of the steel beam is considered.

A test of the resistance and ductility of the headed stud connectors for parallel and transversal position of profiled sheet was carried out according to a standardized test procedure [4],[5] (EC 4, part 1-1, annex B2).

The main part of the research was carried out with a full-scale testing of two models of a simple beam with a span of 5750 mm, with longitudinal and transversal ribs of the profiled sheet.

For comparison with the experimentally obtained results, an elastic-plastic analysis was applied, carried out with 3D/FM models in the "Abaqus 6.14" software package, using material nonlinearity modeled on the basis of the previously determined behavior of the constituent materials.

Keywords: composite beams, headed stud connectors, steel profiled sheet

1. INTRODUCTION

In the modern construction of multi-story buildings, everywhere in the world, the application of steel structures is frequent. In combination with them, a concrete slab cast on a steel profiled sheet is used as a floor slab.

The slab composed of concrete and steel profiled sheet has several advantages over the classic reinforced concrete slab: the sheet in the concreting phase serves as a formwork for the fresh concrete, the steel sheet can be bonded to the concrete and replaces a good part, or entire required reinforcements in the lower zone of the slab. The profiled sheet can be placed with ribs parallel to the beam, or with ribs transversal to the span of the beam.

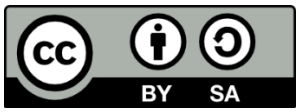

The supporting beams from the floor structure, on which the profiled sheet is directly placed, are usually bonded to the floor slab with headed stud connectors. The headed stud connectors are welded to the steel girder with specialized equipment [7]. There are two general approaches in welding them, directly to the steel beam with holes in the sheet, and welding through the sheet.

A composite simple beam, with a span of 5,75m, made of IPE240 with a concrete slab (d=100mm) cast on a steel profiled sheet (FR38/158 d=1,0mm) placed in the first case parallel to the span of the beam, and in the second case perpendicular to the span of the beam, was considered. For both alternatives, a full-scale model was tested. The testing was carried out in the laboratory for testing of constructions at the Faculty of Civil Engineering from the University "St. Cyril and Methodius" in Skopje.

Headed stud connectors (d=19mm, hc=100mm) type Nelson, without a protective layer of concrete above the head of the connector, were used as means of connection. The resistant of the connectors, which depends on many factors, was examined with a "push" standardized test according to the procedure of EC 4: Part 1-1: Annex B2.

In both tests, modern equipment was used to register the parameters of the structural behaviour under the influence of the test load (force, deformations, strains), as well as for the acquisition of the measured values.

In addition to the experimental investigation of the composite effects, an analytical investigation was also carried out with computer modelling of the test beams in the Abaqus software package. The values obtained from the examination of the constitutive materials (steel and concrete), i.e. the declared values from the attestation documentation (connectors, reinforcement and profiled sheet) were used in the modelling.

The obtained experimental and analytical results in terms of ultimate limit resistance and deformability are compared for the two test models and presented in the form of diagrams, graphs and tables.

The load-bearing capacity of composite beams, using profiled sheet as a formwork for the fresh concrete, depends on a number of factors and is the subject of analytical and experimental investigations. Eurocode 4, part 1-1, provides principles and rules for the design of the ultimate bearing capacity, that is, the plastic bending moment in a characteristic section [4]. The stiffness of the coupled beams is of essential importance for serviceability. Using of elastic shear connectors leads to relevant displacements in the contact plane even for relatively low values of the load [6]. This phenomenon can be determined by experimental investigation, or through complex computer models in which the calibration of parameters are based on experimental results.

2. TESTS ON SHEAR CONNECTORS

When shear connectors are used in T-beams with a constant-thickness concrete slab, or with haunches, the standard push test may be used [2], [8]. In other cases, with longitudinal or transverse placement of profiled steel sheet, a specific push test should be used. In this case, an ordinary sheet was used without indentations or embossments that are used to connect the slab to the sheet [9], [11], [13].

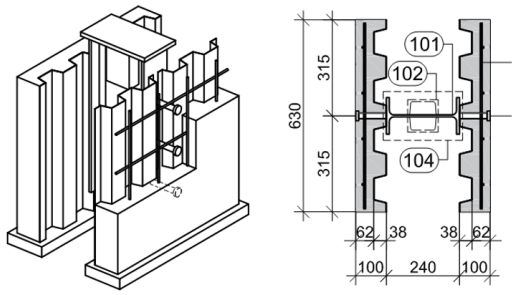

a) parallel ribs

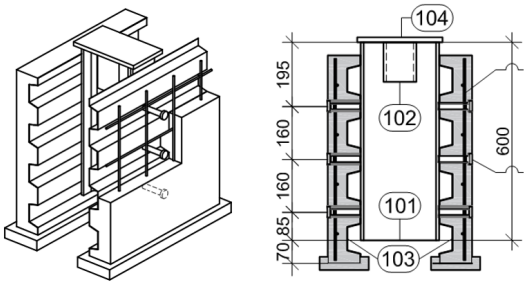

b) transversal ribs

Figure 1. Test specimens for standard push test

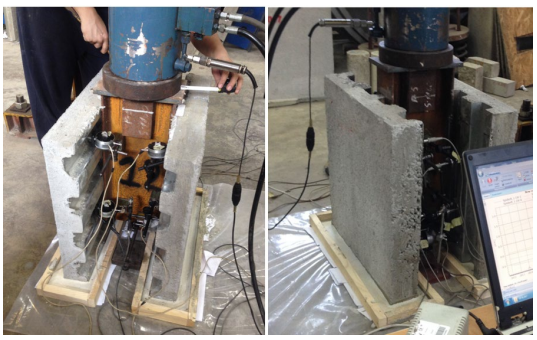

Figure 2. Test equipment

During the test, the applied force and the longitudinal slip between each concrete slab and the steel section are measured, as well as the transverse separation between the steel section and each slab (Fig. 1).

The expected breaking load is obtained by multiplying the design load capacity of the headed stud connector, according to paragraph 6.6.3.1 of EC4-1.1 (1), by the number of applied connectors.

$$P_{Rk} = \frac{0{,}8 \cdot f_u \cdot (\pi \cdot d^2/4)}{\gamma_v} \quad \text{or}$$

$$P_{Rk} = \frac{0{,}29 \cdot \alpha \cdot d^2 \cdot \sqrt{f_{ck} \cdot E_{cm}}}{\gamma_v} \qquad (1)$$

which is smaller, with α=1 for h_{sc}/d=100/19 > 4.

The partial safety factor γ_v is taken equal to 1,0, the specified ultimate tensile strength of the connector material f_u=500MPa, the characteristic cylinder compressive strength of the aged concrete f_{ck}=30MPa, the secant modulus of elasticity of concrete E_{cm}=33000MPa.

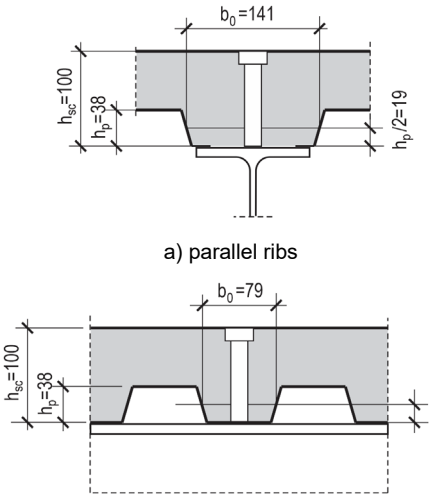

a) parallel ribs

b) transversal ribs

Figure 3. Characteristic geometric values

The shear resistance of the headed stud connector, with the values given in expression (1), is:

$$P_{Rk} = \frac{0{,}8 \cdot 500 \cdot (\pi \cdot 19^2/4)}{1{,}0} = 113{,}35\text{kN} \quad \text{or} \qquad (2)$$

$$P_{Rk} = \frac{0{,}29 \cdot 1{,}0 \cdot 19^2 \sqrt{30 \cdot 33000}}{1{,}0} = 104{,}16\text{kN} \qquad (3)$$

When using a profiled steel sheet with ribs parallel to the beam, the shear resistance should be multiplied by the reduction factor k_l (4), (Fig. 3a).

$$k_\ell = 0{,}6 \cdot \frac{b_0}{h_p} \cdot \left(\frac{h_{sc}}{h_p} - 1 \right) \le 1{,}0 \qquad (4)$$

When using a profiled steel sheet with ribs transversal to the beam, the shear resistance should be multiplied by the reduction factor k_t (5), (Fig. 3b).

$$k_t = \frac{0{,}7}{\sqrt{n_r}} \cdot \frac{b_0}{h_p} \cdot \left(\frac{h_{sc}}{h_p} - 1 \right) \qquad (5)$$

Where n_r is the number of connectors in one rib of the cross section of the beam. Upper limit $k_{t,max}$ for k_t is: $k_{t,max}$=0,85, for n_r=1 and welding through the sheet. The values obtained with the standardized test are given in tab. 1.

Table 1. Measured and calculated forces

Samp. Nb.	Disposition L parallel T transver.	Welding TD through deck H through holes	P_{max} (measured) [kN]	P_{Rk} EC4 [kN]
1.1	L	H	570,3	625,0
1.2	L	H	486,5	625,0
1.3	L	H	520,3	625,0
2.1	T	TD	462,9	531,2
2.2	T	TD	431,8	531,2
2.3	T	TD	399,9	531,2

The following graphs present the measured maximum force for each sample and the P-δ relation.

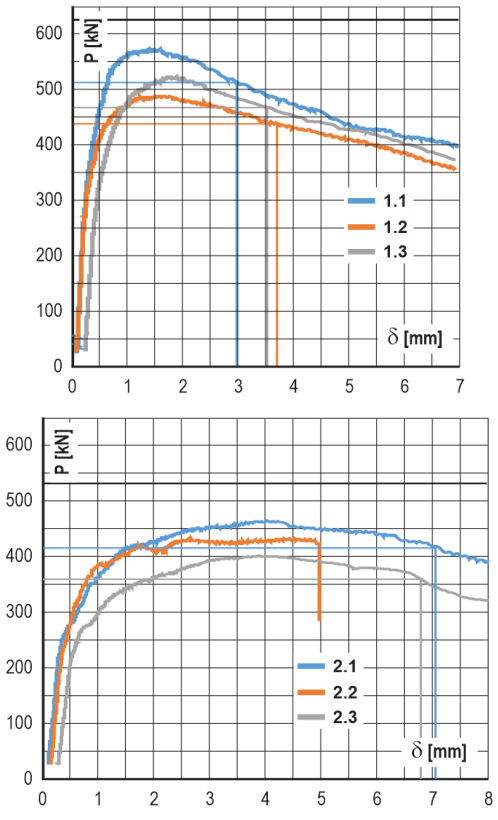

Figure 4. P-δ diagrams of the tested samples

The horizontal line shows the expected maximum force. The ductile behaviour of the headed stud connectors, according to EC4, requires a sliding capacity of at least 6mm in a push test at a characteristic load level (0,9Pmax).

The measured maximum forces for type 1 specimens are approximately 16% lower than the corresponding value according to EC4. The required ductility is not satisfied. The failure appeared in the concrete.

The measured maximum forces for type 2 specimens are approximately 19% lower than the corresponding value according to EC4. The required ductility is met in samples 2.1 and 2.3 by the occurrence of failure through the concrete. A shear failure of the connectors occurred in specimen 2.2.

3. TESTS ON COMPOSITE BEAMS

The experimental research is based on a full-scale testing of two test beams which, according to the static system, represent simple beams with a length of 6,00m and span of 5,75m (Fig. 5).

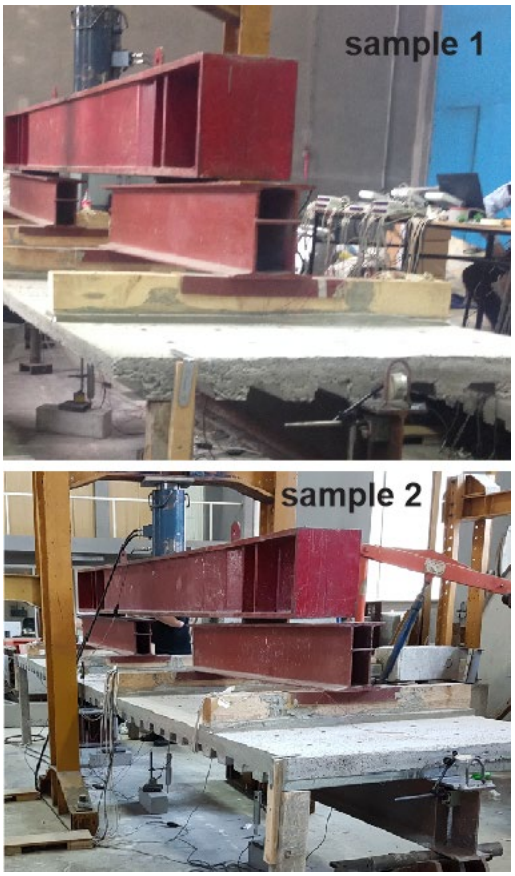

Figure 5. Test beams and load application equipment

The cross-section of the two beams is steel profile IPE240 with a reinforced concrete slab 100mm thick and 1200mm wide. In the first beam, the reinforced concrete slab is cast on the formwork of profiled steel sheet FR38/158 d=1mm placed parallel to the beam, and in the second beam the sheet is placed transversal.

The connection between the steel beam and the reinforced concrete slab is made by headed stud connectors with d=19mm, Nelson type. The studs are placed at a distance of 158mm between each rib in the transversal position. The same raster is adopted for beam 1, for comparative reasons.

The loading is applied by four concentrated forces placed at a distance of L/4 (1450mm). Two by two of the concentrated forces are applied through two secondary traverses, and the aggregate force (P=4*P1) is applied with a hydraulic jack of 1000kN through the primary traverse. The concentrated forces (P1) are applied as a linear load along the width of the reinforced concrete slab of the test beam (1200mm). For this purpose, U120...1200 profiles are welded to the secondary traverses, which rest on wooden beams 10/12cm.

The deflections were measured at 3 points at L/4 of the beam with displacement transducers; the strains were measured in the middle of the beam with strain gauges (3 on the concrete, 3 on the reinforcement, 5 on the steel section and 6 on the headed studs); the slips in the contact plane were measured in 6 points with two mechanical comparators and four inductive displacements transducers. The force is registered with a dynamometer built in the hydraulic jack.

The measurement signals are registered and processed by two data loggers, Quantum and Controls, with a measurement frequency of 2Hz, and the measured values are stored and transferred to a personal computer.

4. ANALYTICAL MODELS

3D FE models have been developed by using software ABAQUS explicit 2024. The models fully correspond with the previously described test models, both in terms of geometry and in terms of loading method. An elastic-plastic analysis with material nonlinearity was carried out [10], [12].

The FE model consists of five constituent materials: steel, concrete, reinforcement, connectors and profiled sheet. 3D solid

elements with eight nodes (C3D8R) are used to model the steel beam, connectors and concrete slab. The profiled sheet is modelled with surface (shell) elements with 4 nodes (S4R), and the reinforcement is modelled with two-node lattice elements (T3D2).

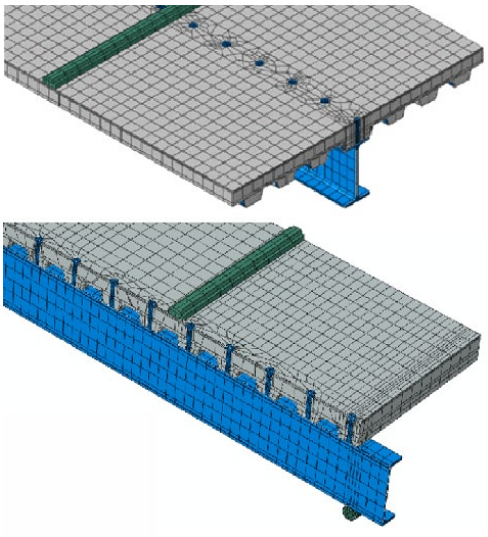

Figure 6. Finite element mesh

An elastoplastic relation σ-ε with a hardening zone for structural steel was used in the modelling of the beam steel. For the profiled sheet, considering the cold forming, an elastic ideally plastic σ-ε diagram was used.

Failure of the connectors exposed to shear and bending are very common. On the basis of this, a σ−ε relation in full range was used for the connectors, where the failure phase is also defined ($\varepsilon_u=25\varepsilon_y$, $\varepsilon_{u2}=90\varepsilon_y$).

During the loading phase, it is common part of the concrete slab to be exposed to tension, and the other part to pressure. That is why a concrete damaged plasticity (CDP) module is used. With this module, tension cracks and possible compressive crushing of concrete can be covered.

5. ANALYSIS OF THE RESULTS

Obtained results of the relation force-deflection in the middle of the beam in the Figure 7 are presented. The designation AM refers to an analytical model, and the designation EM to an experimental model.

A high degree of coincidence of the obtained results can be observed, especially for beam 2. The black line represents the relationship for assumed ideal elastic behavior through the idealized parameters of the cross section. It is evident that, even for relatively low load values, there is a deviation from the idealized line. Main reason is application of elastic shear connectors, in which relevant deformation occurs at an early stage of loadings [1], [3].

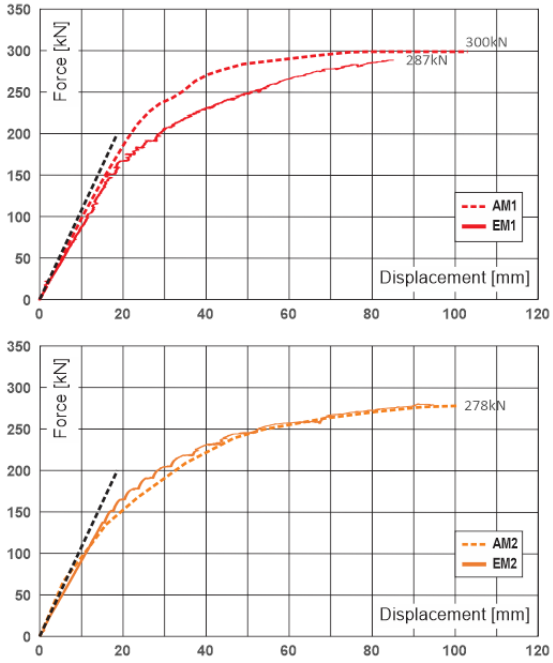

Figure 7. Relation force-maximum displacement

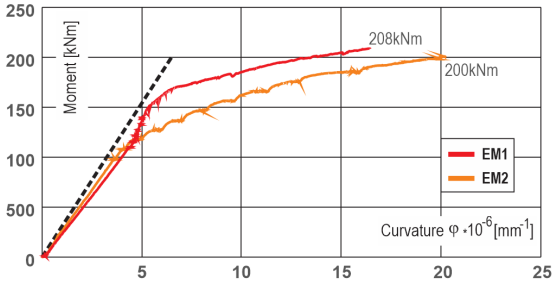

Figure 8. Experimentally determined relation M-φ

The experimentally determined relation M-φ given in Figure. 8 leads to the same conclusion. The actual stiffness of the composite beam is lower than the expected value obtained by applying elastic behavior to an idealized section.

6. CONCLUSION

Based on the conducted experimental determination of the resistance of the headed stud connectors with the standard test, it can be concluded that their resistance is lower than the recommended value in EC4. For the studs welded directly to the steel flange, in the case of longitudinal ribs of the profiled sheet, the difference is about 16%. For studs welded

through the sheet, in the case of transversal ribs of the profiled sheet, the difference is about 19%.

The resistance of headed stud connectors without a protective layer of concrete above the stud head is not specifically regulated. The test results show that there is no significant resistance decrease. Also, the decrease in resistance might be addressed to other factors.

Based on the experimental and analytical study of the composite beam with a profiled sheet with ribs placed longitudinally and transversally, it can be concluded that the stiffness of the composite beam is lower than the designed stiffness for an ideal section. This should be taken into consideration during serviceability control, both in terms of maximum deformation and in terms of dynamic behaviour (period of oscillation).

In general, composite beam with transversal position of profiled sheet ribs has a lower load-bearing capacity. In terms of stiffness, there are no significant differences related to the disposition of the profiled sheet in the zone of linear elastic behaviour.

Acknowledgements

We express our gratitude to the Construction Testing Laboratory of the Faculty of Civil Engineering at the University “St. Cyril and Methodius” in Skopje for the test equipment that was made available. Thanks also to the technical staff for their expert assistance in the preparation and examination of the samples.

REFERENCES

[1] Amanyire Barozi Victoire, John Nyiro Mwero, Naftary Gathimba, Experimental study on the effect of partial shear studs layout on flexural behavior of steel-concrete composite beams. Results in Engineering Volume 21, March 2024.

[2] Cvetanovski P., Popovski D., Partikov M., Dmjanovski V., “Experimental investigation of load and slip capacity of headed stud connectors in composite slabs for buildings”, Annual of the university of architecture, civil engineering and geodesy, Sofia, Volume 46, 2018.

[3] Couchman, G., Minimum Degree of Share Connection Rules for UK Construction to Eurocode 4, SCI P405, 2015.

[4] European Standard EN 1994, Eurocode 4: Design of composite steel and concrete structures, Part 1-1: General rules and rules for buildings, 12.2004, +AC 04.2009, European Committee for Standardization.

[5] European Standard EN 1994, Eurocode 4: Design of composite steel and concrete structures, Part 1-1: General rules and rules for buildings, Draft prEN 1944 1-1 March 2024, European Committee for Standardization.

[6] Faella, C., Martinelli, E. & Nigro, E., Steel and concrete composite beams with flexible shear connection: "exact" analytical expression of the stiffness matrix and applications. Computers and Structures 80 (2002) 11, pp.1001-1009.

[7] Hicks, S.J.: Strength and ductility of headed stud connectors welded in modern profiled steel sheeting, The Structural Engineer, 85, No. 10, 2007, pp 32-38.

[8] Horita Y., Tagawa Y., Asada H., Push-out test of headed stud in composite girder using steel deck -An effect of stud length of projecting part from steel deck on shear strength, 15 WCEE, Lisboa 2012.

[9] Konrad, M., Kuhlmann, U., Headed Studs Used in Trapezoidal Steel Sheeting According to Eurocode 4, SEI, Volume 19, Nr.4, 2009.

[10] Lam D., El-Lobody E., Bahaviour of headed stud shear connections in composite beam. Journal of Structural Engineering, 2005.

[11] Qureshi J., Lam D., Ye J., Behavior of headed shear studs in a push test using profiled steel sheeting, Research gate, July 2009.

[12] Spacone Enrico, Nonlinear Analysis of Steel-Concrete Composite Structures: State of the Art, A.M.ASCE, Jurnal of Structural Engineering, Vol. 130, No. 2, February 2004.

[13] Stephen J. Hicks, Andrew L. Smith, Stud Shear Connectors in Composite Beams that Support Slabs with Profiled Steel Sheeting, Structural Engineering International, 2014.

SEISMIC RETROFIT OF MASONRY WALLS USING REPOINTING

Festim Ademi
MSc in Civil Engineering
Ss. Cyril and Methodius University in Skopje
Faculty of Civil Engineering
N. Macedonia
festim.ademi@hotmail.com

Sergey Churilov
PhD, Professor
Ss. Cyril and Methodius University in Skopje
Faculty of Civil Engineering
N. Macedonia

Elena Dumova Jovanoska
PhD, Professor
Ss. Cyril and Methodius University in Skopje
Faculty of Civil Engineering
N. Macedonia

DOI: https://www.doi.org/10.55302/SJCE2421359a

Seismic strengthening of masonry structures through repointing has been recognized as an efficient and low-cost technique for increasing structural stability, particularly in regions of high seismic activity. This paper shows the results from the research program that involved laboratory tests of the mechanical properties of masonry. The objective of the research was to evaluate the effectiveness of repointing as a method of strengthening existing structures, providing greater resistance to compression and dynamic loads.

The results show that repointing, particularly when advanced materials are used, considerably increases the compressive strength of masonry structures as well as their ability to sustain seismic forces. Additionally, the method contributes to the improvement of their long-term stability, which makes it applicable to a wide spectrum of structures. The economic analysis of the application of repointing shows that this approach is not only effective but also financially viable which makes it a practical choice in civil engineering, being able to provide a considerable contribution to the seismic safety of structures.

Keywords: seismic strengthening, masonry structures, polypropylene strips, repointing.

1. INTRODUCTION

Unreinforced masonry buildings were of interest to be built centuries ago. Most of these buildings that still exist in our country were built at the beginning of the twentieth century. These types of buildings include individual houses, religious buildings, residential buildings, but also larger buildings that house public institutions (hospitals, schools, sports halls, museums, etc.).

Masonry has withstood the test of time as a durable and reliable construction technique, but with the evolving challenges posed by seismic activity and aging infrastructure, it is imperative that we develop effective retrofitting methods to improve the resilience of these structures.

In contemporary practice, scientists and engineers are actively exploring the potential of repointing as a seismic retrofitting technique for

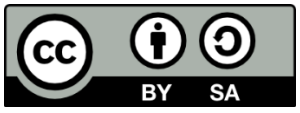

existing structures. Research indicates that proper repointing with advanced materials, such as fiber-reinforced polymer (FRP) systems, can enhance the capacity of walls to withstand dynamic forces induced by earthquakes. Both laboratory and field investigations have demonstrated this method's efficacy as a critical component in seismic strengthening strategies, enabling improved risk assessment and mitigation of catastrophic damage [1].

2. EXPERIMENTAL PROGRAMME FOR TESTING THE EFFECTS OF REPOINTING

To define the effects of repointing on behavior of bearing walls, it was proposed to carry out an experimental program involving laboratory testing of the bearing capacity of masonry in which repointing was applied in the following three different ways:

- Strengthened masonry repointed with lime mortar and with horizontally placed polypropylene strips (Figure 1 and Figure 3).
- Strengthened masonry repointed with lime mortar and with diagonally placed polypropylene strips Figure 2 and Figure 4).
- Strengthened masonry repointed with repair mortar FS4 and with horizontally placed polypropylene strips.

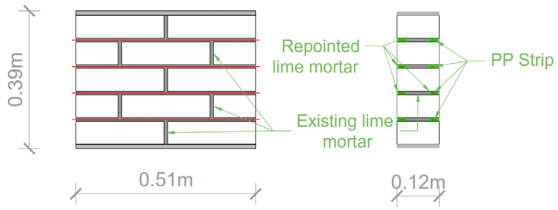

Figure 1. Horizontal application of PP strip and repointing.

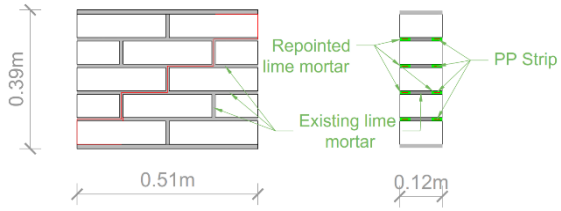

Figure 2. Diagonal application of PP strip and repointing

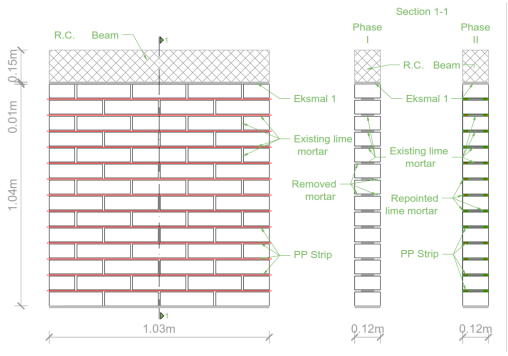

Figure 3. Horizontal application of PP strip and repointing.

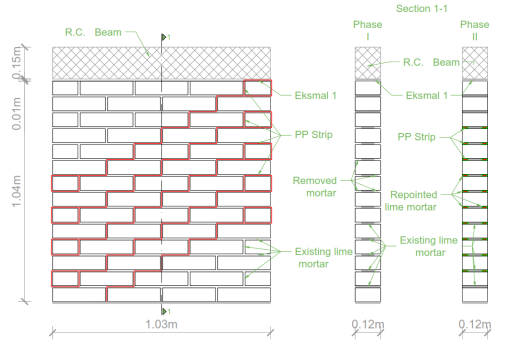

Figure 4. Diagonal application of PP strip and repointing.

Taking into account that masonry is a composite material, the experimental program consisted of three parts: testing of the mechanical characteristics of the constituent materials, bricks and mortar, testing of the compressive strength and testing of the shear strength of masonry. To quantify the proposed repointing procedures, the results from testing of unreinforced masonry were used as referent values. Further in the text, a brief description of the performed tests, the obtained results and the corresponding conclusions is given.

2.1 TESTS ON CONSTITUENT MATERIALS

Tests on constituent materials represent a key step in assessing their durability and suitability for use in engineering structures. The mechanical and physical properties of the materials are defined through different tests, enabling analysis of their behavior under different loads [2]. The presented research involved tests on solid clayey bricks, mortars and polypropylene strips for the purpose of obtaining data on their strength, density, water absorption and other characteristics that are important for optimization of structural systems and improvement of safety of structures. Table 1 shows the obtained mechanical characteristics of the constituent materials.

Table 1. Mechanical characteristics of constituent materials.

Material	Density γ_d	Compres. strength $f_{m,comp}$	Flexural tensile strength $f_{m,flex}$
	(kg/m^3)	(MPa)	(MPa)
Clay brick	1750.50	9.54	2.05
Lime mortar		0.73	0.42
Repair mortar		50.40	11.97

2.2 TESTS ON MASONRY AS CONSTITUENT MATERIAL

For the needs of the investigation, two special setups were developed. They were designed to test the compressive strength and the shear strength of masonry. These setups enabled a precise and controlled analysis of different types of walls, including unreinforced and strengthened structures for the purpose of defining their mechanical properties and behavior under different loads. This provided the basis for comparison of the results and optimization of the strengthening methods in engineering practice [3].

2.2.1 Setup for Testing Compressive Strength of Masonry

Testing of compressive strength was carried out by a special setup consisting of two metal columns (steel columns) fixed to a reinforced concrete floor by steel anchors, connected to an upper steel beam (steel beam “I 160”) that served to provide stability and support to the hydraulic actuator. The testing wall was placed between the columns of the steel beam (“I 300”) through a rubber layer with a thickness of 10 mm for better contact. Placed on the top of the wall was an additional rubber layer and a steel beam (“I 160”) for transfer of the force to the load cell connected to the hydraulic actuator. This setup enabled precise measurements of compressive strength under strictly controlled laboratory conditions.

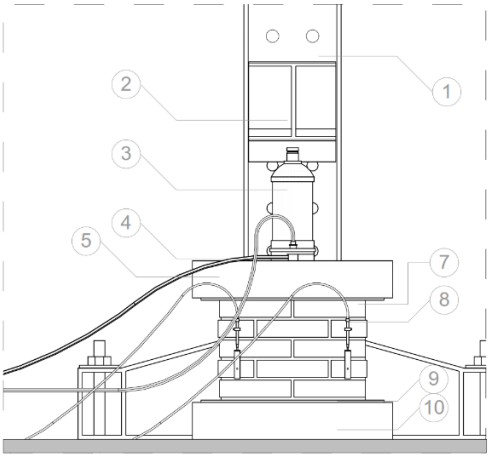

Figure 5. Setup for testing the compressive strength of masonry.

2.2.2 Setup for Testing Shear Strength of Masonry

The setup for testing of shear strength consisted of four metal columns fixed to the reinforced-concrete floor, connected with steel beams. The walls were placed upon a steel beam (“I 200”) and were stabilized with a reinforced concrete beam, whereas rubber layers with a thickness of 10 mm were used for better contact between the materials. Horizontal force was generated by the hydraulic actuator that transferred the force to the walls through roller bearings. A deflection meter (strain gauge) was placed for precise measurement of strains caused by horizontal loads.

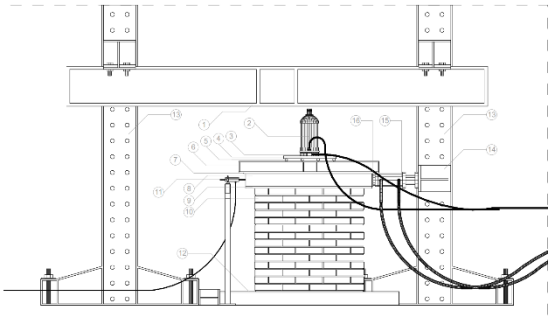

Figure 6. Setup for testing of shear strength of masonry.

These two setups enabled precise and controlled assessment of the performances of different types of walls, including unreinforced and strengthened structures. The results obtained provided important data on the mechanical properties of masonry to be applied in the design and optimization of engineering structures.

2.3 TESTS FOR DEFINITION OF COMPRESSIVE STRENGTH OF MASONRY

Within the frames of the investigation of the mechanical properties of masonry, several wall specimens were tested to define their compressive strength. The specimens were composed of 10 clayey bricks and mortar (lime mortar and repair mortar) that functioned as a composite material. The proportions of the bricks were 250 x 120 x 60 mm, whereas those of the walls were 510 x 390 x 120 mm. Tested were eight walls, distributed into four categories with two specimens each: unreinforced walls, walls strengthened with lime mortar and PP strip in horizontal joints, walls strengthened diagonally with a PP strip and walls strengthened with repair mortar FS 4 and PP strip in horizontal joints.

Figure 7. Testing the compressive strength of masonry.

Figure 8. Compressive strength - a wall after testing (under the effect of compressive force).

2.4 TESTS FOR DEFINITION OF SHEAR STRENGTH OF MASONRY

Within the frames of the investigation of the mechanical properties of masonry, in addition to the tests of compressive strength, tests of shear strength were also carried out. Each wall was composed of 56 clayey bricks and mortar (lime mortar or repair mortar) as a composite material. The proportions of the bricks were 250 x 120 x 60 mm, while those of the test specimens were 1030 x 1040 x 120 mm. Tested were a total of eight walls divided into four categories, with two specimens each: unreinforced walls, walls strengthened with lime mortar and PP strip in horizontal joints, walls strengthened diagonally with PP strip and walls strengthened with repair mortar FS4 and PP strip in horizontal joints.

Figure 9. Testing of shear strength of masonry.

Figure 10. Shear strength - wall after testing.

3. RESULTS FROM TESTS

The results from the performed tests of compressive and shear strength of masonry structures provided a detailed insight into the mechanical properties of different types of walls. Through graphic analysis, the force - deformation relationships and the response of the walls to different types of loads are presented. These results are of primer importance for the assessment of the effectiveness of the applied strengthening techniques and their ability to provide structural stability under static and dynamic forces for

improvement of safety and durability of structures [4].

3.1. COMPRESSIVE STRENGTH OF MASONRY

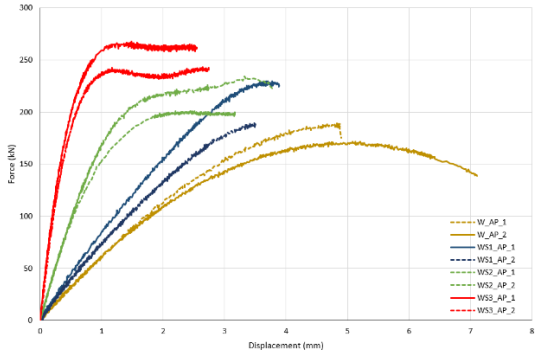

Figure 11. Force-deformation diagram for testing compressive strength of walls.

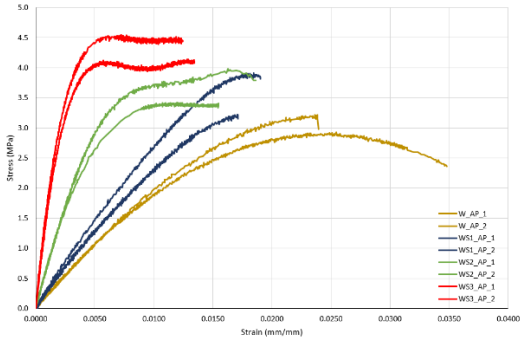

Figure 12. Stress-deformation diagram for testing compressive strength of walls.

The tests showed important improvements in the strength of masonry structures by the application of different strengthening techniques [5]. WS1_AP: Strengthening with lime mortar and PP strip in horizontal joints resulted in an increase of maximum strength of 16.1% and final strength of 31.9%, with a decrease of deformation of 27.6% and 38.5%. WS2_AP: The diagonal position of the PP strip led to an increase of maximum strength of 20.6% and final strength of 34.1%, with a decrease of deformations of 42.5% and 41.9%. WS3_AP: Strengthening with repair mortar and PP strip in horizontal joints showed the highest level of improvement, with an increase of maximum strength of 41.5% and final strength of 60.1%, whereas deformations were reduced for 58.9% and 55.9% The data are presented in tabular form in Table 2.

Table 2. Values obtained for compressive strength of walls.

Types of Examined Walls (Names)	Peak compressive stress, $f_{mas,test}$	Peak stress inc-rease (%)	Ultimate compressive stress, $f_{mas,ult}$	Ultimate stress inc-rease (%)
W_AP	3.07	0.0%	2.67	0.0%
WS1_AP	3.56	16.1%	3.52	31.9%
WS2_AP	3.70	20.6%	3.58	34.1%
WS3_AP	4.34	41.5%	4.27	60.1%

Types of Examined Walls (Names)	Peak strain, ε_{max}	Peak strain decrease (%)	Ultimate strain, ε_{ult}	Ultimate strain dec-rease (%)
W_AP	0.0246	0.0%	0.0294	0.0%
WS1_AP	0.0178	-27.6%	0.0181	-38.5%
WS2_AP	0.0141	-42.5%	0.0171	-41.9%
WS3_AP	0.0101	-58.9%	0.0130	-55.9%

3.2. SHEAR STRENGTH OF MASONRY

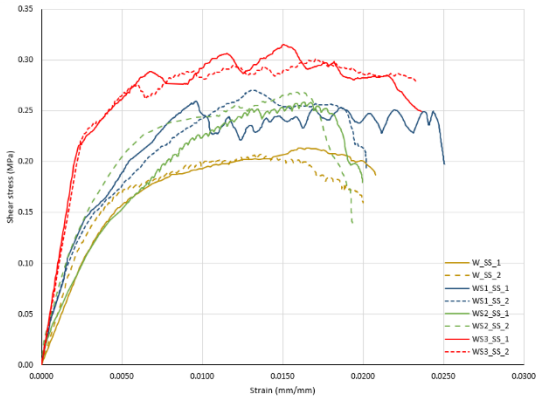

Figure 13. Shear stress - deformation diagram for different types of walls.

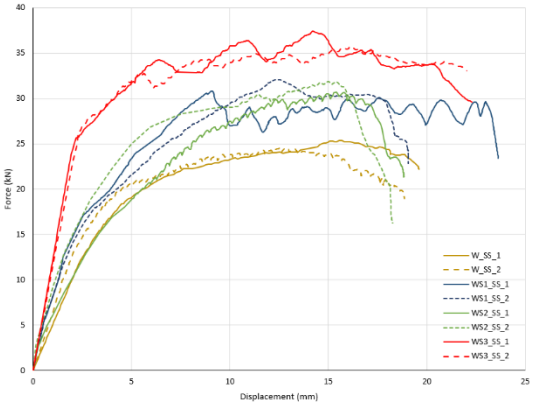

Figure 14. Force - displacement diagram for unreinforced walls and walls strengthened with different methodologies.

W_SS_1 and W_SS_2 unreinforced walls served as the basic line for comparison. They showed the lowest shear strength and the greatest deformation under loads. WS1_SS_1 and WS1_SS_2 were strengthened with lime mortar and a horizontally placed PP strip, which resulted in an increase of shear strength of about 25.9% and a decrease of deformation of 24.5% compared to unreinforced walls. WS2_SS_1 and WS2_SS_2 with a diagonally placed PP strip and lime mortar showed an increase of shear strength of 25.3% and a decrease of deformation of 6.3% compared to the basic specimens. WS3_SS_1 and WS3_SS_2, strengthened with repair mortar FS4 and horizontally placed PP strips showed the best results, with an increase of shear strength of 46.6% and a decrease of deformation of 6.1%.

Table 3: Values of maximum strength and deformation at shear for different types of walls.

Types of Examined Walls (Names)	Peak shear stress, $f_{mas,test}$	Peak shear stress increase (%)	Peak shear strain, ε_{max}	Peak shear strain decrease (%)
W_SS	0.210	0.0%	0.0151	0.0%
WS1_SS	0.265	25.9%	0.0114	-24.5%
WS2_SS	0.263	25.3%	0.0161	6.3%
WS3_SS	0.308	46.6%	0.0161	6.1%

4. CONCLUSION

The experimental investigations confirmed that the application of different techniques for strengthening with repointing considerably improved the mechanical characteristics of masonry, particularly from the aspect of its compressive and shear strength. The results showed that unreinforced walls were characterized by the weakest mechanical properties, with limited bearing capacity and considerable susceptibility to deformations under loads.

These walls were identified as a referent point for the assessment of the effectiveness of different strengthening techniques.

As to the compressive strength, strengthening with lime mortar and horizontally placed PP strips led to an increase of maximum strength of 16.1% and an increase of final strength of 31.9%, with a considerable decrease of deformations. Diagonal placement of PP strips showed additional improvement, but the greatest progress was achieved by use of repair mortar and horizontal PP strips, resulting in an increase of maximum strength of 41.5% and an increase of final strength of 60.1%, whereat the deformations were considerably decreased.

Regarding the shear strength, unreinforced walls again showed the lowest bearing capacity and the highest susceptibility to deformations. Strengthening with horizontal PP strips resulted in an increase of strength of 25.9%, whereas diagonal placement of PP strips added an increase of 25.3%. The greatest improvements were achieved with repair mortar and horizontally placed PP strips, whereat shear strength was increased for 46.6%, while deformations were reduced for 6.1%.

These results pointed out that proper choice and application of strengthening techniques could considerably increase bearing capacity, stability and resistance of masonry structures, particularly in seismically active regions. The use of repair mortar in combination with horizontally placed PP strips was shown as the most optimal solution, providing maximum bearing capacity, minimal deformations and increased safety of structures. This methodology represents an important contribution to engineering practice, with direct application in design and advancement of engineering structures in zones of high seismic risk.

REFERENCES

[1] Sergey Churilov – ''Experimental and Analytical Research of Strengthened Masonry'' – Doctoral dissertation

[2] Sergey Churilov, Elena Dumova-Jovanoska, ''In-plane Shear Behaviour of Unreinforced and Jacketed Brick Masonry Walls'', Elsevier Ltd, 2013.

[3] Bojan Damchevski, Sergey Churilov, Elena Dumova-Jovanoska, ''Mechanical Characterization of Polymer Fibre-reinforced Cement-based Mortar for Masonry Joint Repointing'', Thessaloniki, 2018.

[4] MEASURES OF REHABILITATION OF UNREINFORCED MASONRY SPORTS FACILITY WITH IRREGULARITIES. - Festim Ademi, Enis Jakupi, Rezona Fetahu , Journal of Applied Sciences-SUT (JAS-SUT), Volume 9.

[5] Calderini, C., Cattari, S., & Lagomarsino, S. (2009). In-plane Strength of Unreinforced Masonry Piers. Earthquake Engineering and Structural Dynamics, 38(2), 243–67.

Jasemin Hodza Djafer
International Vision University, Gostivar
N. Macedonia
yasemin.hoca@vision.edu.mk

Sergey Churilov
PhD, Professor
Ss. Cyril and Methodius University in Skopje
Faculty of Civil Engineering
N. Macedonia

METHODOLOGY FOR ASSESSING THE VULNERABILITY OF EXISTING MASONRY BUILDINGS: CASE STUDY OF GOSTIVAR CITY

DOI: https://www.doi.org/10.55302/SJCE2421365dj

Seismic vulnerability assessment of masonry structures is a very important issue even for regions with moderate to low seismic hazard. This is even more important when dealing with old buildings, such as the buildings located in the geographical area of interest, where all masonry structures were built in nineteenth century and in the first half of the twentieth century, that is, before the adoption of the aseismic design regulation. Although most of the masonry building stock in the researched region consists of residential buildings, there are also public and religious buildings. As a result of the field studies, it was determined that many people lived in these buildings. The uncertain behavior of masonry structures during earthquakes shows that people living in these residences are at risk. In this context, the aim of the research is to examine the building stock of masonry structures to evaluate the seismic risk in the region. There are different methods for assessing the vulnerability of structures. The purpose of the research, scope of the study, available resources, etc. should be considered when choosing the appropriate methodology. This paper presents a methodology for assessing the seismic vulnerability of existing masonry structures and the results obtained from the application of the methodology for the city of Gostivar.

Keywords: masonry structures, seismic risk, vulnerability assessment, vulnerability index, urban areas

1. INTRODUCTION

The high sensitivity of today's technologies, large cities built in seismic hazard zones are some of the reasons for the increase in losses from natural disasters in recent years [1]. All this has increased interest in the development of seismic assessment methodologies as well as solutions for reinforcing existing building stocks [2].

It is necessary to construct buildings in accordance with the seismic design rules to

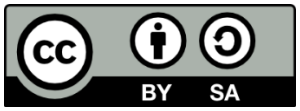

ensure seismic safety. However, existing buildings do not meet these rules, which has led to the need to estimate the vulnerability of existing buildings [3].

The assessment of the vulnerability of buildings can be defined as their susceptibility to damage at a certain earthquake intensity. In the past, many methods have been proposed to assess seismic vulnerability [4].

These methods are used from single buildings to large urban areas. To select the right method, the purpose of the research, the available resources, the approach to obtaining information, the economic situation and the computational effort should be taken into consideration [5].

1.1 METHODS FOR VULNERABILITY ASSESSMENT

To determine the seismic vulnerability of a building, there is a need to establish a correlation that can provide the expected damage level for each seismic intensity level and define appropriate parameters to measure damage and severity [6].

Different vulnerability assessment methods have been proposed and applied in the past. They can be classified generally into two groups: empirical and analytical, both groups can be used in hybrid methods [7].

2. METHODOLOGY FOR SEISMIC VULNERABILITY ASSESSMENT OF MASONRY BUILDINGS

The seismic vulnerability assessment of many buildings in an urban environment is a difficult and complicated task because it is not rational to perform nonlinear analysis of all buildings. To solve this, vulnerability curves obtained by numerical analysis and statistical processing of the results for a class of buildings can be defined. Vulnerability curves relate to the probability of exceeding a certain damage level for a given earthquake intensity [8] [9] [10].

Various studies have been conducted using vulnerability curves to assess seismic vulnerability and damage scenarios of buildings in urban centers and to determine basic critical situations. Empirical methods such as the vulnerability class method and the vulnerability index method are widely used methods to define the vulnerability of buildings in urban areas. In this research, the Vulnerability Index (VIM) method was used to assess the vulnerability of the selected buildings in Gostivar. The vulnerability index method (VIM) is based on the statistical relationship between macroseismic intensity and apparent or observed damage observed in previous earthquakes, as well as the fact that different structural classes tend to experience the same or similar types of damage. The vulnerability index method was originally developed by Benedetti and Petrini [11] [12].

This method, called an indirect method since the relationship between seismic action and response is established through the sensitivity index, is based on a large amount of data obtained from the detected damages. According to this classification, the vulnerability index of each building is evaluated using the following formula:

$$I_{vf}^{*} = \sum_{i=1}^{11} C_{vi} \cdot P_{vi} \quad (1)$$

The vulnerability index (I_{vf}^{*}) is calculated as a scaled sum of 14 parameters where each parameter is defined by a weighting factor P_{vi}, and each parameter is associated with four classes (C_{vi} – A, B, C, D) from (A – optimal) to (D – unfavorable). Later, Vicente made additions and added 3 more parameters to the existing 11 parameters [5]. Ferreira also made additions and calibrated according to the data from the 1998 Azores earthquake [13]. After these calibrations, the method was used to assess the seismic vulnerability of different historical city centers. With the changes made, the final formula is as follows:

$$I_{vf}^{*} = \sum_{i=1}^{14} C_{vi} \cdot P_{vi} \quad (2)$$

The methodology used in this study is based on the calculation of a vulnerability index for each building. The vulnerability index is calculated as the sum of the determined values of the seismic responses of 14 parameters for each building (Table1).

Table 1. Parameters for calculating vulnerability index [5] [13]

Parameters	Class (C_{vi}) A B C D	Weight Factor P_{vi}	
		Vicente, 2008	Ferreira, 2017
Group 1. Structural building system			
P1.Type of resisting system	0 5 20 50	0.75	2.50

P2.Quality of resisting system	0 5 20 50	1.00	2.50
P3.Conventional strength	0 5 20 50	1.50	1.00
P4.Maximum distance between walls	0 5 20 50	0.50	0.50
P5.Number of floors	0 5 20 50	1.50	0.50
P6.Location and soil conditions	0 5 20 50	0.75	0.50
Group 2. Irregularities and interaction			
P7. Aggregate position and interaction	0 5 20 50	1.50	1.50
P8. Plan configuration	0 5 20 50	0.75	0.50
P9. Irregularity in elevation	0 5 20 50	0.75	0.50
P10. Wall façade openings and alignments	0 5 20 50	0.50	0.50
Group 3. Floor slabs and roofs			
P11.Horizontal diaphragms	0 5 20 50	0.75	0.75
P12. Roofing system	0 5 20 50	2.00	0.50
Group 4. Conservation state and other elements			
P13. Conservation state	0 5 20 50	1.00	1.00
P14. Non-structural elements	0 5 20 50	0.75	0.75

For each parameter, a weighting factor P_{vi}, with a value between 0.5 and 2.5, is determined according to its contribution to the examined building. The weighting factors P_{vi}, are evaluated in four vulnerability classes C_{vi} (A, B, C, D) where (A – optimal) to (D – unfavorable).

2.1 VERIFICATION FOR THE PROPOSED METHODOLOGY

The vulnerability index method is like the GNDT II (National Group for Earthquake Defense) proposal. GNDT II is developed with this method, but it allows correlation between data because important parameters are similar [14]. This equivalence allows the validation of the proposed methodology and its correlation with the macroseismic methodology of Giovinazzi and Lagomarsino [15] and allows the construction of damage and loss scenarios.

The methodology developed by Benedetti and Petrini (1984) uses the vulnerability index as an intermediate step in the damage assessment process for buildings subjected to a certain level of seismic action. This deterministic correlation between seismic action (expressed in terms of PGA) and damage (expressed as a vulnerability index ranging from 0 to 1) represents the quotient between the costs of repairing and replacing the original undamaged condition, referring to the present value of the structure. When using the vulnerability curves of the macroseismic methodology proposed by Giovinazzi and Lagomarsino [15], it is essential that they correspond to the GNDT II methodology [14], due to its similarity with the proposed methodology. The macroseismic methodology is based on the definition of building typologies belonging to vulnerability classes, damage classifications and intensity levels according to the European Macroseismic Scale EMS-98 defined by Grünthal [16].

In the macroseismic methodology, vulnerability is also expressed by a numerical value, the vulnerability index (V), which varies from 0 to 1, initially defined according to typological information (type of construction), which is then adjusted with scores attributed to the modified parameters. These parameters depend on the unique characteristics of buildings [17], such as: building condition, quality of materials and construction, number of floors, irregularities, etc. From this value of the vulnerability index (V), a vulnerability function is constructed, translated into an analytical expression of the building or typology of buildings for different EMS-98 macroseismic intensities [16]. In this way, expression (3) is obtained, which allows the calculation of the average damage level (μ_D), defined in the range from 0 to 5.

$$\mu_D = 2.5\left[1 + \tanh\left(\frac{I+6.25-13.1}{Q}\right)\right], \quad 0 \le \mu_D \le 5 \tag{3}$$

The value of the intermediate damage level $\mu_D =$ depends on the fragility index (V), macroseismic intensity (I) and ductility factor (Q), which can vary from 1 to 4. According to the latest calibrations, it has been determined that the most suitable value for masonry buildings is the ductility factor Q = 2.0 [18].

The damage assessment according to the Petrini and Benedetti methodology [11] is expressed as an index of the mean damage value, table 2. This damage index is correlated with the mean damage level (μ_D), given by the macroseismic methodology, which represents the average value of the damage degree (p_k) and is used for the discretized damage degree (D_k), (Table 2), expressed as:

$$\mu_D = \sum_{k=0}^{5} p_k \cdot D_k \tag{4}$$

Table 2. Division of damage by factor and average level of damage

Discretized degree of damage	Damage factor DF	Medium level of damage μ_D
D0- No damage	0.00	[0.00 – 0.50]
D1- Slight damage	0.01	[0.50 – 1.42]
D2- Moderate damage	0.10	[1.42 – 2.50]
D3 – Major damage	0.35	[2.50 – 3.50]
D4 – Very major damage	0.75	[3.50 – 4.00]
D5 - Destroyed	1.00	[4.00 – 5.00]

For ease of application, the relationship between the average damage index value (DF) and the average damage value (μ_D) is converted into an analytical expression given by equation (5), and the correlation of the two procedures is shown in table 3.

$$\mu_D = 4 \cdot DF^{0.45} \tag{5}$$

Table 3. Correlation between vulnerability index of two procedures [19]

GNDT II Methodology	I_v = 45	I_v = 20	I_v = -5
Macroseismic methodology	Class A (V = 0.88)	Class B (V= 0.72)	Class C (V= 0.56)

Based on this comparison, it is possible to define an analytical linear correlation between the vulnerability indexes of the two methodologies (V and I_v):

$$V = 0.592 + 0.0057 \cdot I_v \tag{6}$$

3. APPLICATION OF SEISMIC VULNERABILITY ASSESSMENT METHODOLOGY IN GOSTIVAR

According to the proposed methodology of Vicente, a data collection form for field research is proposed. The parameters of the vulnerability index methodology are adapted to the research area. The aim is to collect more accurate information needed for the assessment of the seismic vulnerability of buildings more quickly. Figures 1 and 2 show the proposed data collection form, while Figure 3 shows an example of completed forms from field research.

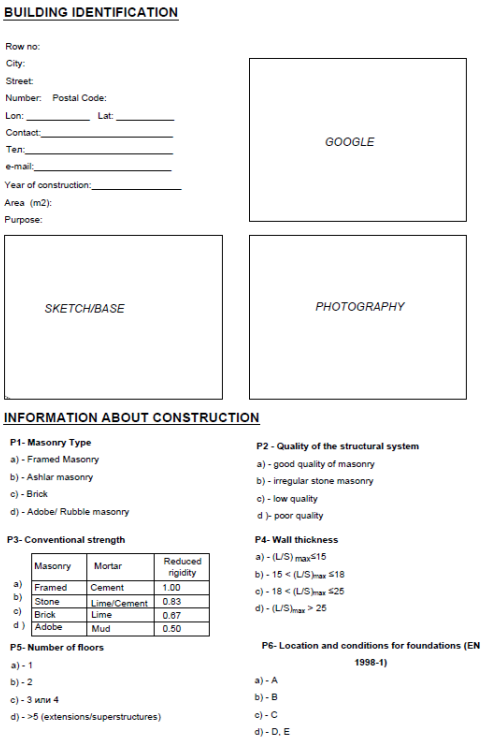

Figure 1. Form - Page 1 (by author)

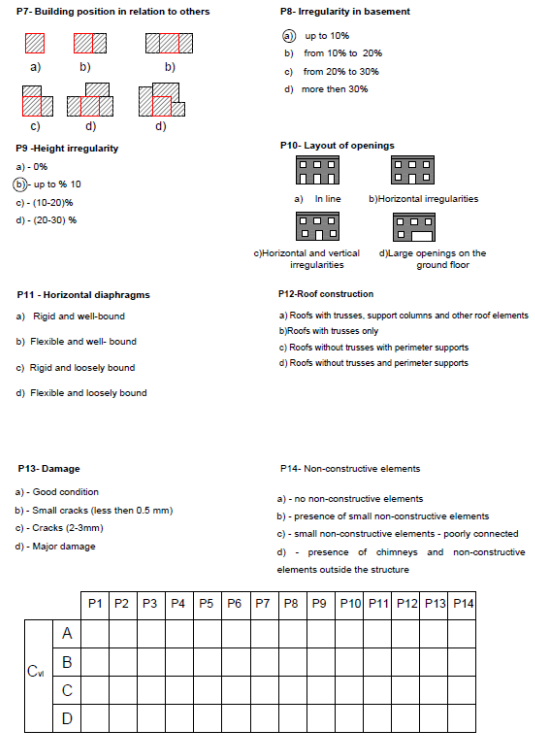

Figure 2. Form - Page 2 (by author)

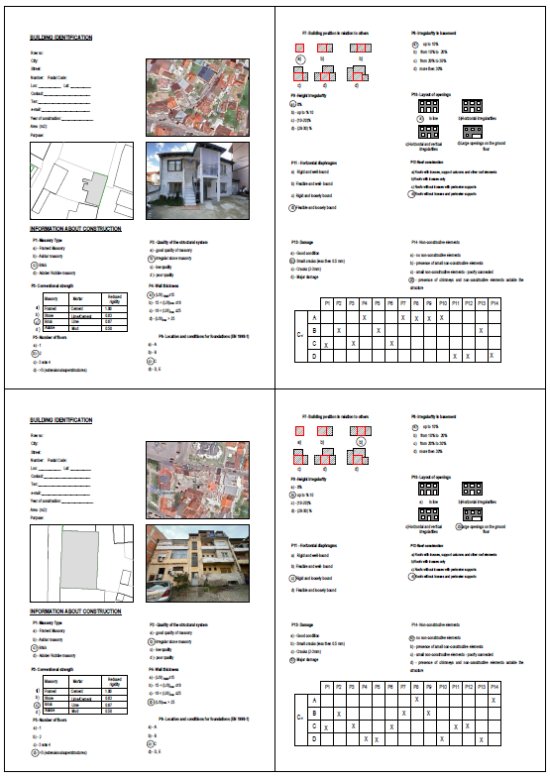

Figure 3. Examples of completed forms in field research (by author)

The seismic vulnerability assessment is made by calculating the vulnerability index I_{vf}^*, which is calculated with equation (2). The vulnerability index I_{vf}^* is normalized from 0 to 100. The weighting factors (p_{vi}) provided by Ferreira were used in the calculation of the vulnerability index. 143 buildings were evaluated in the central urban area of the city of Gostivar. Figure 4 presents the percentage repesresentation of buildings according to I_{vf}.

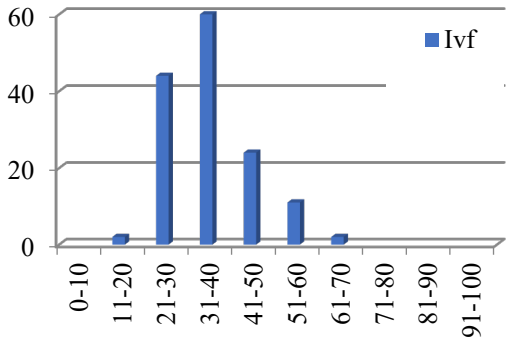

Figure 4. Percentage representation of buildings in Gostivar according I_{vf} - (by author)

From the obtained values, it can be noted that most masonry buildings in Gostivar have a vulnerability index between 21 and 40. According to Ferreira's weighting factors, 1.3% of the buildings belong to the interval between 11 and 20, 30.7% to the interval 21-30, 41.9% to the interval 31-40, 16.7% to the interval 41-50, 7.6% to the interval 51-60 and 1.3% of the buildings to the interval 61-70. Figure 5 shows the spatial distribution of I_{vf} for the current state of the buildings in Gostivar.

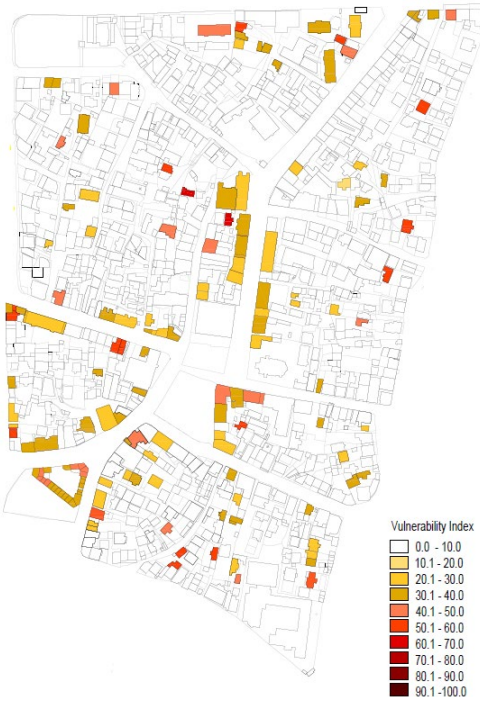

Figure 5. Spatial distribution of I_{vf} for the current state of the buildings in Gostivar - (by author)

Based on the calculated values of the vulnerability index, using equation (3), the average damage level (μ_D) was calculated for different scenarios of macroseismic intensities. The study calculated 4 different scenarios of macroseismic intensities between VI and IX degrees according to the MCS scale. Figure 6 shows the statistical data for the percentage representation of the obtained average damage level for each of the four individual scenarios.

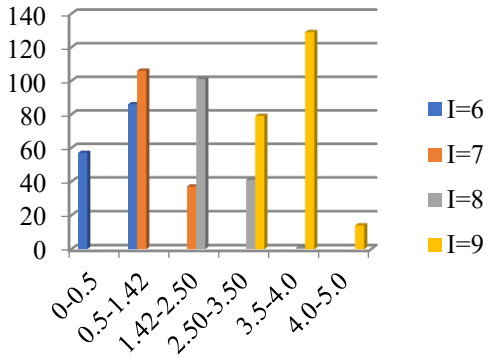

Figure 6. Percentage of buildings according to the average level of damage (μ_D)

According to the analysis of the results, it is noted that for lower earthquake intensities (VI and VII degrees), the buildings in Gostivar are evaluated with scores from 0 to 2.5. For higher earthquake intensities (VII and IX degrees), the buildings receive scores from 2.5 to 5.

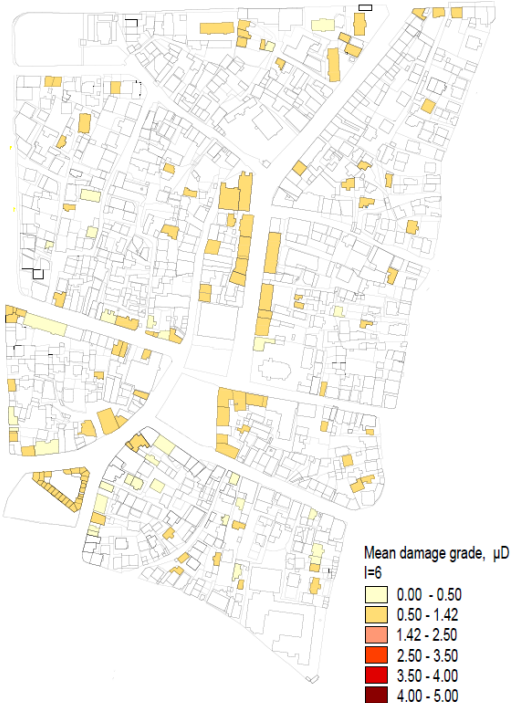

Figure 7. The spatial distribution of the average level of damage for I=6, for buildings in Gostivar

Figure 8. The spatial distribution of the average level of damage for I=7, for buildings in Gostivar

A graphical representation of the spatial distribution of the mean level of damage for earthquake intensities from I=6 to I=9 for Gostivar is shown in Figure 7,8,9 and 10.

Figure 9. The spatial distribution of the average level of damage for I=8, for buildings in Gostivar

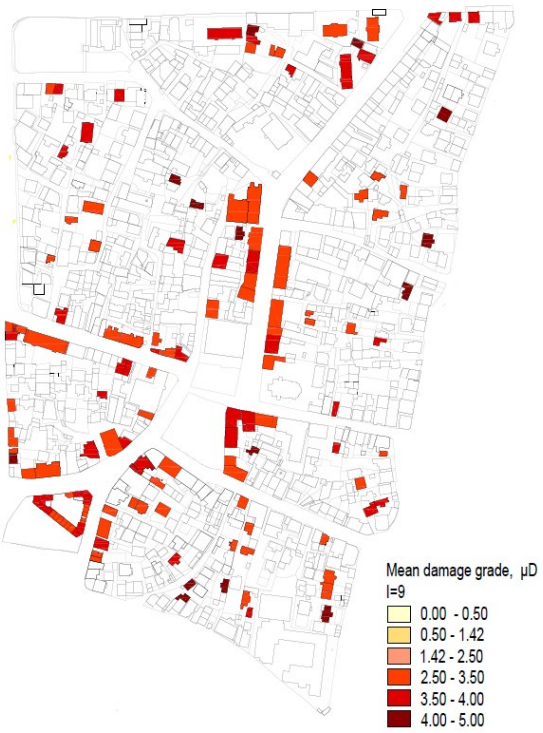

Figure 10. The spatial distribution of the average level of damage for I=9, for buildings in Gostivar

According to the seismic vulnerability obtained of the buildings, vulnerability curves of the masonry buildings in Gostivar were constructed depending on different macroseismic intensities (Figure 11).

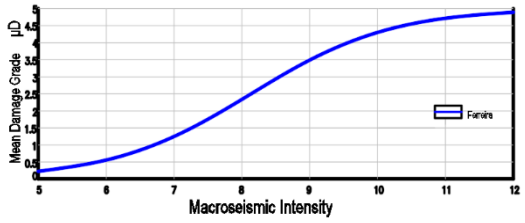

Figure 11. Vulnerability curves for the existing condition of the buildings in Gostivar

4. CONCLUSION

The aim of the study is to analyze a larger number of buildings to examine the vulnerability of existing masonry structures in urban areas. From the obtained results, a typological classification of existing masonry structures can be used to assess seismic risk at a regional level. For this purpose, the vulnerability index methodology was chosen as a methodology for assessing existing masonry structures. From the results obtained presented in the paper, most of the buildings analyzed in Gostivar would experience very large damage or even collapse at the highest earthquake intensity. From the results obtained, buildings or areas that are at the highest risk can be identified and measures can be taken to strengthen them. A precise assessment of the vulnerability of existing buildings and the implementation of appropriate strengthening solutions can significantly reduce physical damage and economic losses from future seismic events.

REFERENCES

[1] Smolka, A., Allmann, A., Hollnack, D. and Thrainsson, H. (2004). “The Principle of Risk Partnershipand the Role of Insurance in Risk Mitigation”, Proceedings of the 13th World Conference on Earthquake Engineering, Vancouver, Canada.

[2] Giovinazzi, S., Lagomarsino, S., Pampanin, P. (2006). “Vulnerability Methods and Damage Scenario for Seismic Risk Analysis as Support to Retrofit Strategies: an European Perspective”.

[3] Sarraz, A., Kroshed, A. Md. (2015). “Seismic Vulnerability Assessment of Existing Building Stocks at Chandgaon in Chittagong City, Bangladesh”, Americen Journal of Civil Engineering.

[4] Lumantarna, E, Lam, N., Tsang, H., Wilson, J., Gad, E., and Goldsworthy, H. (2014). "Review of Methodologies for Seismic Vulnerability Assessment of Buildings."

[5] Vicente, R., Parodi, S., Lagomarsino, S., Varum, H., Mendes Silva, J. A.R. (2011). “ Seismic vulnerability and risk assessment: case study of the historic city sentre of Coimbra, Portugal“, ull Earthquake Eng, 9:1067-1096 DOI 10.1007/s10518-010-9233-3

[6] DMTP. (1994). “Disaster Management Training Programme”, Cambridge Architectural Resarch Limited.

[7] Calvi, G.M., Pinho, R., Magenes, G., Bommer, J.J., Crowley, H. (2006). “Development of Sesimic Vulnerability Assessment Methodologies Overthe Past 30 Years”, 43(472), 75-104.

[8] Rossetto, T., Elnashai, A. (2003). “Derivation of vulnerability functions for European-type RC structures based on observational data”, Eng. Struct. 2003, 25, 1241–1263. [Google Scholar] [CrossRef].

[9] Maniyar, M. M., Khare, R., Dhakal, R. P. (2009). “Probabilistic seismic performance evaluation of non-seismic RC frame buildings”, Struct. Eng. Mech. 2009, 33, 725–745.

[10] Ioannou, I., Douglas, J., Rossetto, T. (2015). “Assessing the impact of ground-motion variability and uncertainty on empirical fragility curves”, Soil Dyn. Earthq. Eng. 2015, 69, 83–92.

[11] Benedetti, D., Petrini, V. (1984).“On seismic vulnerability of masonry buildings: proposal of an evaluation procedure”, L’Industria delleCostruzioni 18:66-74.

[12] GNDT. (1993). “Seismic risk of public buildings”, Vol.1, Methodological aspects Research Report. Rome: GNDT.

[13] Ferreira, T. M., Maio, R., Vicente. R. (2017). “Vulnerability Assessment of the Old City Centre of Horta Portugal: Calibration and Application of a Scoring Method”16th World Conference on Earthquake Engineering, 16WCEE 2017, Santiago, Chile.

[14] GNDT. (1994). “Scheda di esposizione e vulnerabilità e di rilevamento danni di primo livello e secondo livello (muratura e cemento armato”, Gruppo Nazionale per la Difesa dai Terremoti: Roma, Italy.

[15] Giovinazzi, S., Lagomarsino S. (2004). “A Macroseismic Model for the vulnerability assessment of buildings”, 13th World Conference on Earthquake Engineering. Vancouver, Canada.

[16] Grünthal, G. (1998). “European Macroseismic Scale 1998”, In European Center of Geodynamics and Seismology.

[17] Giovinazzi, S. (2005). “The Vulnerability Assesment and the Damage Scenario in Seisimic Risk analysis”. PhD Thesis, Technicla University Casolo- Wilhelmina at Braunschweig, Braunschweig, Germany and University of Florencem Florence, Italy.

[18] Ferreira, T., Vicente, R., Varum, H. (2014). “ Seismic Vulnerability Assessment of Masonry Façade Walls: Development, Application and Validation of a New Scoring Method”. Structural Engineering & Mechanics, Vol.50, No: 4, DOI: http: //dx.doi.org/10.12989/sem.2014.50.4.541

[19] Vicente, R., Parodi, S., Lagomarsino, S., Varum, H. (2008). “Seismic Vulnerability Assessment, Damage Scenarios and Loss Estimation, Case Study of the old city centre of Coimbra, Portugal”, the 14 th World Conference on Earthquake Engineering, October 12-17, Beijing, China.